

**An Exploratory Study into Iron/Chromium Redox Flow Batteries and Kinetic
Method Development for Materials Discovery**

by

Zachary Parr

B.A. Chemistry, Washington & Jefferson College, 2020

Submitted to the Graduate Faculty of
the Swanson School of Engineering in partial fulfillment
of the requirements for the degree of
Master of Science

University of Pittsburgh

2022

UNIVERSITY OF PITTSBURGH
SWANSON SCHOOL OF ENGINEERING

This thesis was presented

by

Zachary Parr

It was defended on

May 27, 2022

and approved by

Dr. Susan Fullerton, Ph.D., Associate Professor, Department of Chemical and Petroleum
Engineering, Department of Electrical and Computer Engineering

Dr. Tagbo Niepa, Ph.D., Assistant Professor, Department of Chemical and Petroleum
Engineering, Department of Bioengineering

Thesis Advisor: Dr. James McKone, Ph.D., Assistant Professor, Department of Chemical
and Petroleum Engineering, Department of Chemistry

Copyright © by Zachary Parr
2022

An Exploratory Study into Iron/Chromium Redox Flow Batteries and Kinetic Method Development for Materials Discovery

Zachary Parr, M.S.

University of Pittsburgh, 2022

The world will face an important challenge over the next 30 years switching from the reliance of fossil fuels to renewable energy sources. Wind and solar are the most likely energy source for this transition, but their availability is not consistent enough to meet the world's energy demand. Thus, an important part of overcoming our reliance on fossil fuels will be to store renewable energy sources when they are abundantly available to be used during periods when their availability is less than the demand.

This thesis describes my efforts and contributions toward this challenge through research done on redox flow batteries over the past 2 years. Our team was able to address a key problem found through literature in this field that highlighted discrepancies for kinetic rate constant values extracted through various methods for viable flow battery electrolyte redox reactions. We developed a universal method to analyze flow battery electrolyte kinetics in an in-situ environment that yielded k_{eff}^0 results within an order of magnitude difference of simulated data. By standardizing kinetic extraction methods for different flow battery electrolytes, we hope to advance materials discovery for flow batteries and move towards a cost competitive alternative for grid scale energy storage.

Additionally, we studied the $\text{Cr}^{3+/2+}$ redox reaction in detail for its application in an Fe/Cr redox flow battery. The reversibility of the $\text{Cr}^{3+/2+}$ redox reaction has been problematic in advancing Fe/Cr redox flow batteries in the past. However, by using saturated salt solutions, we found we could enhance the $\text{Cr}^{3+/2+}$ redox kinetics across various electrodes. We hypothesize that a local pH affect near the electrode surface is allowing for redox chemistry to occur. We hope that by continuing this study, the use of saturated salt solutions can be implemented to optimize $\text{Cr}^{3+/2+}$ redox chemistry in Fe/Cr RFBs.

Table of Contents

Preface	x
1.0 Introduction	1
1.1 Purpose	1
1.2 Background on the Importance of Energy Storage	2
2.0 Flow battery Electroanalysis 3: Online Kinetic Measurements Using Ultramicroelectrodes in Channel Flow	7
2.1 Introduction	7
2.1.1 Why RFBs?	7
2.1.2 The Need for RFB Materials Discovery	8
2.2 Experimental Methods	13
2.3 Results and Discussion	14
2.3.1 Battery Behavior	14
2.3.2 Data from the Analytical Cell	18
2.3.3 Quantifying Electron Transfer Rates	21
2.3.4 Experimental Kinetics Characterization	23
2.4 Conclusions	26
3.0 Enhancement of the $\text{Cr}^{3+/2+}$ Redox Reaction in Saturated Salt Solutions	28
3.1 Introduction	28
3.2 Preliminary Work: Unsuccessful Attempts to Replicate Key Results from NASA	30
3.2.1 Reproducing $\text{Cr}^{3+/2+}$ Redox Chemistry on Carbon Felt	33
3.3 Experimental Methods	35
3.4 Results and Discussion	39
3.4.1 Stability Window Expansion	39
3.4.2 Enhancement of $\text{Cr}^{3+/2+}$ Redox Chemistry	45
3.4.3 Cr^{3+} Speciation in Different Environments	50

3.4.4 Nicholson Fittings for k_o Values	51
3.5 Conclusions	53
4.0 Additive Manufacturing	56
4.1 Introduction	56
4.2 Results and Discussion	58
4.3 Conclusion and Future Work	61
5.0 Conclusion and Closing Remarks	63
Appendix A. A. Detailed Experimental Procedure from Chapter 2	64
Appendix B. B. Tabulated Literature Values displayed in Figure 3	70
Bibliography	72

List of Tables

1	Variation of Peak Potential Separations with Kinetic Parameters for Cyclic Voltammetry	38
2	Compiled kinetics data for aqueous RFB redox couples at various types of carbon electrodes	71

List of Figures

1	Adapted from EIA the impact and future expectations for renewable energy as a replacement for coal and natural gas	3
2	From US EIA a look at the energy demand	5
3	Compiled rate constant for carbon electrodes	10
4	Apparatus Schematic	12
5	Figures of merit for the symmetric RFB cell containing $\text{Fe}^{3+/2+}$ electrolyte . . .	15
6	Data from continuous voltammetric cycling of UMEs in the analytical cell . . .	17
7	Empirical workflow for the shrinking overpotential method	20
8	Empirical kinetics data for three types of UME electrode in $\text{Fe}^{3+/2+}$ RFB electrolyte	24
9	From NASA Redox Storage System Development Project - Final Report. Fe/Cr redox flow battery schematic.	31
10	Preliminary experiments in attempts to suppress HER	34
11	Glassy carbon electrode potential range expansion	40
12	Gold electrode potential range expansion	41
13	Platinum electrode potential range expansion	42
14	Glassy carbon electrode potential range expansion	43
15	The cyclic voltammograms for .1M Cr^{3+} in saturated salt solution on glassy carbon, gold, and platinum electrodes	46
16	The cyclic voltammograms for the $\text{Cr}^{3+/2+}$ and $\text{Fe}^{3+/2+}$ redox reactions using .1M Cr^{3+} and .1M Fe^{2+} in saturated LiCl solutions	48
17	Shows the speciation of Cr^{3+} in different environments	49
18	The iR compensated cyclic voltammograms for different concentrations of LiCl at different scan rates	52
19	The Ψ vs inverse square root of the scan rates for different saturations of LiCl .	54
20	Manufacturing life cycle	57
21	Additive manufacturing results	59

22	3D print future work	62
23	Photo of apparatus used in Chapter 2	66

Preface

I owe special thanks to a plethora of people for helping me get to the point I am currently at as a chemical engineer. I will start by thanking my advisor Dr. James McKone for his helpful insight and words of encouragement throughout my time at Pitt . Your expertise and enthusiasm in electrochemistry have driven me to complete my Master's degree and I will always keep electrification of the chemical industry in mind as I pursue a career in the field. You have helped me grow as a researcher, an engineer, a chemist, a writer, and most importantly, as a person. For that, I am forever grateful.

Next, I would like to acknowledge the members on my thesis committee. Dr. Fullerton, I am grateful for you teaching me and supporting me during the trials and tribulations I experienced learning chemical transport phenomena. Your stories and encouragement pushed me to be a better student and engineer. I am thankful to have had such a wonderful professor. Dr Niepa, your mentorship to me through the GEES program served as a great reminder to me to acknowledge how far I had come as a researcher. Our monthly meetings helped keep me on track to achieve the goals I had set for myself at the very beginning of the program. Your advice and shared experiences were integral to my success.

Finally, I want to give a special thanks to all McKone lab members who I had the pleasure to work with over the past few years. Becca, thanks for being the other half of our graduate RFB team and giving me expert insight on all the MARVEL movies and TV shows. Evan, thank you for always having an open door for ChE613 questions, electrochemical insight, and golf talk. I hope we have not played the last of our rounds together. Todd and Jared thank you for being patient and learning the difficulties of 3D printing along side me. To all others, Sammie, Jeff, Carissa, Thomas, Rituja, Tejal, Manjodh, and Audrey, our conversations and your encouragement to me should not go unmentioned. Thank you all for all that you have contributed to me. My future successes are made possible through my interactions with each of you.

1.0 Introduction

1.1 Purpose

This thesis describes the studies I have completed over the course of the last 2 years (2020-2022). It is written to satisfy the requirements of a Master's degree in Chemical Engineering from the University of Pittsburgh. It also contains all necessary components of the work I have completed, such that students or researchers interested in the progression of Redox Flow Batteries (RFB) as a viable form of energy storage or any student who completes the future work associated with my studies can use it as reference.

The contents are divided into 5 chapters. The remainder of this chapter will serve as an overview of the dissertation itself, an introduction to the field of energy storage, and some of the preliminary experiments I performed that laid the foundation for the work I completed in Chapter 3. Chapters 2-4 summarize the bulk of the work I have completed in my time at Pitt, covering experimental details and results. Chapter 2, specifically, contains the full text of a manuscript currently under review in the *Journal of Materials Chemistry A* entitled "Flow Battery Electroanalysis 3: Online Kinetics Measurements Using Ultramicroelectrodes in Channel Flow." Chapter 3 summarizes my work using concentrated LiCl (aq) solutions to enhance the kinetics of the $\text{Cr}^{3+/2+}$ redox couple. Chapter 4 covers work I completed to jump-start the process of generating electrochemical cell prototypes using additive manufacturing. Note that Chapter 4 was written in a conversational style because it is mainly intended to be informative and entertaining to others who wish to use additive manufacturing in the McKone Lab in the future. Chapter 5 offers a final summary and recommendations for future students following up my work along with broader comments about my experience in the McKone Lab at Pitt.

In addition to the contents of my thesis discussed above, Appendix A includes a procedure for how to construct the apparatus and capture the kinetics measurements reported in Chapter 2.

It was designed as a detailed tutorial that can be treated as an instruction manual for future work. Videos of me constructing the apparatus can also be found on the McKone Lab Youtube channel.

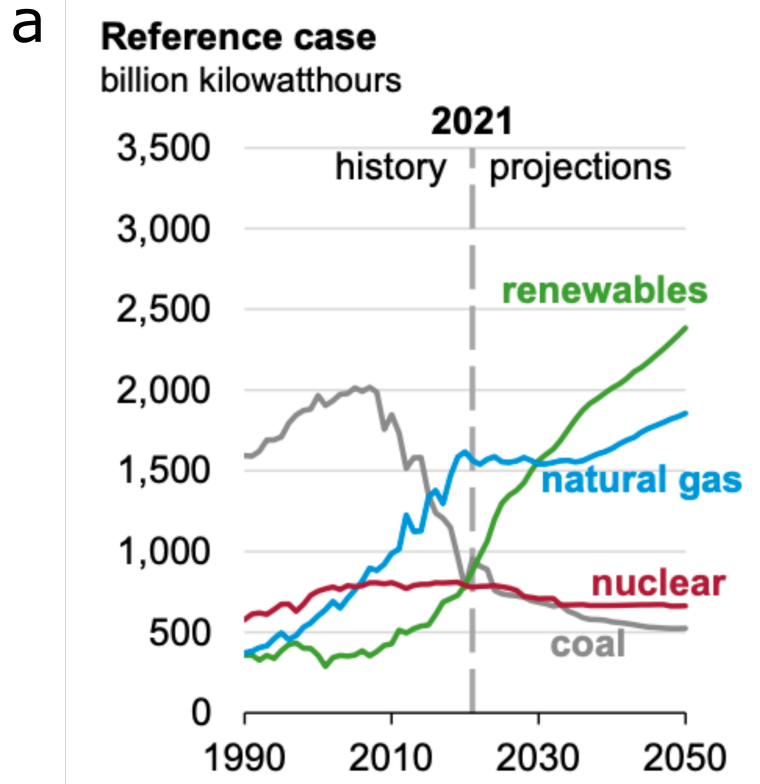
I hope this thesis will not only satisfy the requirements for a Master's degree, but also help the students that follow up my work in making the use of RFBs more practical, even more specifically, for the talented researchers who will join the McKone Lab in the future.

1.2 Background on the Importance of Energy Storage

When I wrote this dissertation in the Spring of 2022, the world had begun a transition to greener forms of energy and had made a deep commitment to decreasing carbon emissions. Largely contributing to carbon emissions are the main sources of energy we currently use which include coal, petroleum, and natural gas. However, the transition away these forms of energy can not happen overnight because currently, they account for 79% of the total energy supply[1].

Additionally, in March 2022, the world's largest exporter of oil, Russia, invaded Ukraine. As countries continue to sanction Russia and the price of oil continues to climb, in my eyes, there is no better opportunity to look for a new way to meet the world's energy demand. As we transition into new eras of clean energy output, finding new methods to store that energy is equally as important.

Alternative forms of energy include renewable sources easily accessible to us like wind and solar energy, or energies that give off net-zero carbon emissions like nuclear energy. Nuclear energy is viewed as a viable alternative because of its net zero carbon emissions. However, the uranium mining that is required to power nuclear energy is an indirect CO₂ intensive process[2, 3, 4]. Wind energy is a readily available and renewable form of energy that converts to electrical energy by turning the blades of a wind turbine[5, 6]. Similarly, solar energy is an abundant form of renewable energy which uses light from the sun that converts to electrical energy through solar panels[7, 8].



b

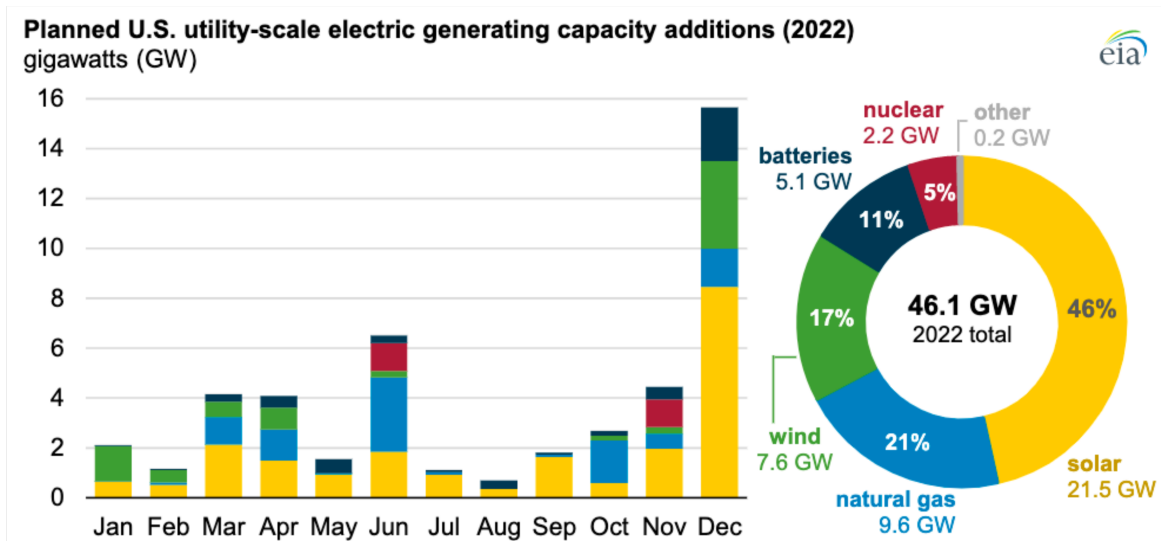


Figure 1: (a) Adapted from EIA the impact and future expectations for renewable energy[9].
(b) Adapted from the EIA shows the capacity addition in GW for investments in renewable energy infrastructure in the US[9].

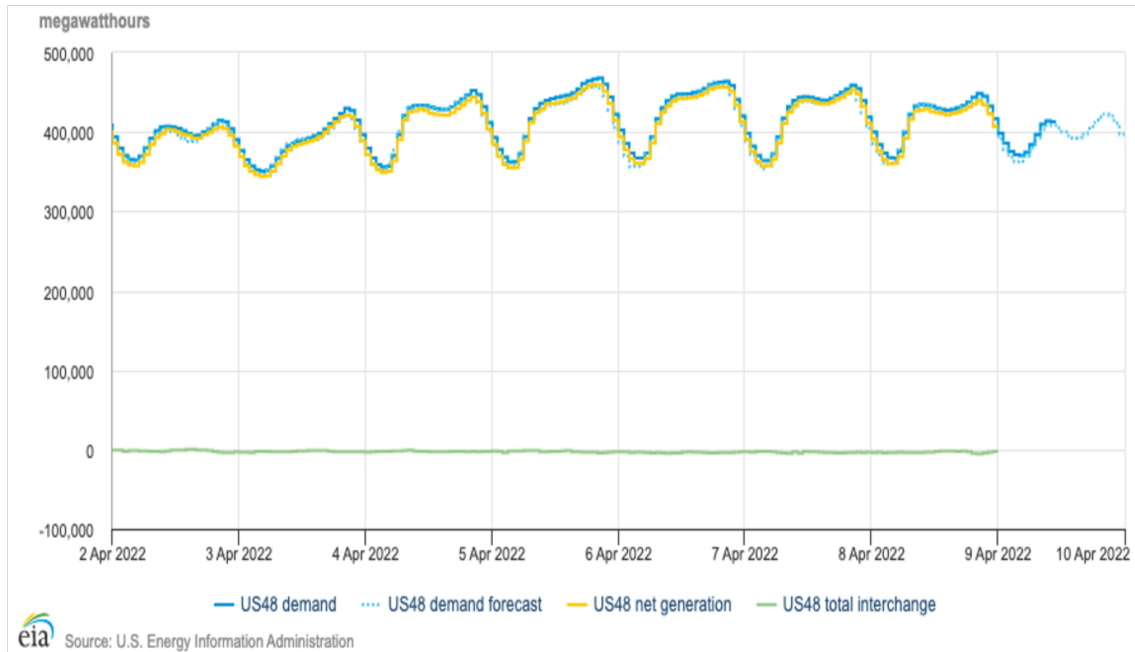
In Figure 1 (a), we can see the impact renewable energy has had on US electricity generation for the past 3 decades and the outlook for the future. The EIA predicts that renewable energy generation will be the main source of electricity in the US before 2050[9]. Figure 1 (b) further supports this narrative. Looking at the expected additions for renewable energy in the US for 2022, we observe that over 50% of the energy will come from wind and solar [9].

While this transition is integral for our planet, we must be realistic about alternative forms of energy. Taking a look at Figure 2 (a), we can see a general trend in the energy demand in the United States over a short period of time. There are slight fluctuations in this trend during the night hours, but for the most part the energy demand remains relatively constant[10]. Looking at Figure 2 (b), the power output from a solar and wind company in Spain was collected over time. For wind power, the trend is relatively random as the time when the wind blows cannot be controlled[11]. Similarly, a span a cloudy days can hinder the availability of sunlight to be used as solar energy[11]. As most of the renewable energy sources are made up of wind and solar energy, to meet the energy demand of the world we must have the ability to store these forms of energy when they are abundantly available for periods in time where they are not[12, 8, 13].

There are a variety of energy storage systems that are available today, including pumped-storage hydroelectricity, capacitors, compressed air energy storage, flywheels, and batteries. Of these energy storage systems, batteries have emerged as a front runner because of characteristics related to the current needs of the energy grid[12, 8, 14]. These characteristics include rapid response time, flexible installation, and short construction cycles. Flexible installation and short construction cycles allow for easy expansion of the energy grid, while, rapid response times allow for batteries to immediately meet the need for energy [15, 14, 8].

More specifically, Li-ion batteries are currently used for 77% of the current grid scale energy storage in the US[14, 15]. Li-ion batteries have become popular because of high energy densities, high energy efficiency, and long life cycles. Even though Li-ion batteries have been accepted as the main form of grid scale energy storage, there exist safety and environmental downsides[14, 15]. Li-ion batteries used for grid scale energy storage are currently made of non-aqueous materials that are often toxic and flammable. Li-ion batteries are also capable

a



b

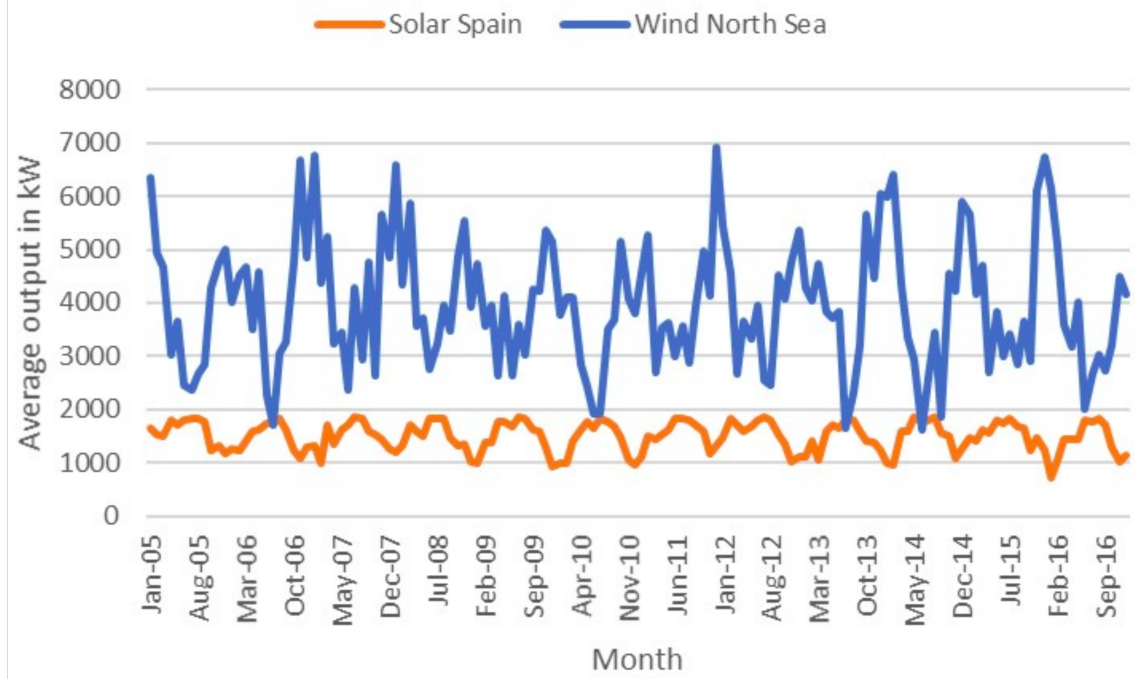


Figure 2: (a) from US EIA a look at the total energy demand in the US over 9 days[10]. (b) average energy output of wind and solar panels adapted from an energy company (KYOS) in Spain [11].

of spontaneous ignition and subsequent explosion when overheated[16, 17, 18]. Additionally, when exposed to low temperatures during charging, anodic buildup of Li metal can lead to increased risk of failure[16, 18]. This is not convenient for storing renewable forms of energy like solar and wind as they are still abundantly available under colder conditions. Further, the organic materials used as electrolytes in Li-ion batteries also pose toxicity risk[17, 18]. A study simulating the toxicity risks of overheated Li-ion batteries showed depending on battery electrolyte choice, Li-ion batteries can give off carbon monoxide, hydrofluoric acid gas, and sulfur dioxide all which are harmful to humans [18]. Further, if these storage devices get damaged by natural disaster or an accidental event, they can cause a great deal of environmental damage.

To avoid the hazards associated with the current non-aqueous Li-ion batteries, a shift toward aqueous batteries has recently emerged. These include aqueous Li-ion batteries and aqueous redox flow batteries (RFBs)[19, 20, 14, 15]. A good battery should have a large stability window in order to maximize the amount of potential energy stored per Coulomb of charge[21]. Aqueous batteries are hindered in this regard, as the voltage difference between water splitting reactions, the hydrogen evolution reaction (HER) and the oxygen evolution reaction (OER), is only 1.23V [22, 23, 24, 21]. Expanding this stability window is an important research topic in advancing safer forms of alternative energy storage. My efforts to contribute to this field will be highlighted in chapter 3.

Further, RFBs are currently being researched as cost competitive alternatives to Li-ion batteries because of their characteristically high charge per unit area[25]. But as I will discuss further in this dissertation, RFBs are currently hindered by their material cost. For RFBs to become cost competitive with Li-ion batteries, they will need to reduce their materials cost by a factor of 2-3 [26, 25, 27]. Currently, the state of the art in RFBs involves a non-abundant metal, vanadium, which contributes to the bulk of RFB materials cost[28, 29, 30, 31, 32]. Because vanadium is not abundant on Earth, there is a need for further materials discovery of RFB electrolytes that allow for a cheaper alternative[26, 25, 27]. My contributions to standardizing kinetics measurements for flow battery materials discovery will be highlighted in Chapter 2.

2.0 Flow battery Electroanalysis 3: Online Kinetic Measurements Using Ultramicroelectrodes in Channel Flow

This chapter reproduces a pre-print version of our manuscript with the same title, submitted in the Spring of 2022 to the *Journal of Materials Chemistry A*. My specific involvement in the development of this manuscript was to carry out the experiments, help analyze the data from those experiments, and contribute to the written portion of the manuscript. Other contributors to this research effort include Becca Segel, Tejal Sawant, Dean Miller, Thomas Henry, Carissa Yim, and James McKone. On a broader scale, this chapter of my thesis will highlight a standardized method that allows for consistent kinetics measurements for redox flow battery materials discovery. We hope that by contributing to the efficiency in flow battery electrolyte testing, we can more rapidly approach a sustainable source of alternative energy storage.

2.1 Introduction

2.1.1 Why RFBs?

Stationary batteries are valuable for increasing the efficiency and flexibility of the electric grid by storing excess power during periods of low demand and delivering power when the demand is high[33, 34, 35]. This type of load leveling will become increasingly important as the proportion of power provided from intermittent renewables continues to grow [36, 37]. As previously stated, due in large part to recent advances in the manufacturing of Li-ion batteries for transportation applications, Li-ion technologies are also the primary focus in the growing market for grid-scale energy storage[38, 39]. However, the redox flow battery (RFB) presents an attractive alternative to Li-ion and related battery technologies because the cost per unit of stored energy decreases dramatically as the size of the battery increases[26, 40, 41].

This is a direct consequence of the characteristic decoupling in RFBs between the design of redox-active liquid or semisolid electrolytes (and their storage containers) and the charge-discharge stack.

Flow batteries have been under active development for half a century. Early work by NASA in the 1970s focused on transition metal complexes in water, culminating in the development of an iron-chromium RFB [42, 27]. The all-vanadium RFB (VRFB) was demonstrated thereafter by Skyllas-Kazacos in 1985, and this remains the most technologically mature RFB chemistry [28, 29, 30, 31, 32]. Key advantages for VRFBs include a cell voltage that closely matches the thermodynamic stability window of water and near-complete immunity to permanent capacity fade since the vanadium-based positive and negative redox couples are interconvertible and easy to regenerate. However, vanadium ore is costly to recover and process, which limits the ability of VRFBs to meet the anticipated global demand for grid storage[38, 43]. Specifically, several techno-economic studies have concluded that redox couples for aqueous RFBs should be at least 2-3 times less costly than vanadium, whereas higher costs are tractable for nonaqueous chemistries with larger cell voltages [26, 25, 27].

2.1.2 The Need for RFB Materials Discovery

The need for new RFB chemistries that outperform the incumbent VRFB technology has motivated a surge of research on materials discovery over the past several years. Significant advances from the last decade include aqueous organic redox couples that are stable when cycled in water,[44, 45, 46, 47], high voltage nonaqueous electrolytes,[48, 49, 50, 51, 52, 40, 53], molecules exhibiting multi-electron transfer reactions,[54, 55, 56, 57, 58, 59], and unconventional electrolytes based on deep eutectic solvents[60, 61, 62]. We encourage readers to consult the available review literature for more extensive and comprehensive summaries of ongoing work [63, 64, 65].

A key advantage for redox flow batteries is their ability to operate at high areal current densities [25]. Accordingly, efficient operation requires fast electron-transfer kinetics, and the effective interfacial electron transfer rate constant (k_{eff}^0) is a key figure of merit. Note that we

use “effective” here to denote empirically derived rate constants based on superficial electrode areas, which do not consider the areal density and heterogeneity of sites at which electron-transfer occurs. Thus, k_{eff}^0 is closely related to the superficial exchange current density J_0 except that it is directly comparable across electrolytes at different concentrations[66].

Numerous analytical methods have been used to study the electron-transfer kinetics on RFB electrodes and electrolytes[67, 68, 69, 70]. The most prevalent approaches include stationary and rotating disk electrode voltammetry,[71, 72, 73, 74, 75], electrochemical impedance spectroscopy,[76, 77, 78, 79, 80] micropolarization, [81, 82, 83, 84, 85], and microelectrode voltammetry[86, 87, 88]. Although each of these approaches is based on a firm foundation in analytical electrochemistry,[89] there exists major discrepancies in the reported values of electron transfer rate constants even for the most heavily studied RFB electrodes and redox couples (Figure 3)[90, 91, 92, 93, 94, 95, 96, 97, 98, 99, 100, 101, 102, 103, 104]. This high level of variability frames an important scientific question: is it possible to accurately measure k_{eff}^0 for RFB active materials?

For the past several years, a major research focus of our lab has been addressing the question above by developing straightforward, replicable methods for measuring electron transfer kinetics in RFBs. Using aqueous $\text{Fe}^{3+/2+}$ redox couples as model RFB electrolytes, we first showed that it is possible to obtain reproducible kinetics measurements on noble metals using stationary and rotating disk electrode (RDE) voltammetry, but only if the electrode surfaces are kept scrupulously clean[105]. We also studied $\text{Fe}^{3+/2+}$ kinetics at glassy carbon electrodes and found that these are less sensitive to fouling but highly sensitive to electrode pre-treatment conditions[106]. Specifically, we found that oxidative pretreatments markedly improve electron-transfer kinetics for Fe-based RFB electrolytes, but only if they increase the fraction of carbonyl functionalities (as opposed to alcohol or ether functionalities) on the electrode surface.

In the course of our prior studies of RFB kinetics, we also encountered several practical drawbacks for the use of stationary and hydrodynamic voltammetry at macroelectrodes. For example, the relatively large currents (10 mA or more at mm-scale electrodes) that are generated in concentrated (1 M or greater) electrolytes makes it difficult to fully correct for voltage errors due to series resistance, because errors of only a few percent in the measured

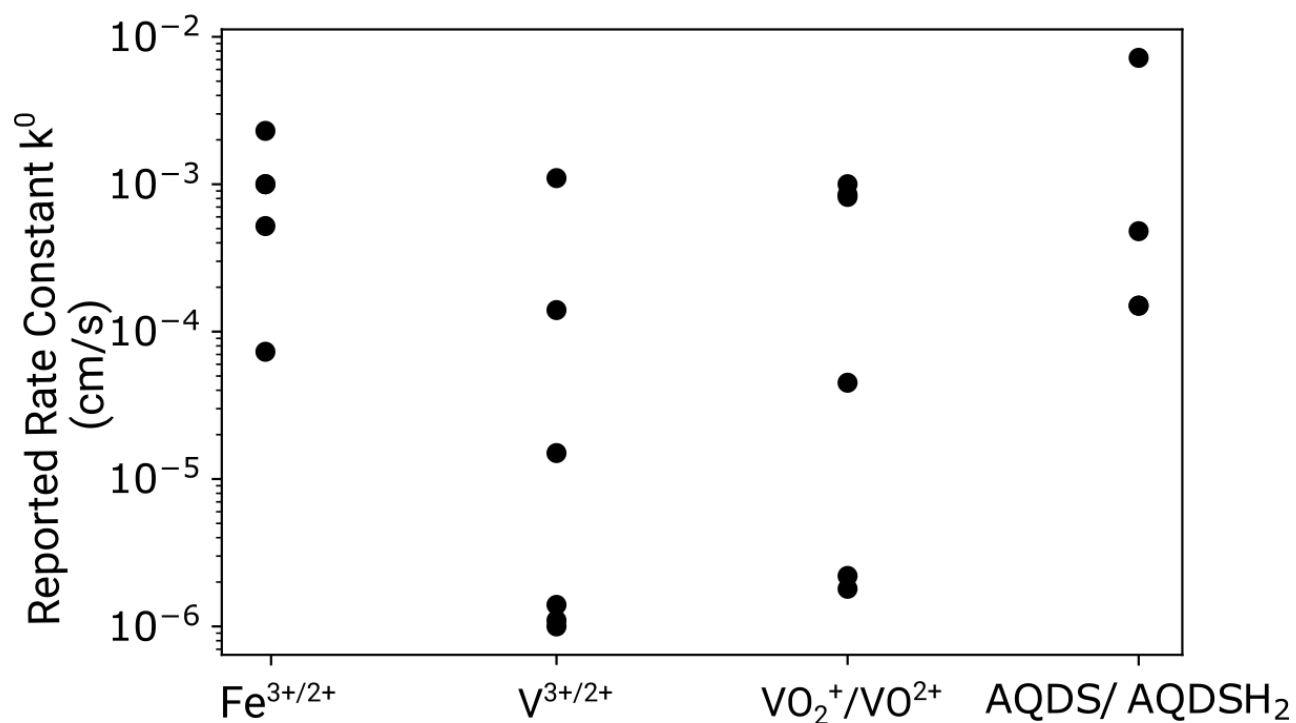


Figure 3: Compiled literature rate constant values reported previously for carbon electrodes and several widely studied RFB redox couples. Note that AQDS/AQDSH₂ refers to the oxidized and reduced forms of anthraquinone disulfonic acid. Tabulated values and references are compiled in Appendix B.

resistance can have a large impact on the final results. These analytical techniques are also tedious because they require the completion of multiple experiments to extract a single rate constant. This in turn makes it difficult to collect replicate measurements or extend kinetic analysis to multiple states of charge, particularly when electron-transfer rates are sensitive to the history of the electrode surface. Finally, most voltammetric techniques require explicit measurements of transport-limited current densities so that transport contributions can be eliminated mathematically from the kinetic analysis. This is a particular problem for RFB studies because the best RFB electrolytes feature redox couples whose reduction potentials are very near the stability limits of the solvent, supporting electrolyte, or electrode. Thus, applying overpotentials that are extreme enough to achieve a transport limit risks irreversible damage to these key battery components. Indeed, practical battery operation usually entails the use of voltage cutoff limits specifically to avoid extended operation under transport-limited conditions.

In this chapter, we describe an approach for kinetics measurements that overcomes several of the aforementioned challenges when used with flow battery active materials. We constructed a 3-electrode cell, featuring an ultramicroelectrode (UME) in a channel-flow configuration, and inserted it into the flow loop of a fully functional RFB, then used the 3-electrode cell to execute voltammetry measurements as the battery underwent charge and discharge. We further developed an empirical approach that we call the *shrinking overpotential method* to extract an estimate of k_{eff}^0 from each voltammogram. Benchmarking our method using simulated voltammetric data showed that accurate measurements can be made over the full range of state of charge (SOC) values that are relevant for RFB operation and for k_{eff}^0 values ranging over several orders of magnitude. We then implemented these tools to measure k_{eff}^0 for the $\text{Fe}^{3+/2+}$ redox couple at Pt and carbon fiber UMEs. The results broadly agree with prior findings that reaction rates vary in the order Pt > electrochemically oxidized C > pristine C[106, 92, 94]. Our data also suggest that Pt electrodes are activated by cycling in Fe RFB electrolyte over at least several hours, whereas pristine and oxidized C fiber electrodes remain quite stable on the same timescale.

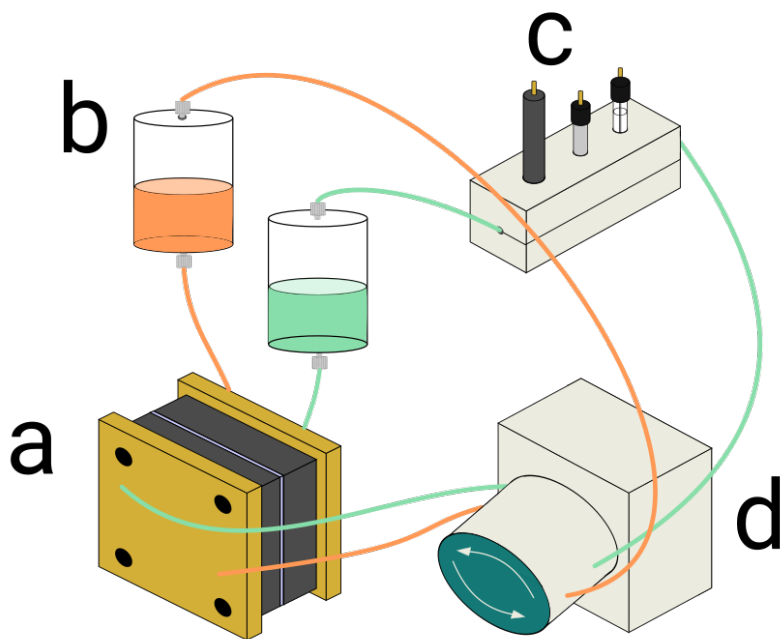


Figure 4: Schematic representation of the experimental apparatus: (a) flow battery charge–discharge cell, which allows for the charge and discharge of the $\text{Fe}^{3+/2+}$ electrolyte; (b) electrolyte storage reservoirs, which are gas tight and also function as pulsation dampeners; (c) analytical half cell containing an ultramicroelectrode working electrode, a graphite rod counter electrode, and an Ag/AgCl reference electrode; (d) peristaltic pump that drives fluid flow through the path defined by the tubing demarcated in orange and teal in a counter-clockwise fashion.

2.2 Experimental Methods

Figure 4 schematizes the apparatus that was used to execute experimental measurements, comprising continuous ultramicroelectrode (UME) voltammetry at platinum and carbon fiber UMEs while cycling an $\text{Fe}^{3+/2+}(\text{aq})$ electrolyte through various states of charge in a coupled RFB. Appendix A includes a detailed discussion of experimental methods, and an abbreviated summary is as follows.

The flow battery itself comprised a 10 cm² commercial flow battery stack with two 5 mL reservoirs and a peristaltic pump. The electrodes in the stack were carbon felt and the membrane was Nafion. It was assembled in an unbalanced, compositionally symmetric cell configuration, as described in detail by Aziz et al [107]. The capacity limiting side of the battery was charged with 3.5 ± 0.5 mL of 1M FeCl_2 in 2 M $\text{HCl}(\text{aq})$ for kinetics measurements. The non-capacity limiting side was charged with 12.5 mL of an electrolyte containing 0.5 M each of FeCl_2 and FeCl_3 in 2 M $\text{HCl}(\text{aq})$. The battery was cycled continuously at ± 20 mA/cm² (based on the superficial area of the battery electrodes) over a cell potential of ± 0.6 V. This corresponds to a C-rate of $\sim 2.1\text{C}$ based on the theoretical capacity of the capacity limiting side of the battery.

A second, home-built electrochemical cell, hereafter referred to as the analytical cell, was placed in fluidic series between the capacity-limiting battery reservoir and the peristaltic pump. It contained a 1 x 1 x 35 mm flow channel with threaded holes oriented perpendicular to the flow direction into which commercial working, counter, and reference electrodes were inserted. The working electrodes were either platinum or carbon fiber UMEs; the reference electrode was Ag/AgCl ; and the counter was a graphite rod. The working electrodes were prepared by abrasive polishing and additional pre-treatment steps as described previously by Sawant et al [106].

Cyclic voltammetry measurements were collected continuously by cycling the potential between 0.1 and 0.9 V vs. Ag/AgCl at a scan rate of 20 mV/s.

A single experimental run involved 5 charge–discharge cycles in the RFB and continuous voltammetric cycling as described above. Note that we define the “charging” direction of the battery to be oxidation of the capacity limiting FeCl_2 electrolyte, consistent with the use

of $\text{Fe}^{3+/2+}$ as the positive redox couple in an Fe/Cr RFB. A set of 15 runs were completed in total—5 replicates each of 3 different UME working electrodes. We also completed one longer set of continuous cycling measurements to confirm the general performance and operational stability of the RFB; note that 4.5 mL of capacity limiting electrolyte was used in this case.

We extracted performance metrics—including full cell voltage as well as capacity and coulombic efficiency of the capacity limiting side—from the RFB cycling data. We also extracted SOC and k_{eff}^0 from cyclic voltammetry data, as described in the corresponding sections below. Error bounds are reported as 95 % confidence intervals unless otherwise noted.

2.3 Results and Discussion

2.3.1 Battery Behavior

Figure 5 depicts representative charge–discharge data for the RFB cell. Panel 5a shows cell voltage vs. time for one experimental run comprising 5 charge–discharge cycles at 20 mA/cm². These data are nearly symmetric about 0 V, which is consistent with cell configuration where the composition of the capacity limiting electrolyte varies from predominantly Fe^{3+} to predominantly Fe^{2+} while the non-capacity limiting side remains very near to equimolar $\text{Fe}^{3+/2+}$ throughout the experiment. Panel 5a also depicts the average cell potential during the charge and discharge cycles, which were .20V and -0.16V, respectively. These values enable a rough estimate of the average overpotentials as ≤ 100 mV each at the anode and cathode, which are reasonable when considering the superficial current density was modest and the carbon cloth electrodes (which were not subjected to any treatment to improve their catalytic properties) have large electroactive surface areas. We observed distinct “breaking in” behavior in 6 out of 15 RFB charge–discharge experiments, where stable potential vs. time behavior was only achieved after one or several cycles. We attribute this mainly to the time required for the electrolyte to fully wet the electrodes.

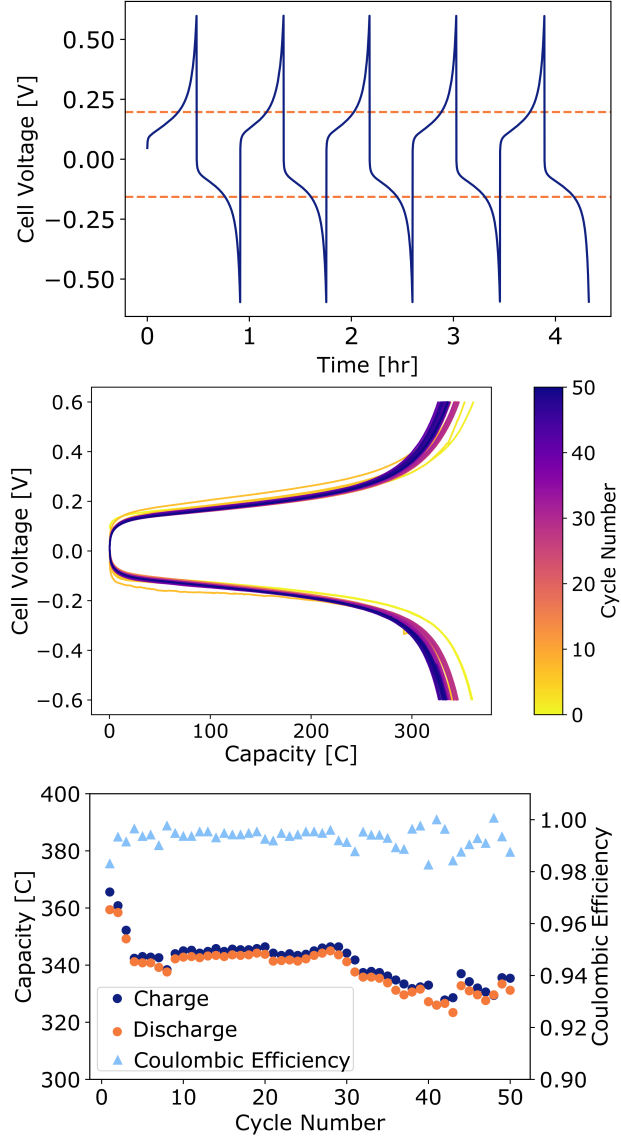


Figure 5: Compiled figures of merit for the symmetric RFB cell containing $\text{Fe}^{3+/2+}$ electrolyte in an unbalanced, compositionally symmetric configuration: (a) cell voltage vs. time during a 5-cycle charge-discharge experiment at $\pm 20 \text{ mA/cm}^2$; (b) cell voltage vs. capacity data compiled over a longer 50-cycle charge-discharge experiment; (c) capacity and coulombic efficiency versus cycle number for the same 50-cycle experiment shown in (b).

Figure 5b and 5c compile capacity and coulombic efficiency data during 50 cycles of extended charge–discharge. The average capacity during charge was 341 ± 2 C and the average capacity during discharge was $339 \text{ C} \pm 2 \text{ C}$. This is $\sim 80\%$ of the theoretical capacity, 434 C, based on the concentration and volume of the capacity-limiting electrolyte, which further implies that the capacity-limiting side cycled between 10 and 90 % state of charge. The temporal evolution of battery capacity included an initial settling period during which capacity decreased by 20 C over the first 4 cycles. This was followed by approximately 25 very stable cycles with coulombic efficiencies exceeding 99 %. Cycles 30–50 were somewhat more erratic in capacity and coulombic efficiency; we speculate that the main reason for this behavior was the tendency for small droplets of electrolyte to become entrained on the sidewalls of the reservoirs, as was noted previously by Aziz et al[107].

These data broadly indicate that the RFB cell stably cycles Fe-based RFB electrolytes over technologically relevant states of charge for at least several hours. This was true even while executing analytical measurements at a second cell in the electrolyte flow loop. The use of UMEs in the analytical cell is advantageous because the very small associated current flow minimally perturbs the composition of the electrolyte. Note, however, that this system also benefits from the commercial availability and chemical stability of FeCl_2 and FeCl_3 , which allowed us to create electrolytes of arbitrary initial composition by mixing salts on the benchtop. Adoption of this approach for novel materials or commercially available electrolytes where only one state of charge is available would require an additional pre-electrolysis step to generate a symmetric configuration. This type of processes is well-documented for preparation of positive and negative electrolytes for VRFBs from a single precursor [62, 108, 109]. The $\text{Fe}^{3+/2+}$ redox couple is also only weakly air sensitive, where Fe^{2+} slowly oxidizes in the presence of atmospheric oxygen, which further benefits stable cycling. Similar studies using air sensitive reagents would require additional efforts to exclude atmospheric oxygen.

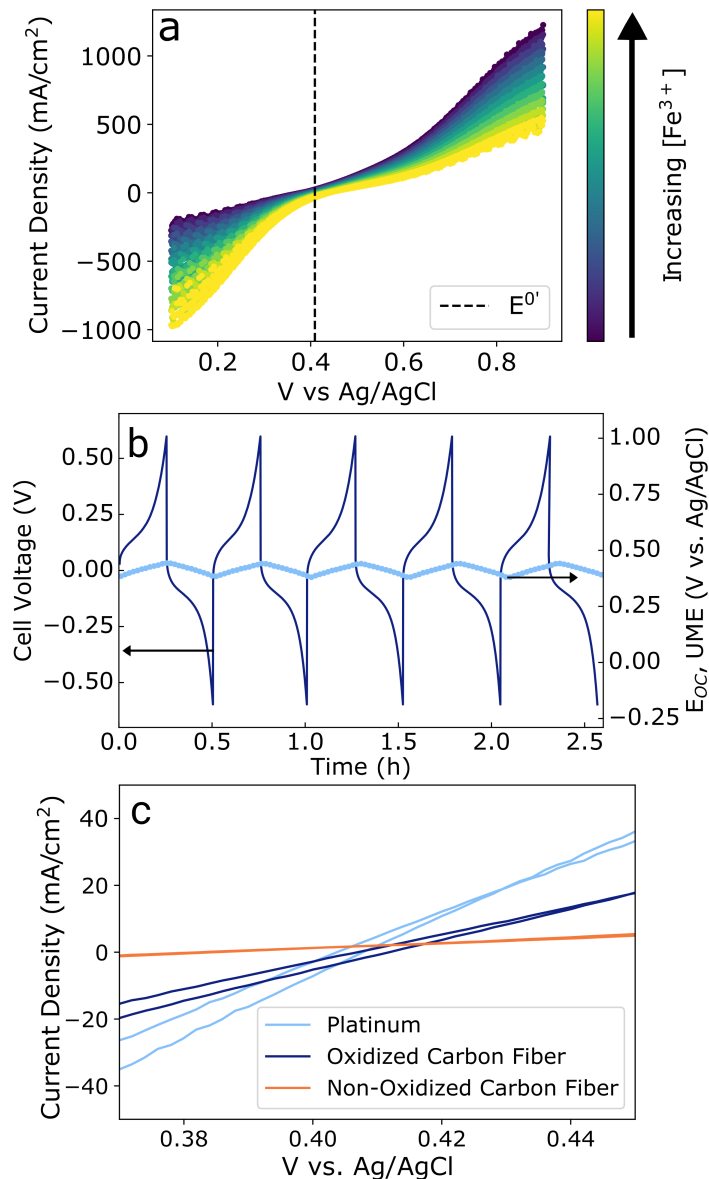


Figure 6: Compiled data from continuous voltammetric cycling of UMEs in the analytical cell: (a) CV data extracted from a time interval from the minimum to the maximum state of charge accessed by the RFB, during which the Fe^{3+} increased continuously; (b) open-circuit potential at the Pt UME (right axis) overlaid against RFB cell voltage (left axis) as a function of time; (c) current density vs. potential data collected at 50 % state of charge for each of the three electrode types used in this study. Note that all carbon fiber electrodes were first treated in isopropanol that had been pre-purified with activated carbon, and oxidized carbon fiber electrodes were further treated by cycling to highly oxidizing potentials in sulfuric acid solution.

2.3.2 Data from the Analytical Cell

Figure 6 collects representative results from UME voltammetry in the analytical cell. The current density vs. potential data in panel 6a were extracted from a Pt UME during continuous cycling over the time interval corresponding to a single charging cycle in the RFB. Hence, the data show clear progression of decreasing anodic current density and increasing cathodic current density as the concentration of Fe^{3+} increases. Notably, the difference between the maximum and minimum current densities (normalized to the superficial area of the UME, $5.9 \times 10^{-7} \text{ cm}^2$) approaches 1.5 A/cm^2 , which attests to the ability of the UME electrode geometry to achieve very high rates of mass transfer, especially with the additional convection afforded by a flowing electrolyte.

We also recorded the temporal progression of the open-circuit potential (E_{oc}) from the UME voltammetry data as the applied potential vs. Ag/AgCl when the current density traversed through 0 mA/cm^2 during each CV sweep. These values are plotted in panel 6b using the righthand y axis alongside cell voltage on the lefthand y axis. These data are directly indicative of the state of charge (SOC) of the capacity limiting electrolyte through the Nernst equation:

$$E_{oc} = E^{0'} - \frac{RT}{nF} \ln \frac{[\text{Fe}^{2+}]}{[\text{Fe}^{3+}]} \quad (2.1)$$

where

$$SOC = \frac{[\text{Fe}^{3+}]}{[\text{Fe}^{3+}] + [\text{Fe}^{2+}]} \quad (2.2)$$

and all other symbols have their regular electrochemical definitions[110]. These data provide similar information to the open-circuit potential excursions used in galvanostatic intermittent titration technique (GITT) measurements,[111, 112] with the added benefit that the charge-discharge experiment need not be interrupted. Note, however, that reliable E_{oc} data can only be collected using UMEs with relatively facile electron-transfer rates for the electrolyte of interest (e.g., Pt in this case); otherwise the electrode will pass nearly zero current flow over a wide range of electrode potentials, yielding ambiguous E_{oc} values. We also observed a distinct time lag between the maximum or minimum SOC implied from E_{oc} values in the analytical cell and the point at which the RFB changed charge direction.

This is consistent with the finite time interval required for electrolyte to flow between the RFB and the analytical cell; additional time lag may also result from incomplete mixing associated with laminar flow in the system, which would be worth characterizing further in future studies.

In the measurements shown in Panel 6b, the E_{oc} values varied from 0.377 to 0.443 V vs. Ag/AgCl. The midpoint of this potential range can be taken as an empirical estimate of the formal potential $E^{0'}$ under the assumption that the capacity-limiting electrolyte charges and discharges over SOC values that are symmetric about 50 % (such an assumption is generally valid as long as the fundamental transport properties of the electrolyte do not change significantly as a function of SOC). This is convenient because temporal changes in the apparent $E^{0'}$ over the course of a charge–discharge experiment, or from run to run, could be indicative of an electrolyte degradation or reference electrode drift. Indeed, we found that $E^{0'}$ varied from a minimum of 0.32 to a maximum of 0.57 V vs. Ag/AgCl over 15 experimental runs executed with a single Ag/AgCl reference electrode, but we did not observe significant drift during any single run.

Alongside the ability to visualize and quantify changes in the electrolyte composition, voltammetry measurements in the analytical cell can be used to measure and compare electron-transfer rates across different UME compositions and surface treatments. Panel 6c depicts current vs. applied potential in the voltage range bracketing the open-circuit potential for Pt and carbon fiber UMEs, where the carbon fiber electrodes were measured before and after surface activation using an electrochemical oxidation procedure that we studied previously on glassy carbon macroelectrodes[106]. These data were extracted from continuous voltammetry measurements by selecting the voltammograms that were nearest to $SOC = 50$ %. Despite the modest difference in E_{oc} in these datasets, the slope of current density vs. potential clearly shows that electron transfer rates varied in the order Pt > oxidized carbon fiber > pristine carbon fiber, in qualitative agreement with our prior findings[106, 113].

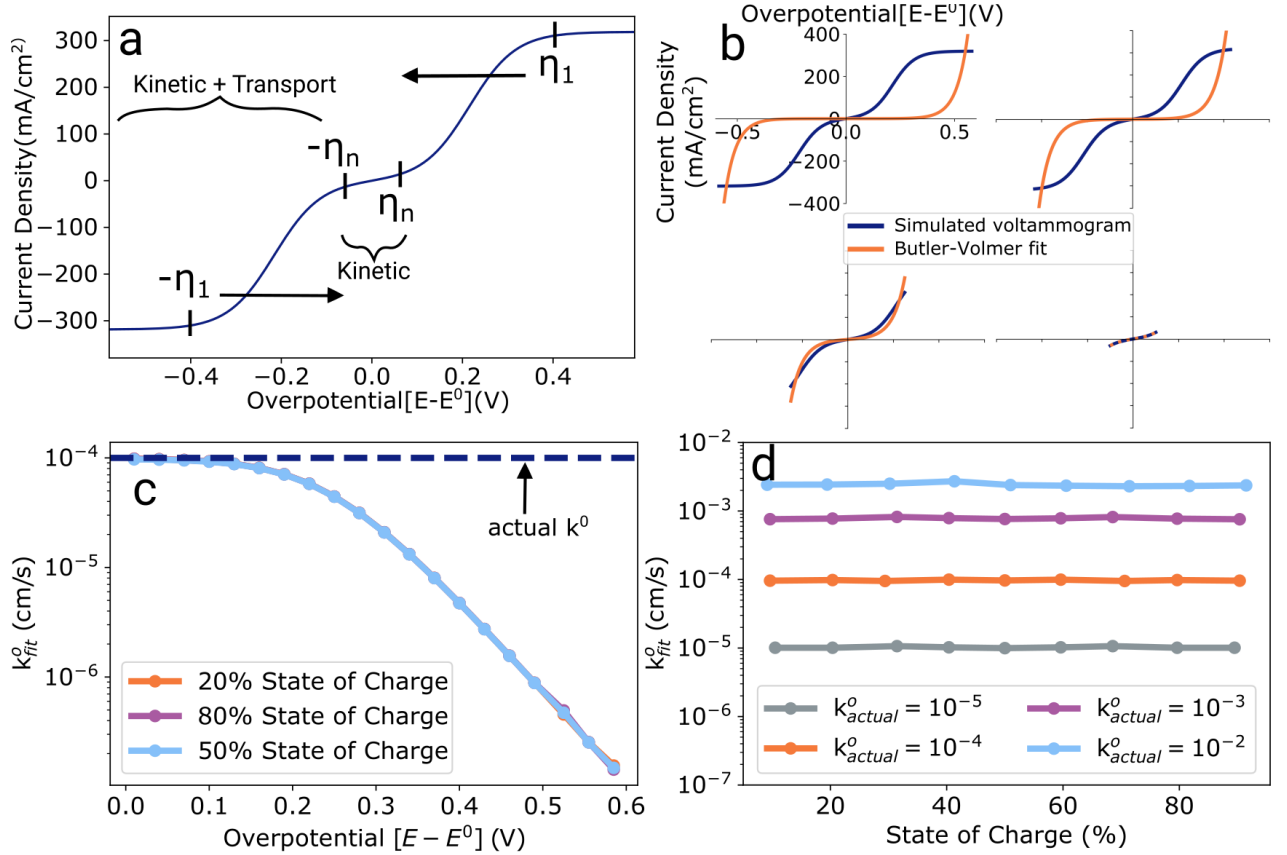


Figure 7: Empirical workflow for the shrinking overpotential method: (a) iteratively decreasing the range of overpotential values over which a kinetic fit is applied results in a progressive transition from the mixed transport-kinetic regime to the kinetically controlled regime; (b) examples of individual fits to the Butler-Volmer equations as the fitted overpotential range shrinks; (c) k_{fit}^0 vs $|\eta|$ data showing a monotonic increase in the apparent rate constant followed by asymptotic approach to the true value (note that 3 states of charge are shown, but the data overlay so that only the 50 % SOC line is evident); (d) compiled maxima for k_{fit}^0 data as in panel (c) over SOC values ranging from 10 to 90 % and k^0 values from 10^{-5} to 10^{-2} cm/s. Current versus overpotential data used for these fits were derived from finite difference simulations using DigiElch software. Full details are included in the Electronic Supplementary Information.

2.3.3 Quantifying Electron Transfer Rates

We further sought to quantify the differences in electron-transfer kinetics across the 3 electrode types used in this study. We were specifically interested in devising a general approach to extract k_{eff}^0 values from UME voltammetry data that overcomes some of the challenges outlined in the Introduction section. Figure 7 illustrates the approach we adopted, which we term the shrinking overpotential method, by applying it to voltammetry data that were simulated using finite difference techniques using a commercial software tool called DigiElch[114].

The approach involves first picking a set of overpotential values, $\pm\eta_1$, at or near the outer bounds of the range of available data and symmetric about the equilibrium formal potential of the redox couple of interest (panel 7a). We then perform a least-squares regression of these data to the Butler-Volmer equation, which describes current vs. overpotential relationships in the absence of transport and resistive losses.

$$J = nFk^0 \left[C_{\text{ox}} \exp\left(\frac{-\alpha F\eta}{RT}\right) - C_{\text{red}} \exp\left(\frac{(1-\alpha)F\eta}{RT}\right) \right] \quad (2.3)$$

Hence, transport and resistive limitations result in a systematic under-estimate of k_{eff}^0 .

We then iteratively decrease the overpotential range ($\pm\eta_n$) and reapply the fitting routine, ultimately converging on a fit applied only to the region in the near vicinity of $E^{\circ'}$ (panel 7b). During this iterative process, the apparent k_{eff}^0 value and the goodness-of-fit increases as the overpotential range shrinks to encompass current densities that are dominated by kinetic contributions to overpotential. Ultimately, the k_{fit}^0 values that result from the fit converge on a maximum that can be taken as the “true” value of k_{eff}^0 (panel 7c).

In fact, this maximum value of k_{fit}^0 is only a valid estimate of k_{eff}^0 if it is smaller than the characteristic mass transfer rate in the analytical cell. When electron transfer rates “outrun” the rate of mass transfer, the result is a systematic underestimate of k_{eff}^0 (panel 7d) such that the maximum value of k_{fit}^0 can only be taken as a lower-bound. Indeed, is possible to estimate a reasonable “upper speed limit” of k_{eff}^0 values that can be measured accurately in this way by converting k_{eff}^0 to an exchange current density,

$$J_0 = nFk_{\text{eff}}^0 \frac{C_{\text{ox}} + C_{\text{red}}}{2} \quad (2.4)$$

which must be smaller than the mass-transfer limited current density J_{lim} to yield a valid estimate of k_{eff}^0 . The exact amount that J_0 must be smaller than J_{lim} depends on the amount of error that can be tolerated, but we consider $J_{lim} \geq 3J_0$ to be a reasonable requirement. In the case of the simulated data in Figure 7, $J_{lim} = 3J_{0,eff}$ when $k_{eff}^0 = 2 \times 10^{-3}$ cm/s; hence, k_{fit}^0 values begin to diverge from the true value around $k_{actual}^0 = 10^{-3}$ cm/s and above (panel 5d).

The shrinking overpotential approach has several beneficial features that make it useful for characterizing electron-transfer rates for RFB electrolytes. The first is that it requires only one set of current-overpotential data to estimate k_{eff}^0 , and the accuracy of this estimate is not sensitive to varying battery stage of charge at least over the range from 10 to 90% (as illustrated in panels 7c and d). This makes it possible to measure reaction kinetics rapidly and continuously using voltammetry data like those shown in Figure 6. This type of data is easy to collect using inline flow cell measurements (using working electrodes of any size) or using battery electrodes directly, provided the potentials can be converted to overpotentials using a suitable reference.

Second, this approach also does not require any knowledge about the mass-transfer limited current density, nor does it require that the range of applied potentials extend all the way to the mass-transfer limited regime. This makes it possible to extract valid kinetic information even from battery systems in which mass-transfer limited rates cannot be accessed.

In the limit of $\pm\eta_n \rightarrow 0$, the shrinking overpotential method is mathematically identical to the polarization resistance method,[115] which uses a linear approximation of the Butler-Volmer equation to extract electron-transfer rate constants from the micro-polarization region around the equilibrium potential. However, our approach is more robust in that it allows us to empirically identify and use the entire region in a set of voltammetry data over which kinetics dominates the overpotential response. The ability to extend the fit to wider overpotential ranges (and extending even to where the current response does not remain linear) reduces the negative impact of background processes like side reactions and capacitance, which can dominate the electrode response at very low overpotentials and currents.

The shrinking overpotential method also provides a useful mechanism to determine that the reaction rate may be so fast that k_{eff}^0 simply cannot be reliably measured. The hallmark of this behavior is a persistently sloping $|\eta_n|$ vs. k_{fit}^0 response with no clear asymptote. Moreover, the shrinking overpotential method should be flexible enough to facilitate the use of more complex kinetic models, including those involving multi-step catalytic mechanisms that may not be amenable to linearization in the same way as the Butler-Volmer equation.

2.3.4 Experimental Kinetics Characterization

Finally, we applied the shrinking overpotential method to the voltammetry data we collected in the analytical cell at Pt, carbon fiber, and oxidized carbon fiber UMEs. Figure 8 compiles representative results, and complete results are included in the Electronic Supplementary Information of the published manuscript.

Panel 8a depicts representative $|\eta|$ vs. k_{fit}^0 data for each electrode type at 50 % SOC from near the beginning of a 5-cycle experimental run. Each dataset yields the expected increase in k_{fit}^0 as the overpotential range shrinks. The general trend is also consistent with prior results, where pristine carbon fiber electrodes yielded the slowest electron-transfer rate and Pt electrodes yielded the highest[106, 113]. However, these data generally did not yield clear asymptotes in k_{fit}^0 at small values of $|\eta|$; we attribute this to the prevalence of background capacitance and electrical noise in the voltammetry measurements, which result in poorer fits and noisier k_{fit}^0 results as the fitted overpotential range shrinks to encompass only a few data points. This problem is likely exacerbated by the use of UMEs, which give sub-nA current flow near E_{oc} , making measurements especially sensitive to vibrations and electrical interference.

Panel 8b demonstrates a full set of k_{eff}^0 vs. time data for a Pt UME during a 5-cycle charge-discharge experiment, where k_{eff}^0 was taken as the maximum value of k_{fit}^0 in the shrinking overpotential analysis. These data have been further plotted against SOC, which was extracted from E_{oc} data in the analytical cell. Here an intriguing set of trends emerge, where k_{eff}^0 increases and decreases with SOC (i.e., higher concentrations of Fe^{3+} yields faster rate and vice-versa) and the overall range of k_{eff}^0 values also increases by a factor of 2–3

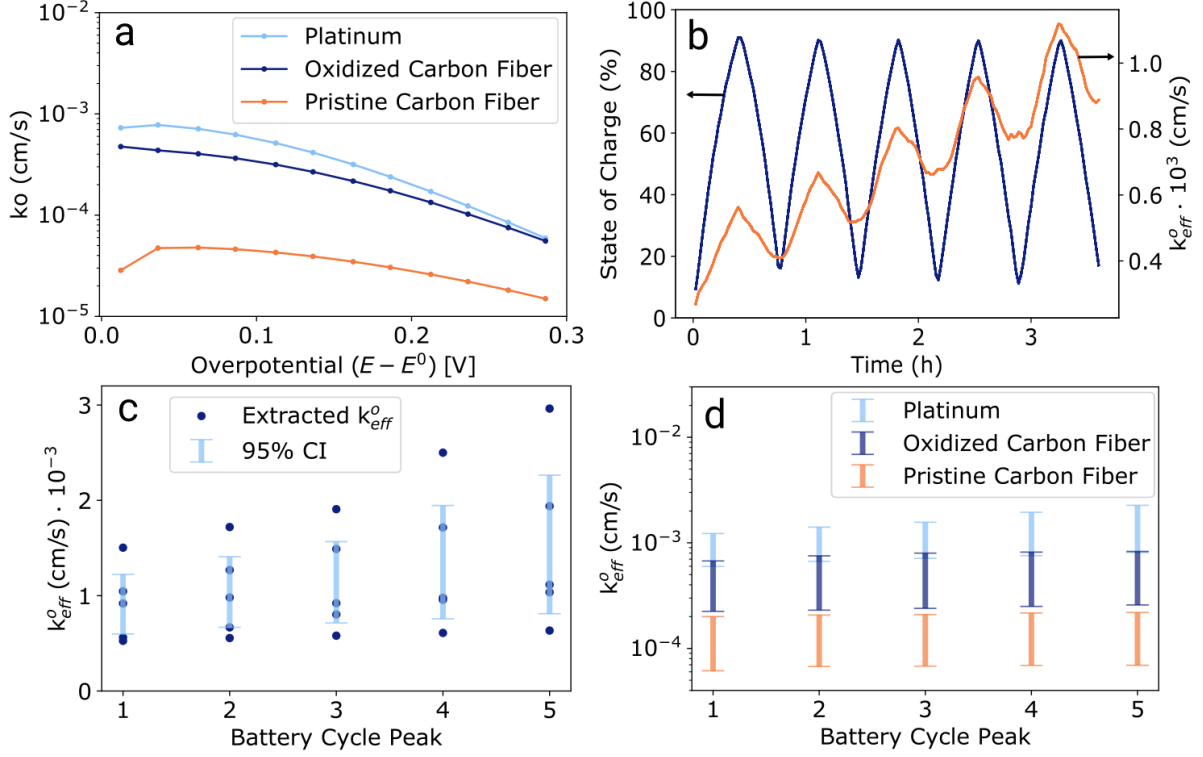


Figure 8: Empirical kinetics data for three types of UME electrode in $\text{Fe}^{3+/2+}$ RFB electrolyte: (a) representative k_{fit}^0 vs. $|\eta|$ data for Pt, pristine carbon fiber, and oxidized carbon fiber electrodes extracted from voltammograms near 50 % SOC; (b) k_{eff}^0 and SOC vs. time data for a single Pt UME, where k_{eff}^0 was taken as the maximum value of k_{fit}^0 as depicted in (a); (c) compiled k_{eff}^0 values extracted from the time points corresponding to the maximum SOC values for 5 separate experimental runs using a Pt UME, along with statistical estimates of the upper and lower bounds at a 95 % confidence interval; (d) upper and lower bounds as in (c) for each of the three noted electrode types.

over several hours. The latter result was consistent across multiple Pt measurements, which leads us to conclude that the Pt surface is modified by Fe^{3+} (e.g., via etching or surface functionalization) in a way that favorably impacts the associated reaction kinetics. Both types of carbon electrode also yielded k_{eff}^0 values that varied systematically with SOC, but neither showed persistent changes in k_{eff}^0 over time. Hence, we tentatively conclude that the SOC-dependence of k_{eff}^0 is an artifact that also results from the influence of electrical noise and background capacitance on the regression fit. Neither capacitance nor random noise were included in the simulated data in Figure 7, and they might be expected to have a larger impact at more extreme states of charge since the magnitude of the anodic and cathodic current flows are small at high and low SOC, respectively.

Panel 8c compiles k_{eff}^0 values extracted from their peaks at the maximum SOC across all 5 charge–discharge runs. Again we see clear evidence for increasing rate constant, but the relative variation in initial k_{eff}^0 is comparable in magnitude to the relative change in rate constant over time. Additional statistical analysis, in which we have estimated upper and lower bounds of k_{eff}^0 at a 95 % confidence interval, mainly show an increased spread in the data (albeit asymmetrically biased in the positive direction) as the Pt UMEs were cycled continuously in $\text{Fe}^{3+/2+}$. Moreover, these results all fall in the range of $k_{\text{eff}}^0 \sim 10^{-3}$ cm/s, which is near the upper bound of what can be accurately measured with $J_{\text{lim}} \sim 1$ A/cm². Accordingly, the primary finding agrees with our prior work showing that Pt electrodes catalyze $\text{Fe}^{3+/2+}$ redox chemistry very efficiently and may become even more efficient upon extended cycling.

Panel 8d compiles the equivalent bounded range of k_{eff}^0 values with 95 % confidence intervals across all three electrode types. These data demonstrate that, despite run-to-run variation, we are able to estimate electron-transfer rate constants within a precision of approximately a factor of 3, or half an order of magnitude. These data also clearly show that pristine and oxidized carbon electrodes give stable reaction kinetics over at least 3–4 hours of continuous cycling. Moreover, oxidized carbon fiber UMEs catalyze $\text{Fe}^{3+/2+}$ oxidation/reduction 3–4 times more efficiently than pristine carbon fiber UMEs. Indeed, we speculate that k_{eff}^0 values of $4\text{--}5 \times 10^{-4}$ cm/s shown by oxidized carbon fiber are fast enough to translate to negligible overpotential losses at operating current densities in the hundreds

of mA/cm² when combined with the ability to increase roughness factor (electroactive area normalized to superficial area) by 10–100 fold using porous carbon fiber electrodes[116]. Nonetheless, key outstanding questions include whether reaction kinetics and electrode stability remain constant over much longer timescales, and whether kinetics measurements made at UMEs can be extrapolated to technologically relevant RFB electrodes.

2.4 Conclusions

We have described here the construction and operation of a channel-flow UME analytical platform for executing continuous voltammetric measurements inline with the operation of a functional RFB. Operating the battery in an unbalanced, compositionally symmetric configuration enables stable cycling while simultaneously measuring the temporal evolution of electrolyte composition and reaction kinetics in the coupled analytical cell. We have also demonstrated a method for extracting electron transfer rate constants from hydrodynamic voltammetry data that overcome several of the key challenges associated with conventional techniques, particularly the need to make explicit measurements of mass-transfer controlled reaction rates. This approach benefits from very high rates of mass transfer achievable with UMEs, but it should be applicable to other electrode and cell geometries provided there exists a potential region over which the current-overpotential behavior is dominated by kinetics. Rate constants for Fe^{3+/2+} chemistry were found to vary in the order Pt \approx oxidized C \approx pristine C, in good agreement with prior work using stationary and rotating-disk electrode voltammetry. Pt electrodes were further found to increase in catalytic activity over at least several hours, albeit with increasing variability over time.

These results, along with the ability to estimate rate electron transfer rate constants with a precision of approximately half an order of magnitude, make us confident that these approaches will be broadly useful for further applications in RFB materials discovery. Accordingly, this work sets the stage for future studies aimed at tackling several key research questions and outstanding challenges. Chief among these is whether it is possible to develop cost-effective electrode materials that minimize kinetic losses for any RFB chemistry

of interest. Studies along these lines will benefit from the ability to make extended measurements directly alongside flow battery operation, but it remains to be seen whether the range of electrode compositions that are accessible in UMEs can accurately replicate the surface chemistry of practical RFB electrodes. Another challenge involves the use of commercial, liquid-filled reference electrodes, which we found to be a weak point due to the tendency for their potentials to drift under extended experimentation in harsh HCl-based electrolytes. Similar challenges are likely to be encountered in many RFB electrolytes, particularly non-aqueous RFBs for which reference electrodes are even less well standardized. Extensions toward electrolytes that are oxygen sensitive will also likely require modifications to the experimental apparatus to exclude atmospheric air. These are certainly worth tackling in the interest of advancing flow batteries and continuous-flow electroanalytical techniques more broadly.

3.0 Enhancement of the $\text{Cr}^{3+/2+}$ Redox Reaction in Saturated Salt Solutions

This chapter outlines the exploratory work I completed to enhance the $\text{Cr}^{3+/2+}$ redox reaction using saturated salt solutions. I was solely responsible for all of the experiments carried out in this study and the data analysis of those experiments. The study remains incomplete, but continued work by my successors in the McKone lab will allow us to make a significant intellectual impact on electrolyte systems for aqueous flow batteries.

3.1 Introduction

As previously stated in the introduction of Chapter 2, redox flow batteries have drawn interest to serve as an alternative to Li-ion batteries for grid scale energy storage because they safely display a high charge per unit area.

Currently, vanadium RFBs remain the most established technology in the the field. Vanadium RFBs are beneficial to energy storage because they allow for the battery to operate within the voltage window where water is thermodynamically stable [117, 118, 33]. Another benefit to vanadium RFBs is that the fully interconvertable positive and negative redox couples in all vanadium RFBs, $\text{V}^{3+/2+}$ and $\text{V}^{5+/4+}$, are immune to irreversible capacity fade, allowing the battery to last over many charge and discharge cycles [31]. However, as previously discussed, vanadium has a high materials cost which makes them hard to bring to industry. Technoeconomical analysis have shown that the materials cost for RFBs should be $\sim \frac{1}{3}$ the material cost of vanadium [25, 27, 119, 120].

Since vanadium RFBs became the focus of modern RFB technology, many other cost competitive materials have been explored as a cheaper alternative. The Zn/Br battery allows for high energy density due to the elimination of one electrolyte volume and operating at a relatively high voltage[121, 36]. The H_2/Br RFB is of particular interest because it displays high energy densities in a RFB both with and without a membrane[122, 123]. One reason anthraquinone disulfonate (AQDS) RFBs are being explored is that AQDS is easily

dissolved in pH neutral electrolyte, removing the need for strong and potentially harmful acids. This organic compound is unique in the sense that it remains stable after undergoing reversible redox reactions with 2 electrons per molecule.[124, 125]. Lastly, the original RFB NASA developed, the Fe/Cr RFB is made of earth abundant materials which keeps the cost low.[126, 127]. Because of the long history and potential for low cost in Fe/Cr RFBs, this material system became the major focus of my work.

Despite Fe/Cr RFBs having such low materials cost, this type of cell has many disadvantages. Because the RFB has different materials on the anodic and cathodic sides of the cell, a concentration gradient over the cells membrane subjects the cell to crossover and ultimately, a loss of capacity [126, 36]. The electrolyte is also susceptible to the hydrogen evolution reaction (HER) because it is commonly coupled with an HCl supporting electrolyte. Formation of H_2 gas is not ideal for RFBs because it is flammable and decreases the amount of charge achievable by the battery. Further susceptibility is reported due to chromium itself being a catalyst for HER [127, 32]. Lastly, the $Cr^{3+}/2+$ redox couple is not readily reversible without a catalyst of its own, as described in the Preliminary Results section below.

Research and technologies for electrochemical experiments to create a large stability window have recently been underway. Boron doped diamond electrodes are a newer type of carbon electrode that allow for a potential window expansion of 400 to 800 mV compared to that of the glassy carbon electrode [128, 129]. Water-in-Salt (WiS) electrolytes have shown potential window expansions of up to 900 mV on a glassy carbon electrode, dependent on the electrolyte salt concentration [130, 131]. Methods for changing the local pH around the electrode and hindering HER and OER based on the relative activity variable in the Nernst equation have also been explored [132, 133]. The availability to expand the stable potential range for an operating electrode leads us to a key question: could expanding the potential range of an electrode, especially in the range where we observe the onset of HER, allow for increased kinetics of the $Cr^{3+}/2+$ redox reaction?

Recent research by Van Hecke et al. used mathematical simulations to create a theoretical UV-Vis spectra for Cr^{3+} in different surrounding environments. Results from this study showed that Cr^{3+} speciates differently when exposed to varying concentrations of chloride-containing solutions. Specifically, in the presence of LiCl, theoretical data showed different

optical properties of the Cr^{3+} species. This suggests that one or more complexes of chromium can be formed depending how saturated the solution becomes with LiCl salt [134]. This raises another key question: are some of these chromium complexes better at doing reversible electrochemistry than others?

In this work, we studied the stability window of platinum, gold, and carbon electrodes by using saturated LiCl and NaCl solutions in water. Further, we looked into how these saturated salt solutions affected the $\text{Cr}^{3+/2+}$ redox reaction on these respective electrodes. Cyclic Voltamograms (CVs) of different NaCl and LiCl concentrations were taken to determine the stability window. Based on that stability window, a determination was made about whether we should expect to see $\text{Cr}^{3+/2+}$ ($\sim -0.61\text{V}$ vs. Ag/AgCl) redox chemistry in the new stability window for each electrode or whether that potential range would still be dominated by HER. Further, we also worked to validate the theoretical Cr^{3+} speciation discussed above by examining the optical properties of Cr^{3+} using UV-Vis. Lastly, for the electrodes where $\text{Cr}^{3+/2+}$ chemistry was obvious, we began a process to extract kinetic data about the redox reaction using cyclic voltammetry data.

3.2 Preliminary Work: Unsuccessful Attempts to Replicate Key Results from NASA

The basis of the work in Chapter 3 comes from the origin of RFBs themselves. NASA invented RFBs as an economical alternative to store grid scale energy. Over the span of roughly a decade in the 1970s and 80s, researchers at NASA and several U.S. universities collaborated on creating and optimizing the iron-chromium (Fe/Cr) RFB. In 1983 they released a final report communicating that working on this RFB project was no longer in their best interest[126]. In the final review they published key findings from the research, which included the assembly of the first fully functional RFB and the challenges they had faced in getting to that point [126]. A schematic of their RFB can be seen in Figure 9a and a photo of their actual cell is pictured in Figure 9b [126].

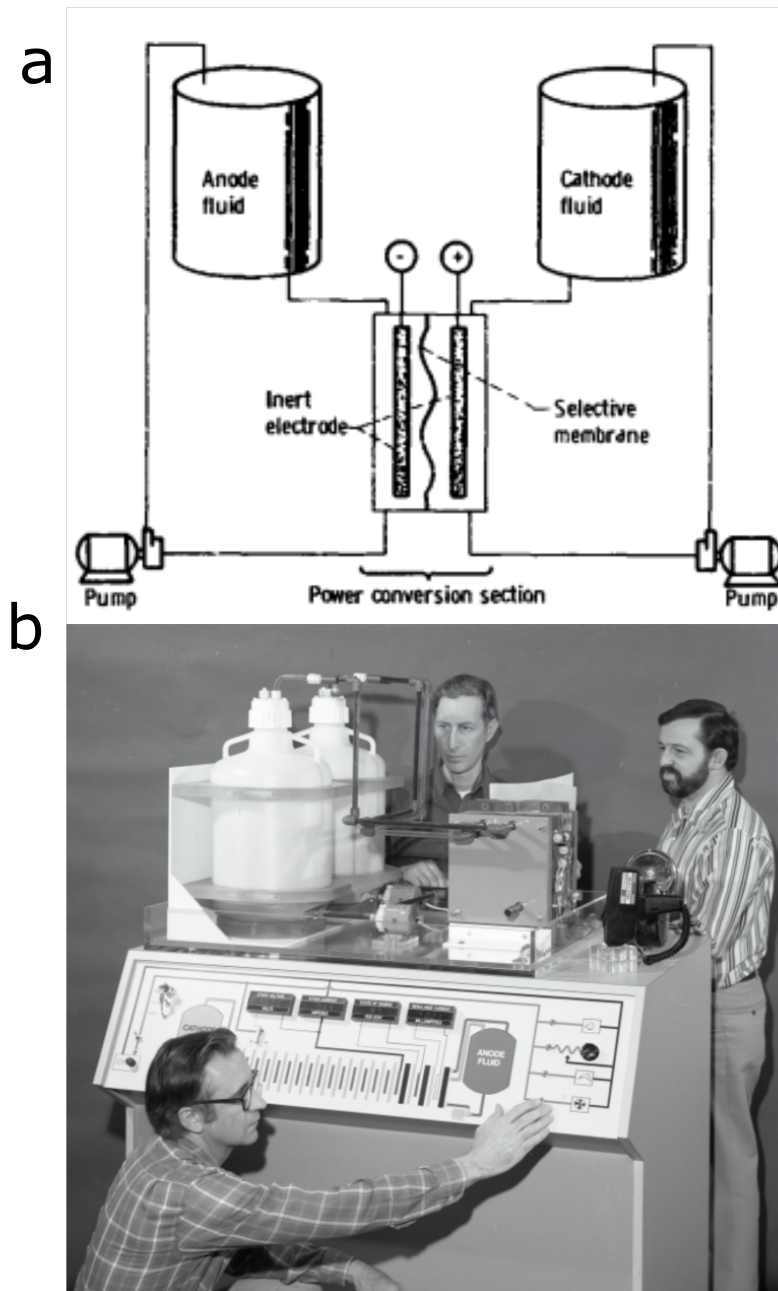


Figure 9: Adapted from NASA Redox Storage System Development Project - Final Report. Illustrates NASA's original Fe/Cr RFB schematic and a live visual of the cell apparatus [126].

The first challenge NASA faced was eliminating the crossover from the opposing Fe and Cr sides of the RFB through the membrane. By placing only Fe and Cr on their respective sides of the battery membrane, a concentration gradient was formed. The Fe and Cr species diffused across the membrane to reach a transport equilibrium. This phenomena is known in the flow battery field as crossover. As crossover occurs, the maximum theoretical capacity a battery can achieve decreases because the concentration of ions on either side of the cell is decreasing. To solve this problem, mixed electrolytes containing both Fe and Cr were placed initially on both sides of the cell. Because the $\text{Fe}^{3+/2+}$ redox reaction thermodynamically occurs at positive potentials and the $\text{Cr}^{3+/2+}$ redox reaction thermodynamically occurs at negative potentials, NASA was able to control which half of the battery cell underwent the desired reaction based on the potential they applied. Essentially, the second species on each side of the battery becomes a spectator ion, but doing this also removes any driving force for crossover by a concentration gradient between different sides of the battery cell. The significance of this discovery is that the overall cell capacity does not decrease because of diffusion across the cell [126].

The second main challenge the NASA researchers faced was enhancing the sluggish kinetics of the $\text{Cr}^{3+/2+}$ redox chemistry. Based on my own work, I believe that this was a more daunting challenge. Sluggish kinetics are bad for an Fe/Cr RFB because they reduce the overall efficiency of the cell. Another problem with using Cr as a redox species is that it has a highly negative standard reduction potential, -0.42V vs. RHE, and Cr itself is known as catalyst for hydrogen evolution. An applied potential negative of 0V vs RHE would already induce the HER, adding a catalyst only would only enhance the kinetics [135, 136]. If the HER is competing with the $\text{Cr}^{3+/2+}$ redox reaction, and the presence of Cr itself is catalyzing the HER, neither of the reactions will reach their full kinetic potential. However, HER will appear as the dominant reaction. When it comes to collecting data, in some of my failed exploratory experiments, HER seems to be dominating at potentials where we expect to see the $\text{Cr}^{3+/2+}$ redox reaction.

The NASA Fe/Cr RFB research team therefore undertook extensive work on electrode engineering to suppress the HER. They tested a variety of catalysts known to hinder HER, including lead, bismuth, and gold in hopes of increasing the selectivity of the negative electrode for the $\text{Cr}^{3+}/2+$ reaction. In their final report, they were successful in demonstrating reversible $\text{Cr}^{3+}/2+$ chemistry on a carbon felt electrode[126]. However, my attempts to replicate these results had unexpected outcomes, as discussed in the following section.

3.2.1 Reproducing $\text{Cr}^{3+}/2+$ Redox Chemistry on Carbon Felt

Some of the first experiments I ran as a graduate researcher were to reproduce $\text{Cr}^{3+}/2+$ redox chemistry on carbon electrodes as NASA had described in their review. The first set of experimental data can be seen in Figure 10 (a), where a 14.5 cm^2 carbon felt electrode was soaked in methanol for 30 minutes, before being rinsed with tap water, and dried with laboratory wipes. The felt was then heated in 45% KOH at 100°C for 2 hours. The felt electrode was then rinsed again with DI water before soaking in a beaker with DI water overnight. Then, the felt was damp dried and moistened evenly with a 25 % water 75% methanol solution containing $62.5 \mu\text{g/ml}$ of $\text{HAuCl}_3 \cdot 3\text{H}_2\text{O}$.

The felt stood overnight in solution and was kept from the light. It was next dried in an oven at 100°C for 4 hours and then heated for 2.5 hours at 265°C . The felt was then wet with 2M HCl and placed in a redox cell for analysis. This pretreatment method comes directly from the NASA report[126]. The pretreatment method is supposed to deposit gold nanoparticles into the carbon electrode to serve as a catalyst for the $\text{Cr}^{3+}/2+$ redox reaction. However, as we see in Figure 10 (a), the pretreated electrode in a 0.1M Cr^{3+} , 2M HCl solution, we see no clear oxidation or reduction peak for the $\text{Cr}^{3+}/2+$ redox couple where I had expected to observe it at -0.61V vs Ag/AgCl. Furthermore, we see this potential range instead appears to give about 5 mA/cm^2 current density of HER. When trying to reproduce the results by NASA using their own electrode treatment method, I was unsuccessful in achieving reversible $\text{Cr}^{3+}/2+$.

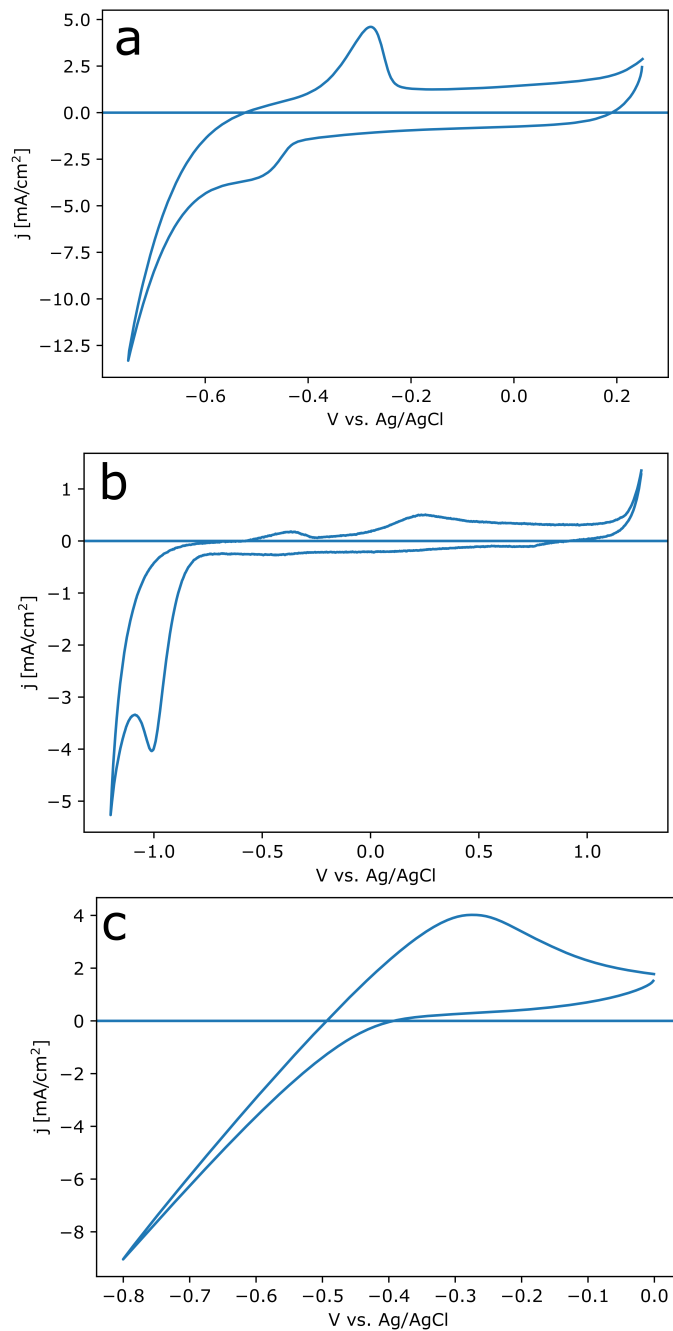


Figure 10: Preliminary experiments in attempts to suppress HER and improve $\text{Cr}^{3+/2+}$ redox chemistry on different types of carbon electrodes. In a) a carbon felt electrode pretreated using the NASA procedure in [126]. In b) on a glassy carbon electrode and in c) on a glassy carbon electrode in the presence of Pb(II) Nitrate.

In Figure 10 (b), I used a regular glassy carbon electrode to see if a higher concentration of Cr^{3+} had an affect on the redox reaction at the electrode surface. I increased the concentration of Cr^{3+} to 1M dissolved in 2M HCl. Despite the high Cr^{3+} concentration, in Figure 10 (b), there is no obvious evidence for a $\text{Cr}^{3+/2+}$ redox reaction. There are some new peaks compared to the previous reaction in Figure 10 (a), but at the time I had never seen any form of $\text{Cr}^{3+/2+}$ redox chemistry outside of the clear and obvious voltammograms reported by NASA and these peaks were unclear to me. So, I decided to further try and suppress HER in Figure 10 (c) using the presence of Pb (II) Nitrate, a compound known to suppress HER, on a glassy carbon electrode in the presence of 0.1M Cr^{3+} [126]. The results were similar; the only evidence we observed for reduction reactions appeared to be HER. From this point, I went back to the drawing board before implementing a new way to suppress HER by employing an RFB electrolyte containing very high concentrations of LiCl(aq) , as explained in detail in the following sections.

3.3 Experimental Methods

A 10.42M LiCl solution was made by adding 100g of LiCl salt (Alfa Aesar) into a Schott Duran bottle that was diluted to 150mL total volume with water. The solution had to be swirled vigorously until the salt became completely dissolved. The reaction between water and LiCl is exothermic so be careful, the bottle will get hot!

2M Cr^{3+} was made by weighing 15.84g of $\text{CrCl}_3 \cdot 6 \text{H}_2\text{O}$ (Alfa Aesar) and diluting to 50mL in a 50-mL plastic centrifugation tube (hereafter referred to as a falcon tube). The tube was shaken and sonicated until no salt could be seen at the bottom.

Aliquots of both the 2M Cr^{3+} solution and 10.42M LiCl solutions were used to make .1M Cr^{3+} and varying concentrations of LiCl solutions. For example, a solution containing 21mL of 7M LiCl and .1M Cr^{3+} was made by taking 1.5 mL of the 2M Cr^{3+} solution combined with 14.7mL of the 10.42M LiCl solution. The combined solution was then diluted to 21mL with DI water in a falcon tube to reach the desired concentrations. Similar processes were repeated for 10M, 9M, 8M, 5M, 2M, and .1M LiCl solutions containing .1M Cr^{3+} using different amounts of DI water and 10.42M LiCl to get 21mL total of the desired solution.

UV-Vis experiments were completed using a 1 mL capacity, 10 mm pathlength, quartz UV-Vis cuvette (Cole Parmer). UV experiments were run on .1M Cr^{3+} in 12M HCl (Alfa Aesar), 6.24M NaCl in water, and 10.42M LiCl in water. The NaCl solution was made by using 18.23g of NaCl (Alfa Aesar) and diluting to 50mL with DI water in a falcon tube. UV-Vis (Agilent, Cary 60) experiments were taken over wavelength range from 200 to 800 nm.

To run cyclic voltammetry experiments, preliminary cleaning of the surface of working electrodes is required to ensure a flat surface area and that no redox active particles are stuck to the electrodes surface. To properly polish a working electrode, polishing cloth should be cut and placed inside of a Pietri dish. Next, deposit 1um Alumina polishing powder onto the polishing cloth and add some DI water droplets until the powder forms a slurry with the water. Next, take the working electrode of choice for the experiment and place it into the slurry of 1um Alumina powder on the polishing cloth, flush with the surface. Rotate the electrode in a clockwise and counter clockwise circular motions for 20 rotations each. Rinse the electrode with water after completion. Repeat this process for with .3um and .05um alumina slurries, respectively.

CVs for this study were taken using a Gamry Reference 1000 potentiostat. The apparatus for the CVs consisted of a scintillation vial with a Teflon cap secured by an arm clip on a ring stand. The Teflon cap allowed for the insertion of 3 electrodes. The working electrodes used for these experiments were interchangeable and consisted of gold, platinum, and glassy carbon disk electrodes with a surface area of .09cm² (CH Instruments). The counter electrode was a graphite rod (Alfa Aesar) and the reference electrode was Ag/AgCl (CH Instruments).

Preliminary CVs were run to examine electrochemical stability windows in HCl and Li or Na chloride salt solutions at 100mV/sec. The stable potential window was determined by the potentials at which the electrode reached 1 mA/cm² current density of HER (negative potential limit) and Cl₂ formation (positive potential limit) for glassy carbon and gold. For platinum, the current density limit was taken as 5mA/cm². The CVs taken to determine the reactivity of Cr³⁺ on gold, glassy carbon, and platinum were run at 100 mV/sec over optimal potential ranges that captured the entirety of the desired redox reaction peaks.

For Nicholson kinetic fittings, scan rates ranged from 5 mV/sec to 1280 mV/sec and working electrodes were polished in between each run of altering scan rate. The basis of this fitting method is to examine peak to peak separation. It is therefore important to compensate for resistances that may have an affect on peak to peak separations in a CV. In this case, working with a highly saturated solution of LiCl, there is a high solution resistance associated with the electrolyte. Solution resistance can allow for more current flow than is actually being produced at the electrodes surface[137]. To compensate for this unwanted current, a positive feedback iR compensation was used. Input solution resistance, R_u , values were calculated using the built-in "Get R_u " function before each cyclic voltammetry experiment. 90% of the R_u value was then applied in positive feedback iR compensation for each of the Nicholson cyclic voltammetry experiments[72].

The Nicholson kinetic fitting describes a formula to extract k^o values from a set of cyclic voltammograms as a function of scan rate[72]. The relevant equations for this method are listed below.

$$a = \frac{nF\nu}{RT} \quad (3.1)$$

$$\gamma = \left(\frac{D_O}{D_R}\right)^{1/2} \quad (3.2)$$

$$\Psi = \frac{\gamma^\alpha k_o}{\sqrt{aD_o\pi}} \quad (3.3)$$

Table 1: Variation of Peak Potential Separations with Kinetic Parameters for Cyclic Voltammetry

Ψ^α	$\Delta E_p \times n$
20	61
7	63
6	64
5	65
4	66
3	68
2	72
1	84
0.75	92
0.5	105
0.35	121
0.25	141
0.1	212

In the first equation, variable a is a function of number of electrons transferred, n , Faraday's constant, F , scan rate, ν , the gas constant, R , and temperature, T . In the second equation γ is a ratio of diffusion coefficients. Lastly, in the third equation Ψ is a function of γ , α (assumed to be 0.5 for these studies), the heterogeneous electron transfer rate constant, k^o , the diffusion coefficient, D_o , and a , from the first equation in this section. The value for the empirical variable Ψ is determined from the table above as a function of ΔE_p , the peak to peak separation. From this set of equations, the relationship of Ψ and the inverse square root of ν , the scan rate, should behavior linearly, allowing for the extraction of k^o .

3.4 Results and Discussion

3.4.1 Stability Window Expansion

Figures 11-13 show the stability windows for saturated LiCl compared to HCl on glassy carbon, gold, and platinum electrodes respectively. Figure 14 shows the stability window for saturated NaCl on a glassy carbon electrode. In Figure 11, adding LiCl salt to water expands the stability window of the glassy carbon electrode, where we observe $1\text{mA}/\text{cm}^2$ current density, by an average of ~ 470 mV compared to that of 2M HCl. In Figure 12 the same stability window is observed on a gold electrode, expanding the potential range by ~ 875 mV on average compared to 2M HCl. In Figure 13, for a platinum electrode, the presence of LiCl seems to expand the potential range where $5\text{mA}/\text{cm}^2$ current density is observed by an average of ~ 500 mV. Similarly, in Figure 14 observing various saturations of NaCl, we see a potential range expansion of ~ 620 mV when observing $1\text{mA}/\text{cm}^2$ current density on average compared to 2M HCl on a glassy carbon electrode.

The reason for this change in potential stability window has been the subject of some debate. One idea behind the expansion of the stability window suggests that because there is so much salt dissolved in the water, the larger molecules from the dissolved salt will interact with the surface of the electrode and allow for less active sites where water molecules can interact with the electrode surface, ultimately leading to less water splitting [130, 131]. While this is a plausible theory, there is also literature suggesting that the high salt concentration in water allows for the solvation sphere from the salt ions to form a complex with water molecules, which then decreases the water activity, and thus expands the stable potential range [138, 21].

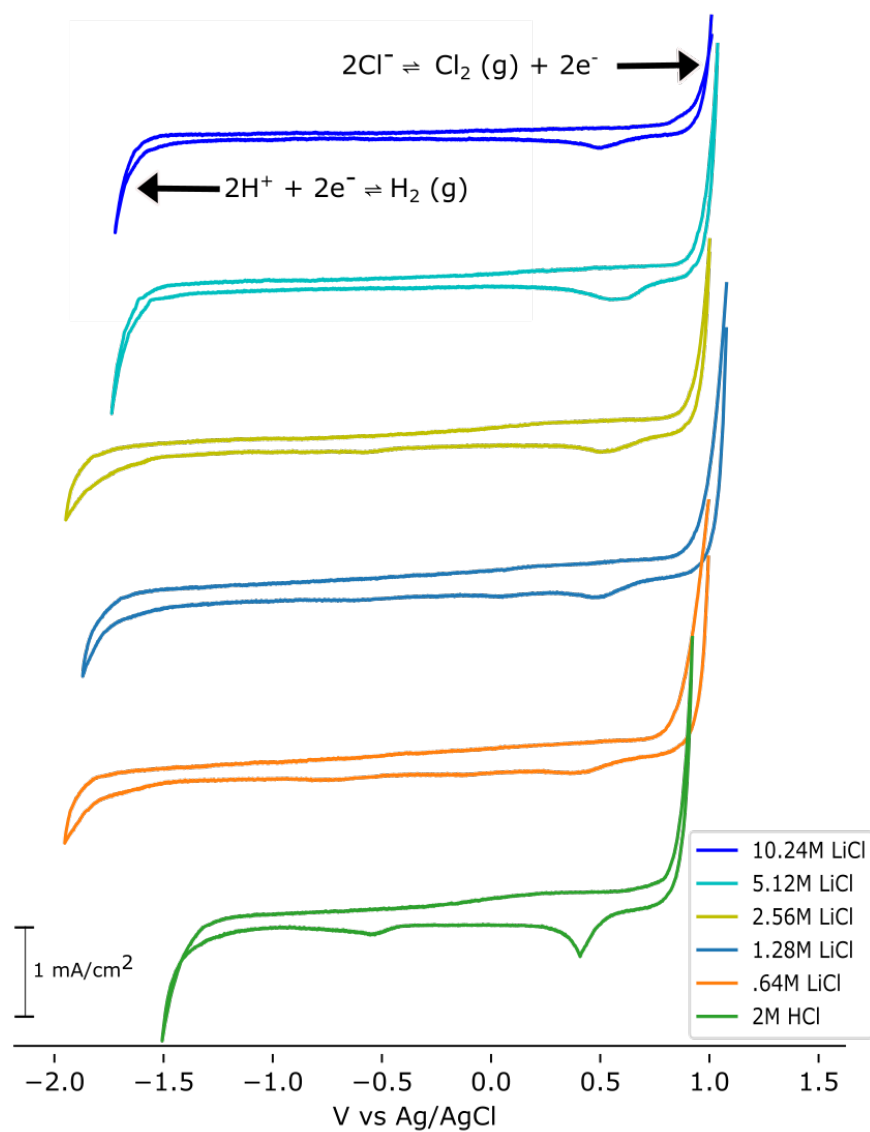


Figure 11: Shows the stability window expansion on a glassy carbon electrode between the HER and Cl_2 formation across different concentrations of LiCl compared to the same reactions in 2M HCl.

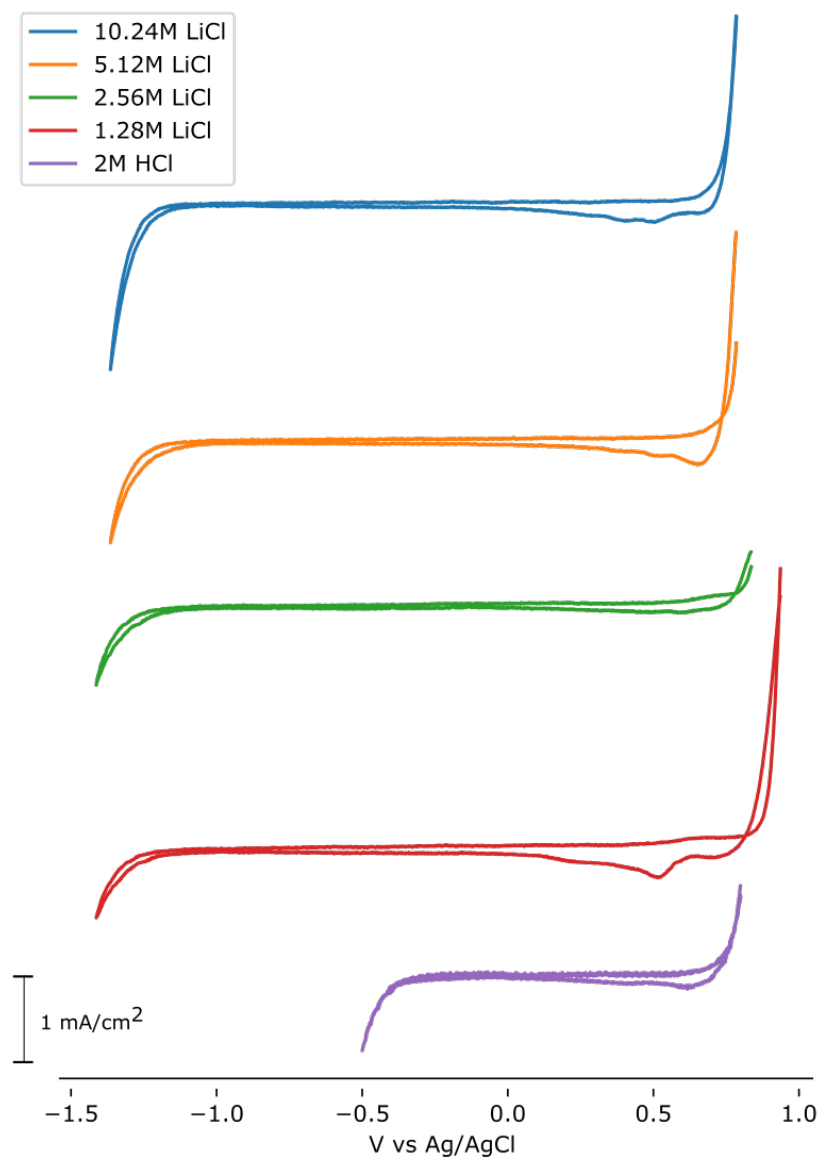


Figure 12: Shows the stability window expansion on a gold electrode between the HER and Cl_2 formation across different concentrations of LiCl compared to the same reactions in 2M HCl.

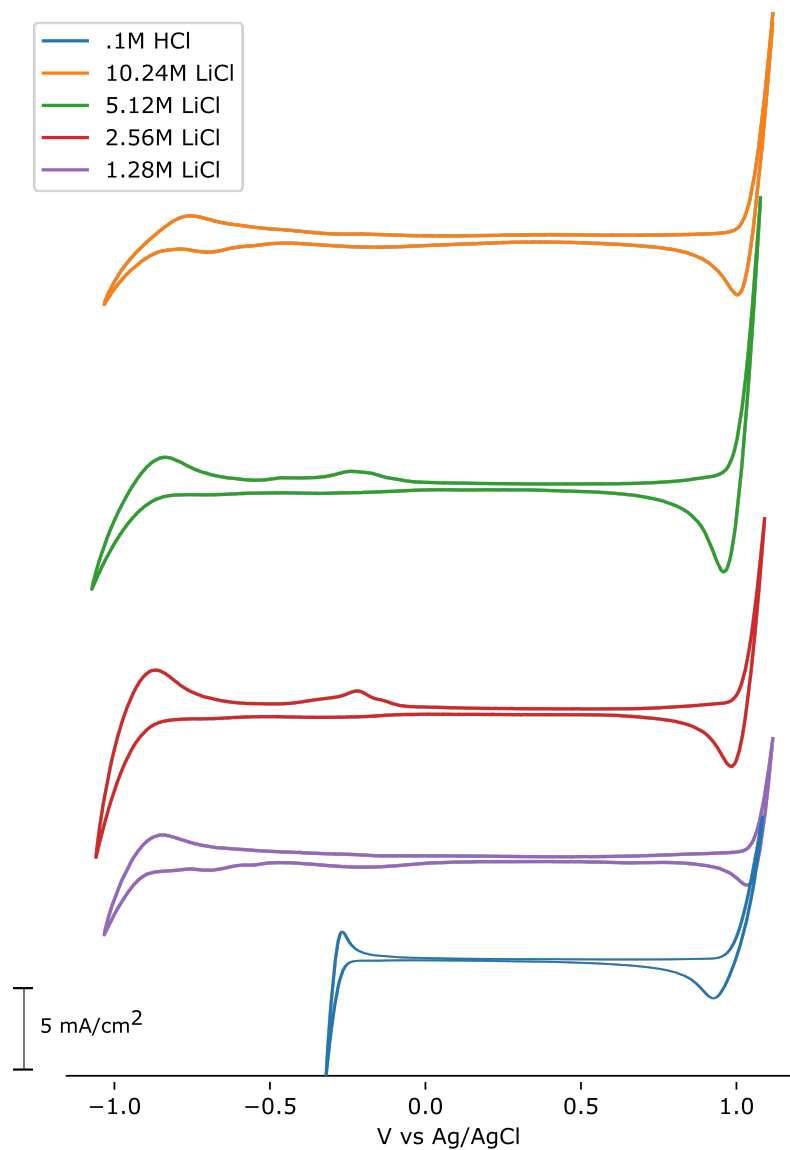


Figure 13: Shows the stability window expansion on a platinum electrode between the HER and Cl₂ formation across different concentrations of LiCl compared to the same reactions in 2M HCl.

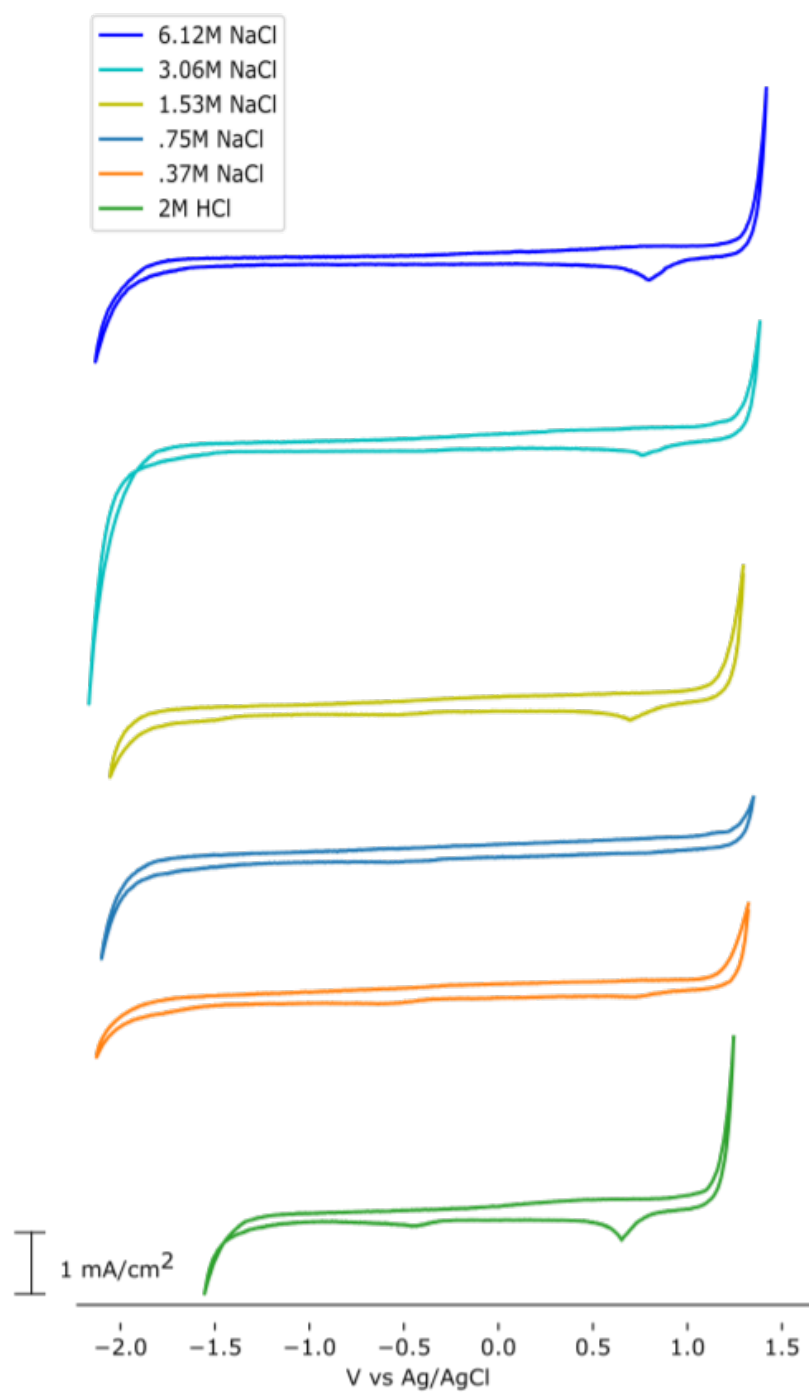
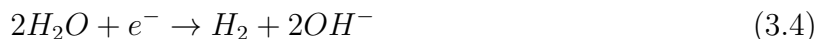


Figure 14: Shows the stability window expansion on a glassy carbon electrode between the HER and Cl₂ formation across different concentrations of NaCl compared to the same reactions in 2M HCl.

We hypothesize that the potential window expansion in this study is mainly due to changes in the local pH of the electrode rather than the competition of the electrodes surface. We expect the pH in 2M HCl to be near zero, whereas in saturated LiCl or NaCl solutions we expect the solution pH to be between 4 and 5 (slightly acidic due to equilibria with atmospheric CO₂). Based on these assumptions, by the Nernst equation, we expect to see a theoretical potential range expansion of 295 mV, compared to the average potential range expansion of 616 mV expansion we see in Figures 11-14. The calculation for the theoretical potential range expansion is derived from the following equations:

The equilibrium reduction potential for the HER,



can be thermodynamically evaluated by the Nernst equation as,

$$E = E^o + \frac{nF}{RT} \ln\left(\frac{[H^+]^2}{P_{H_2}}\right) \quad (3.5)$$

assuming the HER has an E^o of 0V vs. NHE and at 25°C and constant H₂ partial pressure reduces to,

$$E = E^o - \frac{0.059}{2} \times 2pH = -0.059 \cdot pH \quad (3.6)$$

evaluating a change of 5 units in pH allows for a theoretical voltage range expansion of 295mV.

These theoretical calculations suggest the bulk of the stability window increase could be due to a change in local pH around the electrode. Further backing this hypothesis, we believe the spike in current at far positive potentials is due to Cl₂ formation rather than oxygen evolution. This is because the 10M LiCl solution is heavily saturated with Cl⁻ ions that are readily available to react with the electrode surface. The potential where we expect to see Cl₂ formation should not depend on a pH change, but the oxygen evolution reaction should. This is consistent in Figures 11-14 where the potential at the scaled current density for Cl₂ formation is observed. These potentials remain relatively constant despite large changes in pH. Thus, we conclude that the bulk of the stability window expansion is due to a change in local pH driving the equilibrium for the HER more negative rather than a competition for the electrode active sites.

3.4.2 Enhancement of $\text{Cr}^{3+/2+}$ Redox Chemistry

Figure 15 shows the cyclic voltammograms for 0.1M Cr^{3+} in 10.42M LiCl dissolved in water across glassy carbon, platinum, and gold electrodes and for .1M Cr^{3+} in 6.12M NaCl dissolved in water on a gold electrode. In Figure 15 (a) we observe that on a gold electrode in saturated LiCl solutions there is evidence for the $\text{Cr}^{3+/2+}$ redox reaction at $\sim .45\text{V}$ vs. Ag/AgCl. One way to quickly analyze the reversibility of an electrochemical reaction is to examine the peak to peak separation. The fastest achievable peak to peak separation for a reversible reaction is 57 mV by the Nernst equation [67]. On the gold electrode, a peak to peak separation of 120 mV is shown at 100 mV/sec scan rate. This suggests a reasonably reversible chemistry, a true surprise compared to the work I illustrated in the background portion of this chapter.

In Figure 15 (b) we show the cyclic voltammogram results for a 0.1M Cr^{3+} in 10.42M LiCl dissolved in water solution on a glassy carbon electrode. Here we observe more evidence for the $\text{Cr}^{3+/2+}$ redox reaction, however, based on the peak to peak separation of $\sim 700\text{mV}$ this reaction is much less reversible on carbon compared to gold. Carbon is the most desirable of the 3 electrodes for RFB application from a cost perspective.[139, 140, 141] However, it is worth noting that this reaction was done on a pristine glassy carbon electrode. Methods exist that enhance the kinetics of a carbon electrode surface like pretreating the electrode so that it is in an oxidized state before use in an electrochemical cell [106].

In Figure 15 (c) we show the cyclic voltammogram results for .1M Cr^{3+} in 10.42M LiCl dissolved in water on a platinum electrode. Here we observe no obvious evidence of a reversible $\text{Cr}^{3+/2+}$ reaction. Lack of the reversible chemistry on a platinum electrode is not surprising because platinum electrodes are notorious for catalyzing large amounts of HER reactions. In this case, it can be assumed that the $\text{Cr}^{3+/2+}$ redox couple is suppressed by HER as in the background figures of this chapter. This is not the worst of results because from a cost perspective, platinum is too expensive to be used in a viable RFB [139, 140, 141].

In (d) we show the cyclic voltammogram results for 6.12M NaCl and .1M Cr^{3+} dissolved in water. The saturated NaCl solutions shows no evidence of the $\text{Cr}^{3+/2+}$ reaction on a gold electrode despite having displayed a similar stability window to that of LiCl from the previous

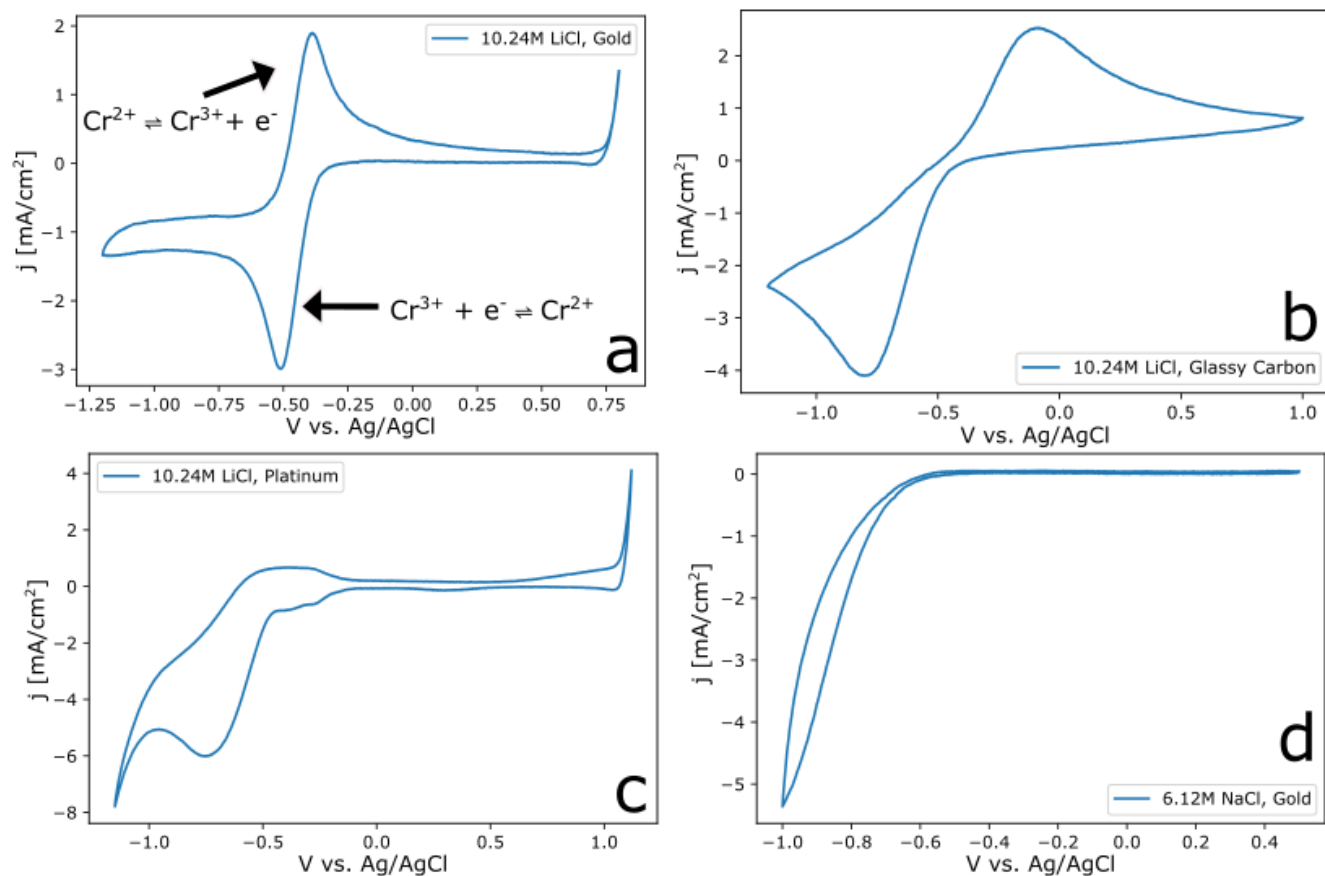


Figure 15: Shows the cyclic voltammograms for .1M Cr^{3+} in saturated salt solution on glassy carbon, gold, and platinum electrodes. In (a), (b), and (c) the Cr^{3+2+} redox reaction in saturated LiCl is observed on gold, glassy carbon, and platinum respectively. In (d) the same redox reaction is not observed in saturated NaCl on glassy carbon.

Figure 12. Note that the maximum saturation achievable for NaCl at room temperature is less than that of LiCl[142]. One possible reason the $\text{Cr}^{3+/2+}$ redox reaction does not show up in saturated NaCl solutions is that Cr^{3+} may speciate differently in Na^+ solutions than it does in Li^+ solutions. If this is true, the complex Cr^{3+} forms in saturated LiCl solutions may be better at redox chemistry than the complex Cr^{3+} forms in NaCl or lower saturated LiCl solutions.

In Figure 16 we show the cyclic voltammogram results for .1M Cr^{3+} , .1M Fe^{2+} , and 10.42M LiCl dissolved in water on both Gold and glassy carbon electrodes. In Figure 16 (a) we see that on a gold electrode, there is evidence for both the $\text{Cr}^{3+/2+}$ redox reaction and the $\text{Fe}^{3+/2+}$ redox reaction. Both of the reactions also seem to behave reversibly, based on a visual inspection of peak to peak separation. If a gold electrode was an economically viable option for a RFB, this electrolyte would serve good purpose. One intriguing feature in this voltammogram is that despite the concentrations of Fe and Cr being the exact same, we see different magnitudes in the peak current for each of the respective reactions. One reason for this phenomena is that the Cr^{3+} does not diffuse as well as Fe^{2+} does in a solution this saturated. This theory is only backed by my own lab observations that adding dissolved Cr^{3+} into a saturated LiCl solution required more physical mixing from me than when I dropped dissolved Fe^{2+} into the same saturated solution.

In Figure 16 (b) we show the cyclic voltammogram results for the same electrolyte as in (a) this time on a glassy carbon electrode. In Figure 16 (b) as hypothesized, we have evidence for both the $\text{Fe}^{3+/2+}$ and $\text{Cr}^{3+/2+}$ reactions. However, the kinetics of the $\text{Cr}^{3+/2+}$ reaction remain sluggish on the carbon electrode. The key take away from the experiments in Figure 16 is that there is no evidence that the presence of Fe in the saturated LiCl solution enhances or hinders the $\text{Cr}^{3+/2+}$ redox reaction. As discussed earlier, if the kinetics of the $\text{Cr}^{3+/2+}$ can be further enhanced on the carbon electrode, this could provide a low cost and simple solution to some of the main problems behind Fe/Cr RFBs.

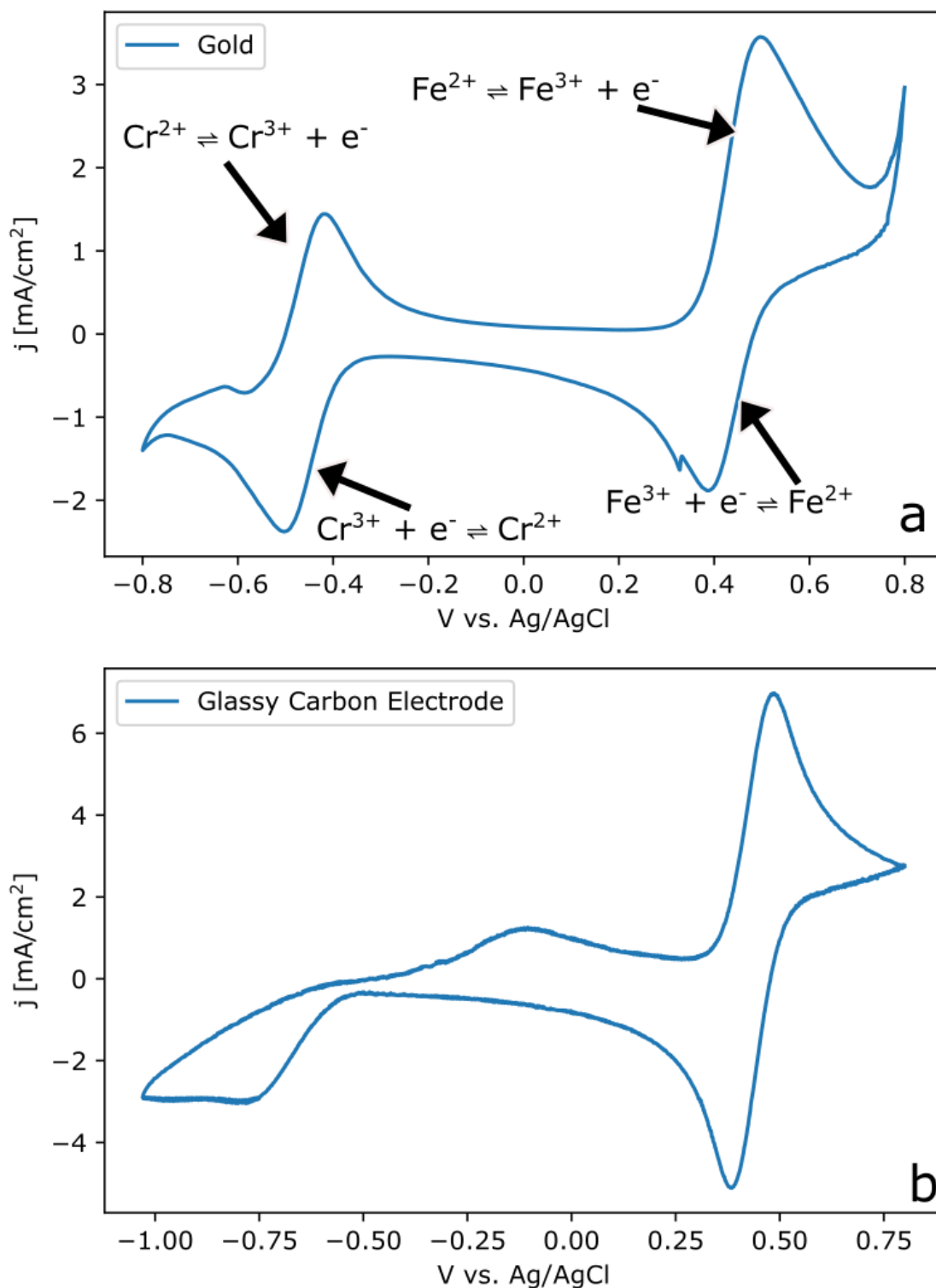


Figure 16: Shows the cyclic voltammograms for the $\text{Cr}^{3+}/\text{Cr}^{2+}$ and $\text{Fe}^{3+}/\text{Fe}^{2+}$ redox reactions using .1M Cr^{3+} and .1M Fe^{2+} in saturated LiCl solutions. In (a) the redox reactions are displayed on gold. In (b) the redox reactions are displayed on glassy carbon.

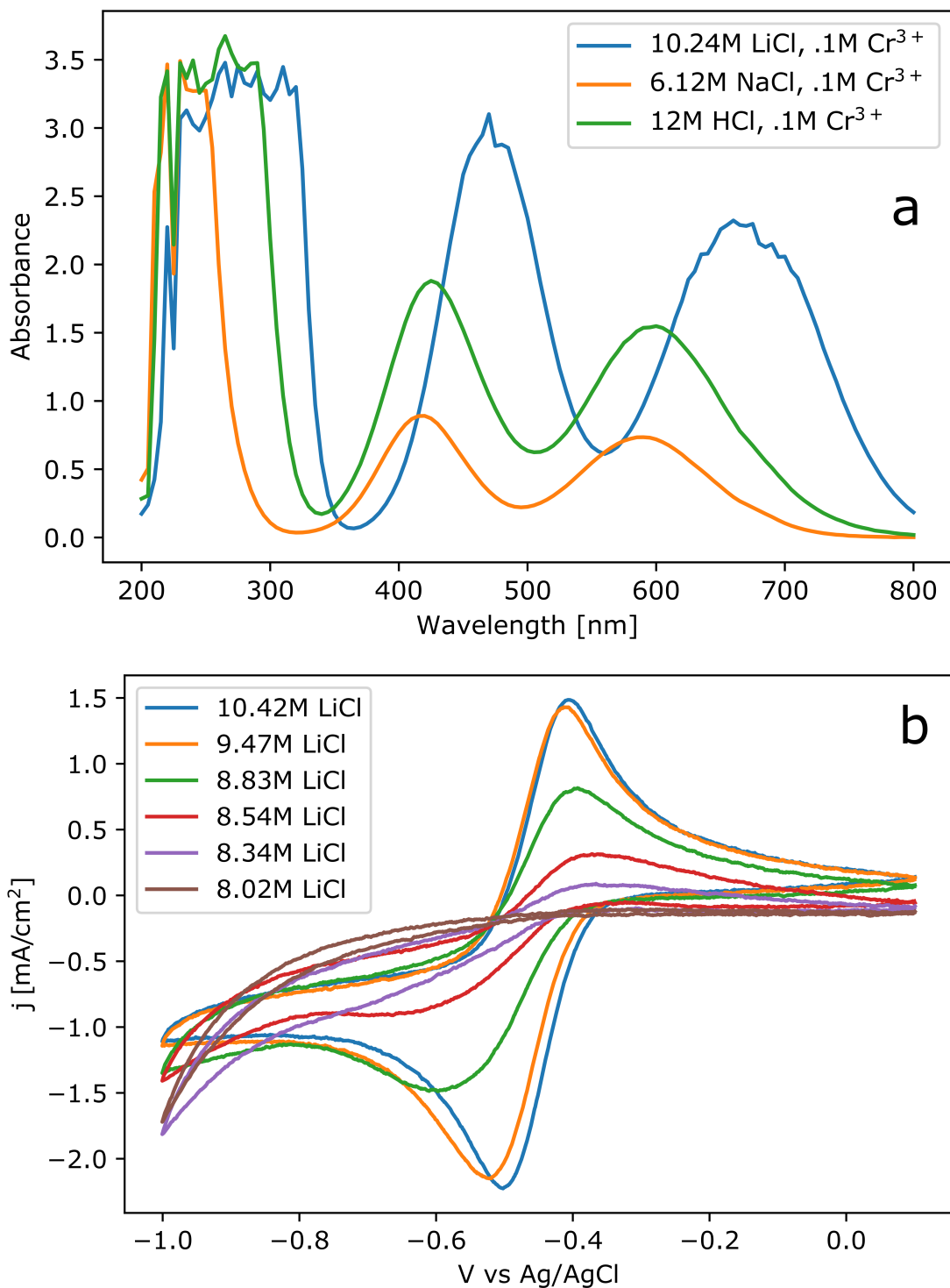


Figure 17: Shows the speciation of Cr^{3+} in different environments. In (a) we observe a UV-Vis spectra showing how Cr^{3+} speciates in saturated LiCl, saturated NaCl, and highly concentrated HCl. In (b) we show the electrochemical effect the LiCl saturation has on the reversibility of the $\text{Cr}^{3+}/\text{Cr}^{2+}$ redox reaction.

3.4.3 Cr^{3+} Speciation in Different Environments

Figure 17 (a) shows the UV-Vis spectra for .1M Cr^{3+} dissolved in 10.42M LiCl, 6.12M NaCl, and 12M HCl. The spectra shows peaks characteristic of Cr at ~ 400 and 600nm in 6.12M NaCl and 12M HCl but peaks of ~ 450 and 650nm in 10.42M LiCl. This data suggests that we have different speciations of Cr^{3+} in LiCl compared to NaCl and HCl, as backed by the mathematical model from Van Hecke et al[134]. Interestingly, despite equal Cr^{3+} concentrations added to each solution, we observe different absorbance maxima in each sample. There is no clear explanation for this as absorbance should be a function of concentration by Beer's Law[143]. One possibility could be that the Cr^{3+} species forming in these varying environments have different molar absorptivities. Another possibility for the difference in absorbance for a .1M Cr^{3+} sample in different environments could be due to the slow diffusion in heavily saturated solutions. If the Cr^{3+} was not evenly diffused in the larger volume sample, injecting a 1 mL aliquot into a cuvette from the larger sample could result in unknown concentration. It is difficult to tell when the sample is fully diffused due to the dark green color of Cr^{3+} even in low concentrations.

Additionally, it is worth noting the pH values across these different solutions because pH can have an effect on the optical properties we expect to see in UV-Vis spectra[144]. Water saturated to the maximum limit at room temperature (10.42M) with LiCl gives a pH of 4.24. This result is surprising because we expected that adding a high concentration of base to a solution should result in a higher pH reading. In a similar water solution fully saturated with NaCl (6.12M), the pH was 8.13M. Interestingly, by adding .1M CrCl_3 to both the saturated LiCl and NaCl solutions, the pH dropped to 1.85 and 3.03 respectively. This effect is consistent with previous claims that when waters coordinate with Cr that they can become more acidic [134].

In Figure 17 (b) the CV results for 0.1M Cr^{3+} in LiCl solutions varying from 10M to 8M. In the voltammograms at high concentrations we see reversible $\text{Cr}^{3+/2+}$ redox chemistry. However, as we dilute the LiCl, we see steady decrease in the reversibility of the Cr^{3+} redox kinetics and around 8M we see complete loss of the obvious $\text{Cr}^{3+/2+}$ redox peak. This suggests that the reversibility of the $\text{Cr}^{3+/2+}$ redox reaction is dependent on the surrounding

concentration of LiCl and may also explain why the saturated NaCl solution in Figure 12 did not show any evidence of the $\text{Cr}^{3+}/2+$ redox reaction because NaCl cannot reach 8M in water at room temperature [142]. Note that in future figures there is evidence for Cr^{3+} redox chemistry in lower concentrations of LiCl, those results are likely due to better polished electrodes than what I had used to run these experiments, as these experiments were done before I had a lot of the experience I now have as an electrochemist.

3.4.4 Nicholson Fittings for k_o Values

Figure 18 shows the iR compensated cyclic voltammograms for .1M Cr^{3+} in ranges of LiCl concentrations from 10M-5M. Each voltammogram in the respective figures was run at a different scan rate. In Figure 18 (a) we show the data for 10M LiCl. The current densities in this experiment decrease consistently with decreasing scanrate, as expected for a voltammetry measurement with a soluble redox couple. In Figure 18 (a) scan rates varied from 20 mV/sec to 1280 mV/sec yielding peak to peak separations from 71 mV to 177 mV. One interesting feature in (a) is that the reduction peaks shift as a function of scan rate more than the oxidation peaks. One theory for this could be that the reaction mechanism for oxidation in the system is different than the reaction mechanism for reduction. Even further, it could be hypothesized that the saturated LiCl solution is helping to catalyze one mechanism more than the other.

In Figure 18 (b), (c), and (d) we see similar data sets for .1M Cr^{3+} in 9M, 7M, and 5M LiCl. Scan rates for these experiments vary from 5 mV/sec to 160 mV/sec, 5 mV/sec to 80 mV/sec, and 5 mV/sec to 80 mV/sec respectively. Peak to peak separations ranged from 72 mV to 155 mV, 120 mV to 138 mV, and 134mV to 158 mV for 9M, 7M, and 5M LiCl solutions respectively. Notice here that the peaks do not scale nearly as consistently at lower LiCl concentrations compared to the fully saturated LiCl solution. Peak to peak separations within the limits of the Nicholson fitting method (see table 1) were reached at much lower scan rates in the less saturated solution, suggesting more sluggish kinetics. Lower concentrations of LiCl were also studied to extract kinetic rate constants. However, at lower concentrations we saw a similar result as in the previous Figure 17, that as we decrease

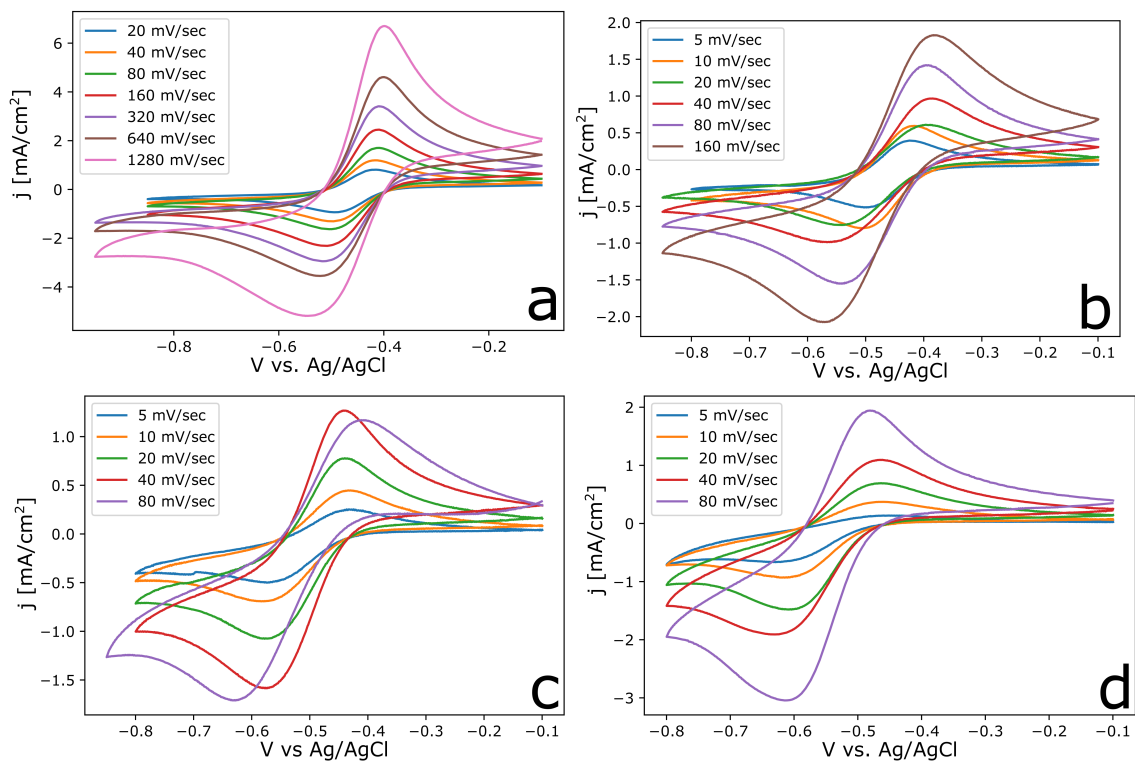


Figure 18: Shows the iR compensated cyclic voltammograms for different concentrations of LiCl at different scan rates on a Gold electrode. In (a) 10M LiCl, (b) 9M LiCl, (c) 7M LiCl, and (d) 5M LiCl.

concentration eventually, there is no evidence of the $\text{Cr}^{3+/2+}$ redox reaction. As previously noted, lower concentrations for visible evidence were studied here than in Figure 17. Further work should be completed to study the true threshold concentration for when the $\text{Cr}^{3+/2+}$ redox reaction appears in electrochemical measurements.

In Figure 19 we show the Nicholson equation variable Ψ as a function of the inverse square root of the scan rate. Based on the equations in the experimental section of this chapter, Ψ vs. the inverse square root of scan rate should scale linearly and have a y-intercept close to 0. If this holds true, knowing all of the other variables in the Nicholson equation, a k° value can be calculated. The fully saturated LiCl experiments show the best representation of this although it is not exact. The fits get worse as the LiCl saturation becomes more dilute. This is expected based on the preliminary CV data in Figure 18 that showed current did not scale evenly as a function of scan rate. From this data, we can conclude that the Nicholson kinetic extraction method may not be best suited for these experiments. Nicholson kinetic fittings work best for straight-forward single electron transfer mechanisms[67]. As previously stated, it is a hypothesis that this reaction mechanism involves multiple steps. If that hypothesis is valid, it could explain why the Nicholson fitting method is not yielding the predicted results. Further work should be completed on this topic to extract a true rate constant for the $\text{Cr}^{3+/2+}$ redox reaction and how that rate constant changes as function of the LiCl concentration.

3.5 Conclusions

Through the exploratory research described in this chapter, we have taken advantage of a simple way to expand the stability window of platinum, gold, and glassy carbon electrodes by using aqueous solutions containing high LiCl concentrations. Through this potential range expansion with the use of LiCl, we further studied that the $\text{Cr}^{3+/2+}$ redox reaction displays fast kinetics on a gold electrode and slower kinetics on a glassy carbon. When trying to extract specific values of the heterogeneous electron transfer rate constant (k°) through Nicholson kinetic fittings, it was concluded that this method is not the best way to extract

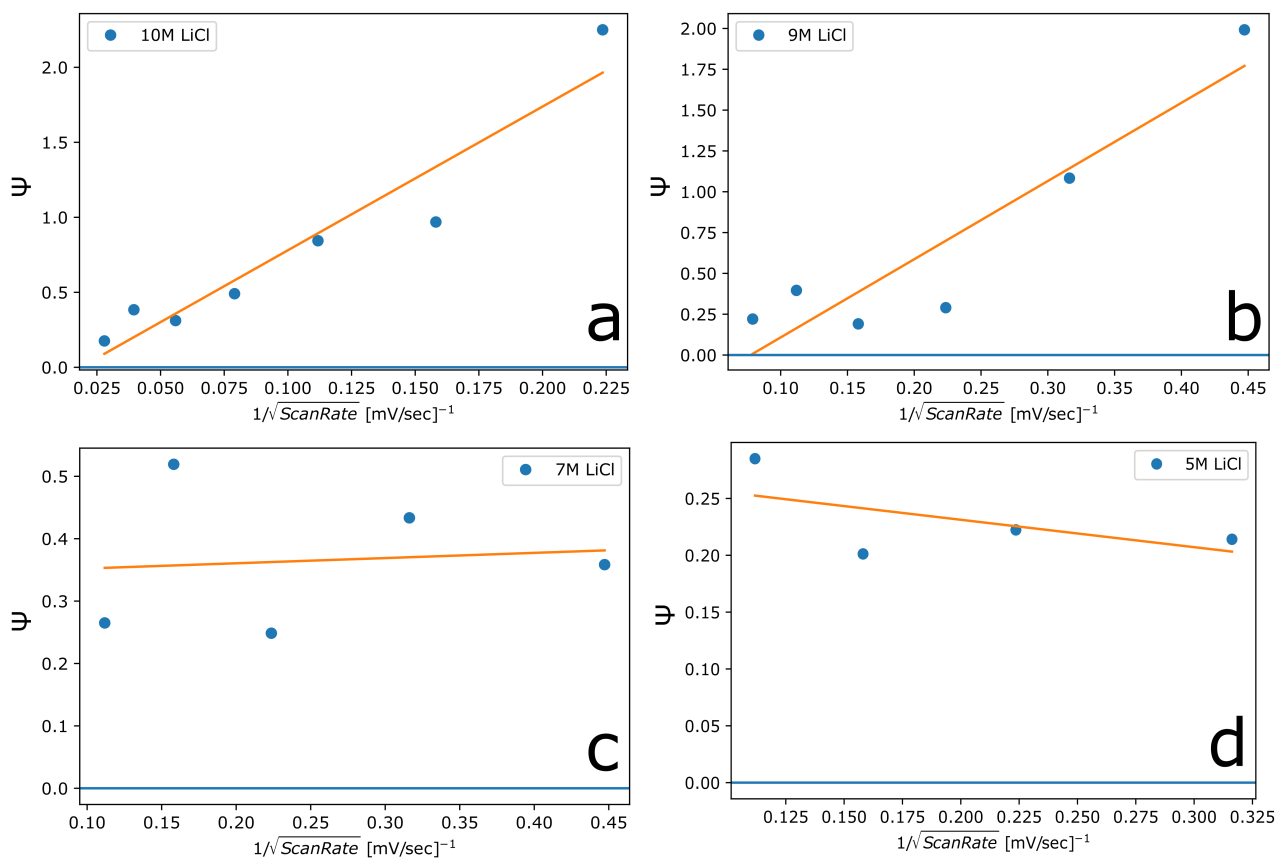


Figure 19: Shows the Ψ vs inverse square root of the scan rates for different saturations of LiCl. In (a) 10M LiCl, (b) 9M LiCl, (c) 7M LiCl, and (d) 5M LiCl.

accurate kinetic values for this reaction due to the high solution resistance of a solution this saturated. We also began studying the speciation of Cr^{3+} in different environments. By examining the optical properties of Cr^{3+} in saturated NaCl, LiCl, and HCl solutions, we uncovered that Cr^{3+} forms complexes with different optical properties in these environments. We believe that some of these different Cr^{3+} species are better at undergoing redox reactions than others.

More work certainly needs to be done to complete this study. First, we need to be able to extract k^o values from the $\text{Cr}^{3+/2+}$ redox reaction on different electrodes. There are multiple ways this that include, rotating-disk electrode experiments, impedance spectroscopy, or the use of the shrinking overpotential method that is outlined in Chapter 2 of this dissertation. Next, the hypothesis that some Cr^{3+} chloride complexes are better at redox chemistry than others needs to be probed further. UV-Vis data for different concentrations of Cr^{3+} in LiCl needs to be gathered. The same needs to be done altering the Cr^{3+} concentration holding the LiCl concentration constant. From this, we can perhaps work with computational researchers to generate predominance plots that express which Cr^{3+} species predominate as a function of LiCl and Cr chlorides. Combining the foundational work I completed on this topic with this future work, our hope is that we can contribute to the advancement of aqueous based RFBs.

4.0 Additive Manufacturing

4.1 Introduction

Additive manufacturing can be defined as the process which combines layers of materials together to make objects created using 3D computer-aided design (CAD) modelling software; it also commonly known as 3D printing. Additive manufacturing was created over 20 years ago, but only recently with modern advances have we seen it progress into a viable method for prototyping new products[146, 147]. Additive manufacturing has found a niche in many industries including ceramics, polymers, metals, composites, biological systems, and concrete[146, 147, 148]. The predecessor to additive manufacturing, creatively called subtractive manufacturing, uses machines like a CNC mill to cut away from a bulk block of material[146, 147, 148].

The recent advances in additive manufacturing that have optimized the accuracy and turnaround time to get a finished product, allow for additive manufacturing to make a large impact on the manufacturing and prototyping industries[146, 149, 150, 151, 152, 153]. One of the most popular forms of additive manufacturing uses a 3D printer to heat materials to a molten state before layering them on top of each other in the specific orientation designed by the user's CAD file[150, 151, 152, 153]. One key benefit in being able to deposit the exact amount of material needed is that it minimizes the waste associated with the manufacturing process[146, 149, 150, 151, 152, 153]. A schematic of this type of 3D printing is demonstrated in Figure 20[148]. In comparison, subtractive manufacturing starts with more material than is actually needed for the process, then cuts out the design using an automated drill system, and leaves behind waste that often cannot be reused[149, 146].

From a design perspective, additive manufacturing has many advantages. Specifically, it enables the construction of parts that require additional empty space within the volume of the design as well as parts that tightly integrate multiple materials[149, 146]. For example, imagine being tasked to design a prototype for a food storage container. Using subtractive manufacturing, the process would begin by drilling a block of plastic until the volume of the

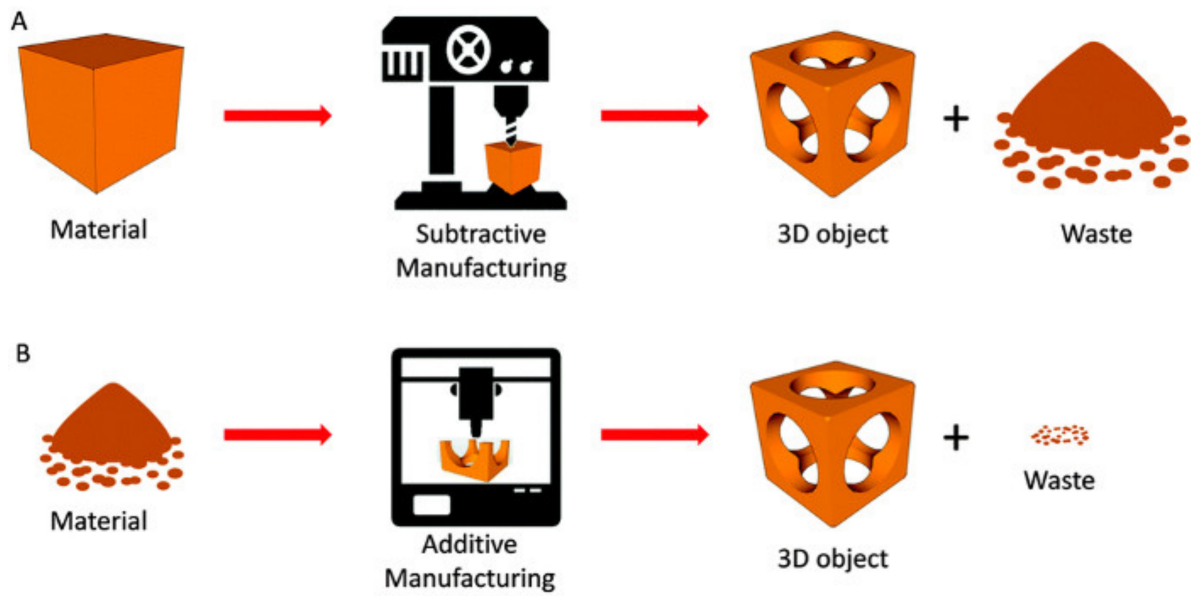


Figure 20: Adapted from Chen et al. Shows the life cycle of a material in subtractive manufacturing (a) and in additive manufacturing (b)[145].

container was cut out. The bulk of the starting material will be turned into plastic shavings that might be challenging to recover and reuse. However, additive manufacturing allows for production of that same container using much less materials and, therefore, for much less of a cost. Now I am sure better ways exist to design and manufacture food containers, but for a specific part that requires a finite amount of empty volume, additive manufacturing has a clear advantage.

To manufacturing parts made of multiple materials, 3D printers can be equipped with multiple extruders that deposit distinct materials[151, 150]. In subtractive manufacturing if the desired product requires a multi-material part, it will have to be manufactured as individual pieces and then later combined in the manufacturing process, adding total cost of the part. Because of these advantages additive manufacturing is now used for aerospace parts, motor vehicle production, medical/dental parts, military machinery, architectural material (including fully 3D printed houses!), and food[146, 149, 150, 151, 152, 153].

Now that there is a general understanding for the importance of additive manufacturing, I should explain it's relevance to my work here at Pitt. When I first joined the McKone Lab, I was responsible for initiating 3D print prototyping so that we could develop our own test devices for different electrochemical cells. As I progressed into my role as a technician for our 3D printer, I learned many valuable skills like CAD Design, hands on troubleshooting, and other fundamentals to obtain the highest quality printed part. As an MS student who aspires to go into industry, I think this learning process helped shape some of the important skills I will take with me well beyond my time at the University of Pittsburgh.

4.2 Results and Discussion

The start-up process for 3D prototyping involved a significant amount of struggle. In the following figure you will see that not every print turns out perfect. However, even if the printing process was frustrating at times, I found a great deal of satisfaction in being able to take an idea or design and being able to hold it in your hand after a few hours of work. In fact, in Figure 21 (a) on the left I show one of the first prints I completed. The

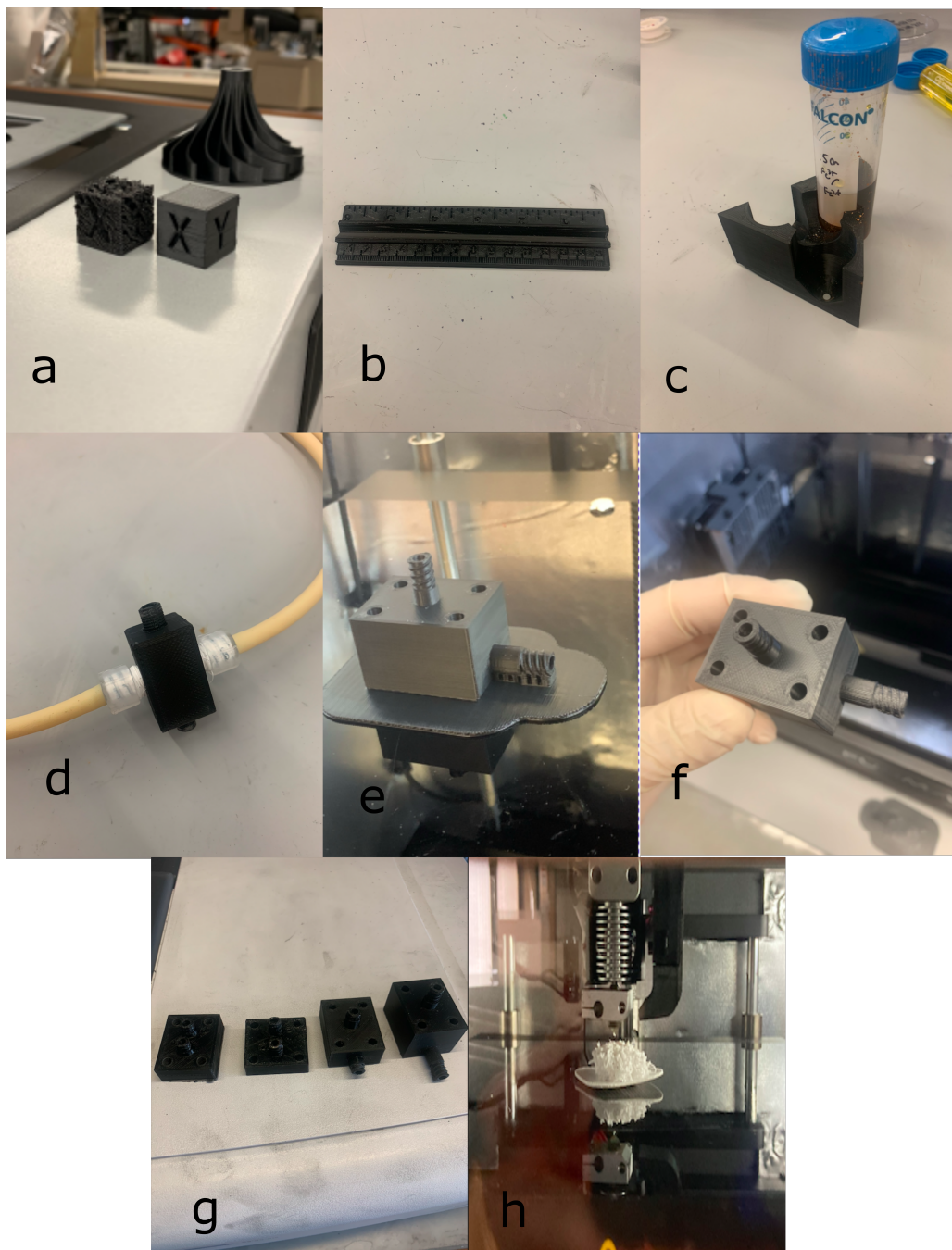


Figure 21: Shows some of the 3D prints I was responsible for or assisted on. In (a) my first ever print of a 3D calibration cube shows a before and after. In (b) a solid attempt at a ruler. In (c) a falcon tube holder. In (d) a spectroelectrochemical cell prototype. In (e), (f), and (g) membrane reactor prototypes. In (h) an example of warping and the affect it can have on the rest of the print.

print was done using ABS material, which is known to be easy to 3D print. As you can see, the initial print attempt resulted in poor quality, but after indulging in a lot of 3D print Youtube videos, I was able to obtain a higher quality result pictured directly to the right. After learning some of the basic fundamentals of 3D printing like bed-levelling, optimal print temperatures, making sure to dry water out of printing filaments before printing, etc. I decided to design and print a few other tools like Figure 21 (b) and (c) which show a ruler and a falcon tube holder respectively. Two random items, but at the time they were relatively scarce around the lab. During COVID when I was trying to get adjusted to the lab space and often times found myself working alone, it was difficult to yell across the benchtop to whomever used it last and say, “Hey where did you hide the ruler?”. These prints were not perfect as shown in Figure 21 (b) where it is hard to make out the numbers on the ruler, but I was proud that the tick marks were the right distance apart.

After a few months of printing fun tools for the lab it became time to take my print skills to the next level. I had been tasked with assisting one of the undergraduate lab members with printing a spectroelectrochemical cell prototype. Spectroelectrochemical cells are used to examine optical properties of electrolytes as they are oxidized or reduced in a system. This specific cell shown in Figure 21 (d) was designed so that optical properties of the electrolyte could be examined as it flowed through the cell. The cell is connected to a peristaltic pump on both sides and the other female thread connectors would attach to the UV-Vis to gather optical data. The work we completed on designing and printing this cell did not ultimately lead to a useable prototype, but it was a valuable learning experience to begin creating prototypes for electrochemical systems. Additionally, it was my first experience creating a print that had to be attached with threads, which are notoriously difficult to 3D print. I considered it a success nonetheless.

The next experimental prototyping I participated in was for a membrane reactor project. For this project we had to use a chemically resistant polysulfone material, PSU. This material is considered to be intermediate level to print because the chamber of the printer needs to be held at a constant temperature throughout the print. The build plate also has to be heated to a certain temperature so that the PSU will adhere properly. The results for different membrane reactor prototypes can be seen in Figure 21 (e), (f), and (g). The main challenge

with manufacturing these reactors was getting the material not to warp when it was printing. When warping happens, the base of the print curves out in a parabolic shape as in Figure 19 (h), making the next layer of print slightly more parabolic until the extruder begins to drag through the previously printed layers. This usually results in a failed print attempt. The solution to this is to take all the precautionary steps to make sure the first layer of the build properly adheres to the build plate. These steps include applying a printer adhesive onto the build plate in the right amount, making sure the bed is level and the extruder is set to print at the proper distance from the build plate, making sure the print is set to be complete at hot enough temperatures so that the material does not get jammed in the extruder, and using a drying oven to properly remove all water that may have been absorbed from the air into the filament.

4.3 Conclusion and Future Work

Lastly, to be classified as an expert level printer by Vision Miner, one must be able to print a material from either PEEK or PEKK. In Figure 22 I have designed a bottle opener to take with me from the lab to prove my expertise as a 3D printing technician. I have not yet attempted to print this design but hope to before my time at Pitt is over.

In conclusion, I was able to learn valuable skills like CAD design and hands on experience with additive manufacturing through my time in the McKone Lab. This section was written intentionally in a more casual tone as it was not the main focus of my degree, but rather a fun and entertaining way to gain skills I can take with me beyond my time at Pitt.



Figure 22: Shows a bottle opener designed to be printed in PEEK or PEKK

5.0 Conclusion and Closing Remarks

Over the past 2 years I have gained valuable experience in the transition to becoming a chemical engineer. Broadly, I learned important skills including problem solving, experimental design, data analysis, technical writing, and the experience and patience to understand that research almost never goes as planned. I will take the skill set I have developed at Pitt with me through the rest of my life.

More specifically, my efforts were directed to making an impact on sustainable energy storage through RFBs. To enhance the process of materials discovery for RFBs, we successfully assembled an apparatus that can extract kinetic rate constants for different electrolytes, while closely mimicking the environment these electrolytes would endure in a real RFB setting. We hope that this method will standardize the way kinetic rate constant values are extracted for flow batteries and eliminate large literature discrepancies. Additionally, I explored a simple method for obtaining reversible $\text{Cr}^{3+/2+}$ redox chemistry by using an aqueous solution saturated with LiCl. Through this work, I have demonstrated a new way to obtain $\text{Cr}^{3+/2+}$ redox chemistry across various electrodes. This work is still unfinished, but I have hope that it will contribute to the shift of cost effective aqueous RFBs as a viable alternative for grid scale energy storage.

Overall, the work we have done has demonstrated the importance of both developing characterization tools for RFB materials discovery and contributing to the transition of aqueous batteries as a cheaper and safe alternative to grid scale energy storage. This work further motivates the need for an efficient, standardized, and smaller scale flow battery apparatus for materials testing. I believe it also motivates researchers to continue being creative in materials discovery to find the best electrolyte that will make RFBs commercially cost competitive.

Finally, I hope this dissertation serves as a valuable resource for future researchers who continue the work on RFB materials discovery. I have no doubt we are on the verge more sustainable energy processes and I look forward to reading about the advancements in the field in the decades to come.

Appendix A A. Detailed Experimental Procedure from Chapter 2

The experimental apparatus (Figure S1) was constructed using a commercial RFB stack (TDM LLC, fuelcellstore.com). The RFB stack included polymeric endplates, two copper coated current collectors, two graphite plates with interdigitated flow fields, two PTFE gaskets, two carbon felt squares 10 cm² in area, and a Nafion cation-exchange membrane. A single set of battery hardware was used for all experiments without modifications except for routine cleaning and abrasive polishing of the current collectors.

To construct the RFB stack, an endplate was placed flat on a bench with the electrolyte inlets oriented at the top and the binding screws were inserted through the guide holes. Wooden toothpicks were used as guides to ensure the holes of the gaskets, membrane, and flow plates were properly aligned. The current collector was inserted into its socket on the inside of the endplate. Next, one of the graphite flow field plates was positioned so that electrolyte flow can enter the top left of the cell. A PTFE gasket was then placed on top of the graphite plate. Next, a piece of carbon felt was laid inside the square gasket and on top of the interdigitated flow field. The Nafion membrane was placed next on the carbon felt such that the edges overlapped with the PTFE gasket. Next, a second electrode, gasket, and graphite flow field were placed in reverse order, and the flow field was oriented so that electrolyte flow can enter in the top right of the stack and exit on the bottom left. Lastly, the second current collector and endplate were inserted and aligned with the binding screws. While the stack is held together by hand, washers and nuts were used to tighten the cell to finger tightness. The screws were then further tightened with a wrench in an alternating pattern to the maximum extent possible that did not result in any visible bowing of the endplates.

Next, the RFB stack was integrated into an electrolyte flow loop. The full apparatus consisted of the RFB stack, a peristaltic pump (MasterFlex), a three electrode half-cell (machined in house from PEEK), and two 10 mL reservoirs with compression fittings (Saville) on each side. All components were connected using rubber peristaltic pump tubing (MasterFlex ChemDurance Bio) or clear polyethylene tubing (McMaster-Carr). Nylon Barb

connectors (McMaster-Carr) were used to connect the rubber tubing to the clear plastic tubing and Nylon Luer adapters (McMaster-Carr) were used to connect peristaltic tubing into the three-electrode half-cell. Lastly, Nylon screw in Luer adapters (McMaster Carr) were inserted into the RFB stack to allow for connection of the clear plastic tubing.

The full apparatus was assembled by using a ring stand to hold the reservoirs in a vertical orientation, such that RFB electrolyte could enter the top and flow out the bottom. The reservoirs were further configured so that the inlet flow created a dripping action, which has the added benefit of preventing bubbles from accumulating in the flow lines. Clear plastic tubing ran from the first reservoir into the top left of RFB stack. The tubing was connected using the screw-in Luer adapters. Clear plastic tubing was also inserted into the opposite side of the RFB stack using a screw-in Luer adapter. Then the clear plastic tubing was further connected to peristaltic tubing using a barb connector. The barb connector was sealed with PTFE tape to prevent any leaks. Next, the peristaltic tubing was clamped into the rollers of the pump and further connected back into the clear plastic tubing using a barb connector lined with PTFE tape. Finally, the clear plastic tubing was run back into the starting reservoir.

The procedure above comprised assembly of the non-capacity limiting RFB half-cell. This was repeated for capacity-limiting half cell, except that the clear plastic tubing was also connected through the three-electrode analytical cell as schematized in Figure 2 of the main text using Luer and compression fittings. The half-cell was held in place using an additional arm connected to the same ring stand as with the reservoirs.

Next, electrodes were inserted into the analytical cell, which contains threaded holes for one working UME (Pt or C fiber, BASi), one counter-electrode (Alfa Aesar), and one reference electrode (Ag/AgCl, CH Instruments). Screws for each size of the respective electrodes were also machined in house. The screws were placed over each respective electrode and an O-ring was attached at the bottom of each electrode to prevent leaks. The electrodes were then screwed into their respective locations in the half-cell just until leak tight.

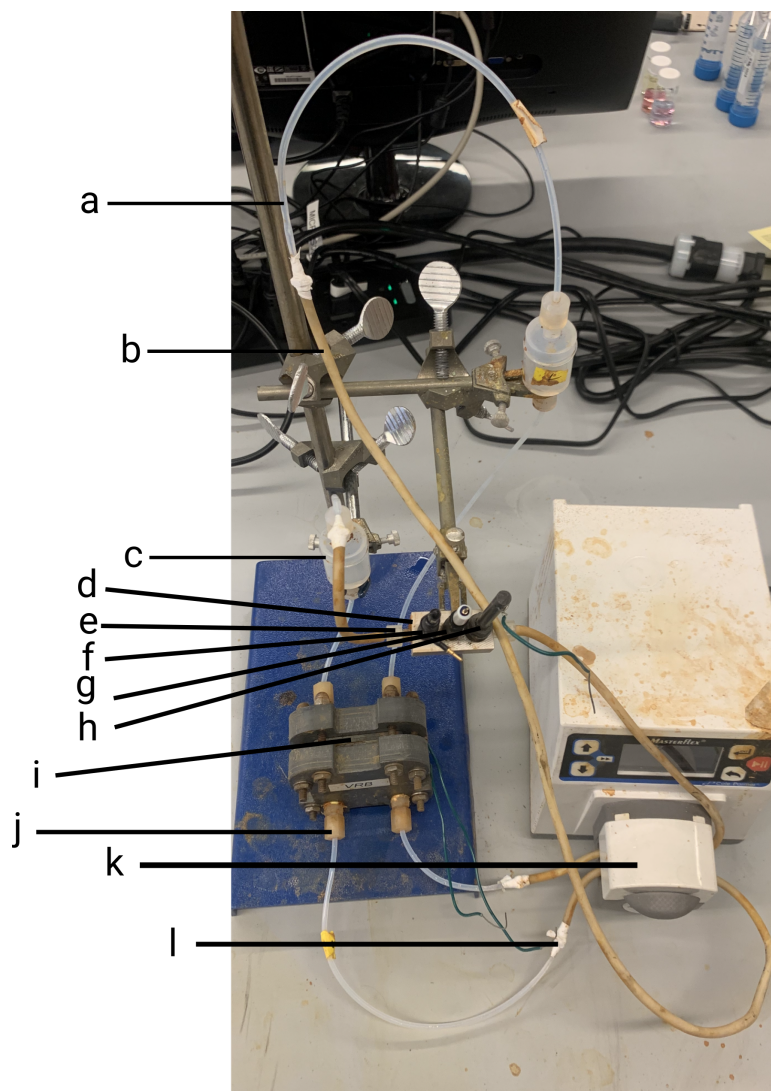


Figure 23: Photograph of the experimental apparatus with labels for key components described in the Materials and Methods section. The labels are as follows: (a) clear polyethylene tubing; (b) MasterFlex ChemDurance Bio peristaltic pump tubing; (c) Savillex reservoir; (d) PEEK three electrode cell; (e) Nylon Luer Adapter; (f) UME; (g) graphite counter electrode; (h) Ag/AgCl reference electrode; (i) Flex Stak FB cell; (j) Nylon Screw in Luer Adapter; (k) Masterflex peristaltic pump; and (l) Nylon barb connector.

The next step was to make electrolyte for the cell. In a representative procedure, the non-capacity limiting electrolyte was made using a 50mL polypropylene centrifugation tube (Corning) to weigh 4.97g $\text{FeCl}_2 \cdot 4\text{H}_2\text{O}$ and 6.76g $\text{FeCl}_3 \cdot 6\text{H}_2\text{O}$ (Alfa Aesar). These salts were then solvated to 50 mL using a 2M HCl (aq). The 2M HCl solution was made diluting from a 12M HCl stock solution (Fisher Chemicals).

The tubes were sonicated and stirred as needed until the salts fully dissolved. The final concentration of the analyte was 0.5M Fe^{3+} and 0.5M Fe^{2+} . The capacity-limiting electrolyte was made in the same way using 9.94g $\text{FeCl}_2 \cdot 4\text{H}_2\text{O}$ and solvating to 50 mL total volume with 2 M HCl (aq). The final concentration of the catholyte was 1.0 M Fe^{2+} . Both sets of electrolytes were allowed to stand without stirring for at least 10 minutes prior to their use in experiments.

Next, the apparatus was cleaned of residues from prior experiments. To clean the apparatus, the plastic tubing was removed from the tops of both reservoirs and inserted into a beaker that contained deionized water. The peristaltic pump was then set to flow at 10 mL/min in the opposite direction from RFB operation. Water was flowed through the apparatus until both reservoirs contained ~ 1 mL of water—note that this corresponds to 2–3 mL of water total when including the internal volumes of the RFB, analytical cell, and tubing. The pump was next paused so the plastic tubing could be reinserted into the tops of the reservoirs. The pump direction was then reversed and allowed to flow for 15 minutes before the water was drained from the apparatus and into a waste beaker.

Next, the working electrode was removed from the three electrode cell to be prepared via a series of polishing and pretreatment steps. A carbon fiber UME was polished by placing a piece of grinding paper inside a plastic Petri dish. A small quantity (approximately 0.25 mL by volume) of alumina powder with a 1-micron grit size was placed onto the grinding paper and wetted with water to generate a slurry of a similar consistency to cream or very thin acrylic paint. The electrode was held level with the bench top and polished in a circular motion via twenty rotations in both the clockwise and counterclockwise directions on the grinding paper. The electrode was then sonicated for 30 seconds to remove excess alumina powder. This process was then repeated using both 0.3- and 0.05-micron alumina powder. The entirety of this process was repeated for all UME working electrodes.

Carbon fiber UMEs were further pretreated by sonicating in pre-purified isopropanol, as reported previously. [106, 154] In a representative procedure, a suspension containing 3.3 g of activated carbon (Alfa Aesar) and 9 mL of isopropanol(Alfa Aesar) was stirred for 5 minutes and then sonicated for 10 minutes. The mixture was then left to stand in air for 30 minutes. After 25 minutes, the working electrode of interest was polished as described above. The electrode was then submersed into the carbon slurry for 10 minutes. The electrode was finally rinsed and sonicated in deionized water for 30 seconds. Carbon fiber UMEs left in this condition as pristine or non-oxidized carbon in the main text.

To prepare oxidized carbon fiber UMEs, the electrodes were further placed into a separate single-chamber electrochemical cell comprising a 20 mL scintillation vial containing 0.5M H_2SO_4 , a graphite counter electrode, and a Ag/AgCl reference electrode. The electrode was then cycled at 200 mV/sec from -0.25 to 1.5V vs. Ag/AgCl for 100 cycles and then 0.25 to 1.7V vs. Ag/AgCl for 20 cycles. Upon removal and rinsing with deionized water, electrodes were used immediately for analytical experiments.

Final assembly comprised filling the analytical apparatus with electrolyte and initiating charge-discharge and voltammetry experiments in the RFB and analytical cell, respectively. On the the capacity limiting side of the RFB, 3.5 mL of Fe^{2+} electrolyte was pumped into the apparatus at 10 mL/min. The volume was gauged by monitoring the negative volume displacement in a 15 mL polypropylene centrifugation tube. On the non-capacity limiting side of the apparatus, 12.5 mL of 0.5M $\text{Fe}^{3+/2+}$ electrolyte was pumped in at 10 mL/min while monitoring in the same fashion. Note that this total volume was the maximum that could be used while maintaining a modest headspace in the reservoirs to capture air bubbles.

Next, a potentiostat (Gamry, Reference 600) was connected to the current collectors of the RFB in a two-electrode configuration. A second potentiostat (of the same design) was connected to the analytical cell in a 3-electrode configuration. The potentiostat connected to the RFB was configured to run cyclic charge-discharge experiment using a constant current of ± 0.2 A. Half cycles were set to terminate after 2000 s had elapsed or the applied potential reached a limit of ± 0.6 V. The battery was cycled 5 times with a 1 s sample period.

The potentiostat connected to the analytical cell was configured to run cyclic voltammetry experiments continuously alongside battery charge–discharge over a potential range from 0.1 to 0.9 V vs. Ag/AgCl at 20 mV/s without iR compensation. In a representative run, 160 CVs were performed over a total of 2.7 hours, which was the total time required to charge/discharge the flow battery over 5 cycles. A total of 5 replicates were completed for each type of UME, for a total of 15 experimental runs. The data in the main text comprise representative results, which were chosen by avoiding data corresponding to the highest or lowest values of reaction rate constant, battery capacity, charge–discharge time. Complete datasets for all experimental runs have been assembled in the following section.

Appendix B B. Tabulated Literature Values displayed in Figure 3

To illustrate the need to perform high-quality analytical measurements, Table 2 presents a representative set of heterogeneous electron transfer rate constants reported in the literature for four popular RFB electrolytes at various types of carbon electrodes. These data were collected from some studies that were directed at RFB operation and others that were directed at the fundamental chemistry and physics of interfacial electron-transfer. Accordingly, only a subset of these values include accompanying measurements of RFB figures of merit, which in turn makes it challenging to contextualize differences in kinetics in terms of device-level performance. The large spread in these data clearly indicates that electron-transfer processes remain poorly understood even in well-established RFB active materials. While some of this ambiguity results from the use of different carbon materials and experimental conditions, differences in interfacial electron transfer kinetics of up to several orders of magnitude have been reported even while holding these constant.

Table 2: Compiled kinetics data for aqueous RFB redox couples at various types of carbon electrodes

redox couple	electrode material	rate constant, k^0 (cm/s)	measurement technique	supporting electrolyte	concentration of active species	Ref.
$\text{Fe}^{3+}/2+$	glassy carbon	7.3×10^{-5}	RDE	2 M H_2SO_4	1 M	Yang[90]
	glassy carbon	2.3×10^{-3}	RDE	0.2 M HClO_4	5 mM	McDermott[91]
	glassy carbon	1×10^{-3}	RDE	0.3 M HCl	1 mM	Stulikova[92]
	pyrolytic graphite	5.2×10^{-4}	RDE	4 M HCl	0.1 M	Ateya[93]
	pyrolytic graphite	1.0×10^{-3}	CV	1.5 M HCl	1 M	Hollax[94]
$\text{V}^{3+}/2+$	glassy carbon	1.0×10^{-6}	potentiostatic polarization	4.2 M H_2SO_4	1.6 M	Orijji[95]
	glassy carbon	1.4×10^{-4}	EIS	4.5 M H_2SO_4	1.5 M	Bourke[96]
	electrochemically activated graphite	1.1×10^{-6}	CV	2 M H_2SO_4	2 M	Liu[97]
	carbon felt	1.4×10^{-6}	LSV	0.1 M H_2SO_4	150 mM	Li[98]
	carbon felt	1.5×10^{-5}	CV	1 M H_2SO_4	50 mM	Agar[99]
	carbon paper	1.1×10^{-3}	CV	1 M H_2SO_4	50 mM	Wu[100]
$\text{VO}_2^+/\text{VO}^{2+}$	glassy carbon	2.2×10^{-6}	potentiostatic polarization	4.2 M H_2SO_4	1.6 M	Orijji[95]
	glassy carbon	4.5×10^{-5}	EIS	4.5 M H_2SO_4	1.5 M	Bourke[96]
	electrochemically activated graphite	8.2×10^{-4}	CV	2 M H_2SO_4	2 M	Liu[97]
	carbon nanotubes	1.8×10^{-6}	CV	1 M H_2SO_4	100 mM	Friedl[101]
	carbon paper	1.0×10^{-3}	CV	1 M H_2SO_4	50 mM	Wu[100]
	carbon-polymer composite	8.5×10^{-4}	CV	1 M H_2SO_4	50 mM	Yamamura[102]
AQDS/AQDSH ₂	glassy carbon	7.2×10^{-3}	RDE	1 M H_2SO_4	1 mM	Huskinson[103]
	glassy carbon	1.5×10^{-4}	RDE	1 M H_2SO_4	1 mM	Yang[90]
	glassy carbon	4.8×10^{-4}	CV	1 M H_2SO_4	10 mM	Lantz[104]
	glassy carbon	1.5×10^{-4}	RDE	2 M H_2SO_4	1 M	Yang[90]

Bibliography

- [1] “U.S. energy facts explained - consumption and production - U.S. Energy Information Administration (EIA).”
- [2] M. Lenzen, “Life cycle energy and greenhouse gas emissions of nuclear energy: A review,” *Energy Conversion and Management*, vol. 49, pp. 2178–2199, 8 2008.
- [3] T. Jin and J. Kim, “What is better for mitigating carbon emissions – Renewable energy or nuclear energy? A panel data analysis,” *Renewable and Sustainable Energy Reviews*, vol. 91, pp. 464–471, 8 2018.
- [4] F. L. Toth and H. H. Rogner, “Oil and nuclear power: Past, present, and future,” *Energy Economics*, vol. 28, pp. 1–25, 1 2006.
- [5] G. M. Joselin Herbert, S. Iniyan, E. Sreevalsan, and S. Rajapandian, “A review of wind energy technologies,” *Renewable and Sustainable Energy Reviews*, vol. 11, pp. 1117–1145, 8 2007.
- [6] J. K. Kaldellis and D. Zafirakis, “The wind energy (r)evolution: A short review of a long history,” *Renewable Energy*, vol. 36, pp. 1887–1901, 7 2011.
- [7] N. Kannan and D. Vakeesan, “Solar energy for future world: - A review,” *Renewable and Sustainable Energy Reviews*, vol. 62, pp. 1092–1105, 9 2016.
- [8] N. L. Panwar, S. C. Kaushik, and S. Kothari, “Role of renewable energy sources in environmental protection: A review,” *Renewable and Sustainable Energy Reviews*, vol. 15, pp. 1513–1524, 4 2011.
- [9] “Annual Energy Outlook 2022 - U.S. Energy Information Administration (EIA).”
- [10] “Real-time Operating Grid - U.S. Energy Information Administration (EIA).”
- [11] “PPA Insights: Solar radiation and wind speed data - KYOS.”

- [12] S. Ould Amrouche, D. Rekioua, T. Rekioua, and S. Bacha, “Overview of energy storage in renewable energy systems,” *International Journal of Hydrogen Energy*, vol. 41, pp. 20914–20927, 12 2016.
- [13] A. Z. AL Shaqsi, K. Sopian, and A. Al-Hinai, “Review of energy storage services, applications, limitations, and benefits,” *Energy Reports*, vol. 6, pp. 288–306, 12 2020.
- [14] T. Chen, Y. Jin, H. Lv, A. Yang, M. Liu, B. Chen, Y. Xie, and Q. Chen, “Applications of Lithium-Ion Batteries in Grid-Scale Energy Storage Systems,” *Transactions of Tianjin University*, vol. 26, pp. 208–217, 2020.
- [15] J. O. G. Posada, A. J. Rennie, S. P. Villar, V. L. Martins, J. Marinaccio, A. Barnes, C. F. Glover, D. A. Worsley, and P. J. Hall, “Aqueous batteries as grid scale energy storage solutions,” *Renewable and Sustainable Energy Reviews*, vol. 68, pp. 1174–1182, 2 2017.
- [16] L. Hu and K. Xu, “Nonflammable electrolyte enhances battery safety,” *Proceedings of the National Academy of Sciences of the United States of America*, vol. 111, pp. 3205–3206, 3 2014.
- [17] J. Sun, J. Li, T. Zhou, K. Yang, S. Wei, N. Tang, N. Dang, H. Li, X. Qiu, and L. Chen, “Toxicity, a serious concern of thermal runaway from commercial Li-ion battery,” *Nano Energy*, vol. 27, pp. 313–319, 9 2016.
- [18] A. Lecocq, G. G. Eshetu, S. Grugeon, N. Martin, S. Laruelle, and G. Marlair, “Scenario-based prediction of Li-ion batteries fire-induced toxicity,” *Journal of Power Sources*, vol. 316, pp. 197–206, 6 2016.
- [19] C. Dong, F. Xu, L. Chen, Z. Chen, and Y. Cao, “Design Strategies for High-Voltage Aqueous Batteries,” 2021.
- [20] V. Singh, S. Kim, J. Kang, and H. R. Byon, “Aqueous organic redox flow batteries,” 2019.
- [21] L. Suo, O. Borodin, T. Gao, M. Olguin, J. Ho, X. Fan, C. Luo, C. Wang, and K. Xu, ““Water-in-salt” electrolyte enables high-voltage aqueous lithium-ion chemistries,” *Science*, vol. 350, pp. 938–943, 11 2015.
- [22] L. Suo, O. Leg Borodin, W. Un, X. Fan, C. Yang, E. Wang, Z. Ma, M. Schroeder, A. Von Cresce, S. M. Russell, M. Armand, A. Angell, K. Xu, and C. Wang, “Ad-

- vanced High-Voltage Aqueous Lithium-Ion Battery Enabled by "Water-in-Bisalt" Electrolyte," 2016.
- [23] J. Zhang, C. Cui, P.-F. Wang, Q. Li, L. Chen, F. Han, T. Jin, S. Liu, H. Choudhary, S. R. Raghavan, N. Eidson, A. Von Cresce, L. Ma, J. Uddin, D. Addison, C. Yang, and C. Wang, "Water-in-salt" polymer electrolyte for Li-ion batteries \dagger ," 2878 — *Energy Environ. Sci*, vol. 13, p. 2878, 2020.
 - [24] Y. Yamada, K. Usui, K. Sodeyama, S. Ko, Y. Tateyama, and A. Yamada, "Hydrate-melt electrolytes for high-energy-density aqueous batteries," 2016.
 - [25] M. L. Perry and A. Z. Weber, "Advanced Redox-Flow Batteries: A Perspective," *Journal of The Electrochemical Society*, vol. 163, no. 1, pp. A5064–A5067, 2016.
 - [26] R. M. Darling, K. G. Gallagher, J. A. Kowalski, S. Ha, and F. R. Brushett, "Pathways to low-cost electrochemical energy storage: a comparison of aqueous and nonaqueous flow batteries," *Energy & Environmental Science*, vol. 7, pp. 3459–3477, 10 2014.
 - [27] Y. K. Zeng, X. L. Zhou, L. An, L. Wei, and T. S. Zhao, "A high-performance flow-field structured iron-chromium redox flow battery," *Journal of Power Sources*, vol. 324, pp. 738–744, 8 2016.
 - [28] E. Sum and M. Skyllas-Kazacos, "A study of the V(II)/V(III) redox couple for redox flow cell applications," *Journal of Power Sources*, vol. 15, pp. 179–190, 6 1985.
 - [29] M. Skyllas-Kazacos, M. Rychick, and R. Robins, "All-vanadium redox battery," 1 1988.
 - [30] A. Parasuraman, T. M. Lim, C. Menictas, and M. Skyllas-Kazacos, "Review of material research and development for vanadium redox flow battery applications," *Electrochimica Acta*, vol. 101, pp. 27–40, 7 2013.
 - [31] M. Skyllas-Kazacos, L. Cao, M. Kazacos, N. Kausar, and A. Mousa, "Vanadium Electrolyte Studies for the Vanadium Redox Battery—A Review," *ChemSusChem*, vol. 9, pp. 1521–1543, 7 2016.
 - [32] M. Skyllas-Kazacos, M. H. Chakrabarti, S. A. Hajimolana, F. S. Mjalli, and M. Saleem, "Progress in Flow Battery Research and Development," *Journal of The Electrochemical Society*, vol. 158, p. R55, 6 2011.

- [33] L. Li, S. Kim, W. Wang, M. Vijayakumar, Z. Nie, B. Chen, J. Zhang, G. Xia, J. Hu, G. Graff, J. Liu, and Z. Yang, “A Stable Vanadium Redox-Flow Battery with High Energy Density for Large-Scale Energy Storage,” *Advanced Energy Materials*, vol. 1, pp. 394–400, 5 2011.
- [34] N. Xu, X. Li, X. Zhao, J. B. Goodenough, and K. Huang, “A novel solid oxide redox flow battery for grid energy storage,” *Energy & Environmental Science*, vol. 4, pp. 4942–4946, 11 2011.
- [35] Y. K. Zeng, T. S. Zhao, L. An, X. L. Zhou, and L. Wei, “A comparative study of all-vanadium and iron-chromium redox flow batteries for large-scale energy storage,” *Journal of Power Sources*, vol. 300, pp. 438–443, 12 2015.
- [36] W. Wang, Q. Luo, B. Li, X. Wei, L. Li, and Z. Yang, “Recent Progress in Redox Flow Battery Research and Development,” *Advanced Functional Materials*, vol. 23, pp. 970–986, 2 2013.
- [37] L. Trahey, F. R. Brushett, N. P. Balsara, G. Ceder, L. Cheng, Y. M. Chiang, N. T. Hahn, B. J. Ingram, S. D. Minter, J. S. Moore, K. T. Mueller, L. F. Nazar, K. A. Persson, D. J. Siegel, K. Xu, K. R. Zavadil, V. Srinivasan, and G. W. Crabtree, “Energy storage emerging: A perspective from the Joint Center for Energy Storage Research,” *Proceedings of the National Academy of Sciences of the United States of America*, vol. 117, pp. 12550–12557, 6 2020.
- [38] C. Prochaska and M. Gonzales Harsha, “Energy Storage Grand Challenge: Energy Storage Market Report,” tech. rep., United States Department of Energy, 12 2020.
- [39] A. Anisie and F. Boshell, “Utility-Scale Batteries Innovation Landscape Brief,” tech. rep., International Renewable Energy Agency, Abu Dhabi, 2019.
- [40] M. Li, Z. Rhodes, J. R. Cabrera-Pardo, and S. D. Minter, “Recent advancements in rational design of non-aqueous organic redox flow batteries,” *Sustainable Energy & Fuels*, vol. 4, pp. 4370–4389, 8 2020.
- [41] P. Alotto, M. Guarnieri, and F. Moro, “Redox flow batteries for the storage of renewable energy: A review,” *Renewable and Sustainable Energy Reviews*, vol. 29, pp. 325–335, 1 2014.
- [42] L. H. Thaller and NASA Lewis Research Center, “Electrically Rechargeable Redox Flow Cells,” *Intersoc. Energy Conversion Eng. Conf.*, 10 1974.

- [43] A. Ciotola, M. Fuss, S. Colombo, and W. R. Poganietz, “The potential supply risk of vanadium for the renewable energy transition in Germany,” *Journal of Energy Storage*, vol. 33, p. 102094, 1 2021.
- [44] L. Su, A. F. Badel, C. Cao, J. J. Hinricher, and F. R. Brushett, “Toward an Inexpensive Aqueous Polysulfide-Polyiodide Redox Flow Battery,” *Industrial and Engineering Chemistry Research*, vol. 56, pp. 9783–9792, 9 2017.
- [45] F. R. Brushett, M. J. Aziz, and K. E. Rodby, “On Lifetime and Cost of Redox-Active Organics for Aqueous Flow Batteries,” *ACS Energy Letters*, vol. 5, pp. 879–884, 3 2020.
- [46] K. Lin, R. Gómez-Bombarelli, E. S. Beh, L. Tong, Q. Chen, A. Valle, A. Aspuru-Guzik, M. J. Aziz, and R. G. Gordon, “A redox-flow battery with an alloxazine-based organic electrolyte,” *Nature Energy* 2016 1:9, vol. 1, pp. 1–8, 7 2016.
- [47] D. G. Kwabi, K. Lin, Y. Ji, E. F. Kerr, M. A. Goulet, D. De Porcellinis, D. P. Tabor, D. A. Pollack, A. Aspuru-Guzik, R. G. Gordon, and M. J. Aziz, “Alkaline Quinone Flow Battery with Long Lifetime at pH 12,” *Joule*, vol. 2, pp. 1894–1906, 9 2018.
- [48] K. Lin, Q. Chen, M. R. Gerhardt, L. Tong, S. B. Kim, L. Eisenach, A. W. Valle, D. Hardee, R. G. Gordon, M. J. Aziz, and M. P. Marshak, “Alkaline quinone flow battery,” *Science*, vol. 349, pp. 1529–1532, 9 2015.
- [49] J. Huang, L. Su, J. A. Kowalski, J. L. Barton, M. Ferrandon, A. K. Burrell, F. R. Brushett, and L. Zhang, “A subtractive approach to molecular engineering of dimethoxybenzene-based redox materials for non-aqueous flow batteries,” *Journal of Materials Chemistry A*, vol. 3, pp. 14971–14976, 7 2015.
- [50] Q. Liu, A. A. Shinkle, Y. Li, C. W. Monroe, L. T. Thompson, and A. E. Sleightholme, “Non-aqueous chromium acetylacetonate electrolyte for redox flow batteries,” *Electrochemistry Communications*, vol. 12, pp. 1634–1637, 11 2010.
- [51] A. E. Sleightholme, A. A. Shinkle, Q. Liu, Y. Li, C. W. Monroe, and L. T. Thompson, “Non-aqueous manganese acetylacetonate electrolyte for redox flow batteries,” *Journal of Power Sources*, vol. 196, pp. 5742–5745, 7 2011.
- [52] E. V. Carino, J. Staszak-Jirkovsky, R. S. Assary, L. A. Curtiss, N. M. Markovic, and F. R. Brushett, “Tuning the Stability of Organic Active Materials for Nonaqueous

- Redox Flow Batteries via Reversible, Electrochemically Mediated Li⁺ Coordination,” *Chemistry of Materials*, vol. 28, pp. 2529–2539, 5 2016.
- [53] R. W. Hogue and K. E. Toghill, “Metal coordination complexes in nonaqueous redox flow batteries This review comes from a themed issue on Energy Storage,” *Current Opinion in Electrochemistry*, vol. 18, pp. 37–45, 2019.
 - [54] G. Kwon, S. Lee, J. Hwang, H. S. Shim, B. Lee, M. H. Lee, Y. Ko, S. K. Jung, K. Ku, J. Hong, and K. Kang, “Multi-redox Molecule for High-Energy Redox Flow Batteries,” *Joule*, vol. 2, pp. 1771–1782, 9 2018.
 - [55] P. Navalpotro, J. Palma, M. Anderson, and R. Marcilla, “A Membrane-Free Redox Flow Battery with Two Immiscible Redox Electrolytes,” *Angewandte Chemie - International Edition*, vol. 56, pp. 12460–12465, 10 2017.
 - [56] M. Pahlevaninezhad, P. Leung, P. Q. Velasco, M. Pahlevani, F. C. Walsh, E. P. Roberts, and C. Ponce de León, “A nonaqueous organic redox flow battery using multi-electron quinone molecules,” *Journal of Power Sources*, vol. 500, p. 229942, 7 2021.
 - [57] N. H. Attanayake, J. A. Kowalski, K. V. Greco, M. D. Casselman, J. D. Milshtein, S. J. Chapman, S. R. Parkin, F. R. Brushett, and S. A. Odom, “Tailoring Two-Electron-Donating Phenothiazines to Enable High-Concentration Redox Electrolytes for Use in Nonaqueous Redox Flow Batteries,” *Chemistry of Materials*, vol. 31, pp. 4353–4363, 6 2019.
 - [58] S. M. Laramie, J. D. Milshtein, T. M. Breault, F. R. Brushett, and L. T. Thompson, “Performance and cost characteristics of multi-electron transfer, common ion exchange non-aqueous redox flow batteries,” *Journal of Power Sources*, vol. 327, pp. 681–692, 9 2016.
 - [59] A. Ohira, T. Funaki, E. Ishida, J. D. Kim, and Y. Sato, “Redox-Flow Battery Operating in Neutral and Acidic Environments with Multielectron-Transfer-Type Viologen Molecular Assembly,” *ACS Applied Energy Materials*, vol. 3, pp. 4377–4383, 5 2020.
 - [60] Q. Xu, L. Y. Qin, Y. N. Ji, P. K. Leung, H. N. Su, F. Qiao, W. W. Yang, A. A. Shah, and H. M. Li, “A deep eutectic solvent (DES) electrolyte-based vanadium-iron redox flow battery enabling higher specific capacity and improved thermal stability,” *Electrochimica Acta*, vol. 293, pp. 426–431, 1 2019.

- [61] N. S. Sinclair, D. Poe, R. F. Savinell, E. J. Maginn, and J. S. Wainright, “A Nitroxide Containing Organic Molecule in a Deep Eutectic Solvent for Flow Battery Applications,” *Journal of The Electrochemical Society*, vol. 168, p. 020527, 2 2021.
- [62] R. Cheng, J. Xu, J. Zhang, P. Leung, Q. Ma, H. Su, W. Yang, and Q. Xu, “Facile segmented graphite felt electrode for iron-vanadium redox flow batteries with deep eutectic solvent (DES) electrolyte,” *Journal of Power Sources*, vol. 483, p. 229200, 1 2021.
- [63] H. Zhang and C. Sun, “Cost-effective iron-based aqueous redox flow battery for large-scale energy storage application: A review,” *Journal of Power Sources*, vol. 493, p. 229445, 2021.
- [64] Y. A. Gandomi, D. S. Aaron, J. R. Houser, M. C. Daugherty, J. T. Clement, A. M. Pezeshki, T. Y. Ertugrul, D. P. Moseley, and M. M. Mench, “Critical Review—Experimental Diagnostics and Material Characterization Techniques Used on Redox Flow Batteries,” *Journal of The Electrochemical Society*, vol. 165, pp. A970–A1010, 4 2018.
- [65] D. G. Kwabi, Y. Ji, and M. J. Aziz, “Electrolyte Lifetime in Aqueous Organic Redox Flow Batteries: A Critical Review,” *Chemical Reviews*, vol. 120, pp. 6467–6489, 7 2020.
- [66] A. J. Bard and L. R. Faulkner, *Electrochemical Methods: Fundamentals and Applications*. Danvers: John Wiley & Sons, Inc., 2 ed., 2001.
- [67] R. S. Nicholson, “Theory and Application of Cyclic Voltammetry for Measurement of Electrode Reaction Kinetics,” *Analytical Chemistry*, vol. 37, pp. 1351–1355, 10 1965.
- [68] T.-M. Tseng, R.-H. Huang, C.-Y. Huang, K.-L. Hsueh, and F.-S. Shieu, “A Kinetic Study of the Platinum/Carbon Anode Catalyst for Vanadium Redox Flow Battery,” *Journal of The Electrochemical Society*, vol. 160, pp. A690–A696, 2 2013.
- [69] E. Martínez-González, H. G. Laguna, M. Sánchez-Castellanos, S. S. Rozenel, V. M. Ugalde-Saldivar, and C. Amador-Bedolla, “Kinetic Properties of Aqueous Organic Redox Flow Battery Anolytes Using the Marcus-Hush Theory,” *ACS Applied Energy Materials*, vol. 3, pp. 8833–8841, 9 2020.

- [70] A. Orita, M. G. Verde, M. Sakai, and Y. S. Meng, “A biomimetic redox flow battery based on flavin mononucleotide,” *Nature Communications* 2016 7:1, vol. 7, pp. 1–8, 10 2016.
- [71] H. Wang, S. Y. Sayed, E. J. Lubner, B. C. Olsen, S. M. Shirurkar, S. Venkatakrishnan, U. M. Tefashe, A. K. Farquhar, E. S. Smotkin, R. L. McCreery, and J. M. Buriak, “Redox Flow Batteries: How to Determine Electrochemical Kinetic Parameters,” *ACS Nano*, vol. 14, pp. 2575–2584, 3 2020.
- [72] R. S. Nicholson, “Theory and Application of Cyclic Voltammetry for Measurement of Electrode Reaction Kinetics,” *Analytical Chemistry*, 1965.
- [73] J. Masa, C. Batchelor-McAuley, W. Schuhmann, and R. G. Compton, “Koutecky-Levich analysis applied to nanoparticle modified rotating disk electrodes: Electrocatalysis or misinterpretation,” *Nano Research*, vol. 7, no. 1, pp. 71–78, 2014.
- [74] U. A. Paulus, T. J. Schmidt, H. A. Gasteiger, and R. J. Behm, “Oxygen reduction on a high-surface area Pt/Vulcan carbon catalyst: a thin-film rotating ring-disk electrode study,” *Journal of Electroanalytical Chemistry*, vol. 495, pp. 134–145, 1 2001.
- [75] T. J. Schmidt, H. A. Gasteiger, G. D. Stäb, P. M. Urban, D. M. Kolb, and R. J. Behm, “Characterization of High-Surface-Area Electrocatalysts Using a Rotating Disk Electrode Configuration,” *Journal of The Electrochemical Society*, vol. 145, pp. 2354–2358, 7 1998.
- [76] S. N. Pronkin, A. Bonnefont, P. S. Ruvinskiy, and E. R. Savinova, “Hydrogen oxidation kinetics on model Pd/C electrodes: Electrochemical impedance spectroscopy and rotating disk electrode study,” *Electrochimica Acta*, vol. 55, pp. 3312–3323, 3 2010.
- [77] E. Siebert, A. Hammouche, and M. Kleitz, “Impedance spectroscopy analysis of La_{1-x}Sr_xMnO₃-yttria-stabilized zirconia electrode kinetics,” *Electrochimica Acta*, vol. 40, no. 11, pp. 1741–1753, 1995.
- [78] M. J. Escudero, A. Aguadero, J. A. Alonso, and L. Daza, “A kinetic study of oxygen reduction reaction on La₂NiO₄ cathodes by means of impedance spectroscopy,” *Journal of Electroanalytical Chemistry*, vol. 611, pp. 107–116, 12 2007.
- [79] X. Wu, H. Xu, L. Lu, H. Zhao, J. Fu, Y. Shen, P. Xu, and Y. Dong, “PbO₂-modified graphite felt as the positive electrode for an all-vanadium redox flow battery,” *Journal of Power Sources*, vol. 250, pp. 274–278, 3 2014.

- [80] A. Di Blasi, O. Di Blasi, N. Briguglio, A. S. Aricò, D. Sebastián, M. J. Lázaro, G. Monforte, and V. Antonucci, “Investigation of several graphite-based electrodes for vanadium redox flow cell,” *Journal of Power Sources*, vol. 227, pp. 15–23, 4 2013.
- [81] C.-N. Sun, F. M. Delnick, D. S. Aaron, A. B. Papandrew, M. M. Mench, and T. A. Zawodzinski, “Resolving Losses at the Negative Electrode in All-Vanadium Redox Flow Batteries Using Electrochemical Impedance Spectroscopy,” *Journal of The Electrochemical Society*, vol. 161, pp. A981–A988, 4 2014.
- [82] F. Q. Xue, Y. L. Wang, W. H. Wang, and X. D. Wang, “Investigation on the electrode process of the Mn(II)/Mn(III) couple in redox flow battery,” *Electrochimica Acta*, vol. 53, pp. 6636–6642, 9 2008.
- [83] A. Abbas, S. Abbas, A. Bhattarai, N. M. Latiff, N. Wai, A. N. Phan, and T. M. Lim, “Effect of electrode porosity on the charge transfer in vanadium redox flow battery,” *Journal of Power Sources*, vol. 488, p. 229411, 3 2021.
- [84] W. H. Wang and X. D. Wang, “Investigation of Ir-modified carbon felt as the positive electrode of an all-vanadium redox flow battery,” *Electrochimica Acta*, vol. 52, pp. 6755–6762, 8 2007.
- [85] Y. Xiang and W. A. Daoud, “Investigation of an advanced catalytic effect of cobalt oxide modification on graphite felt as the positive electrode of the vanadium redox flow battery,” *Journal of Power Sources*, vol. 416, pp. 175–183, 3 2019.
- [86] A. A. Shinkle, A. E. Sleightholme, L. T. Thompson, and C. W. Monroe, “Electrode kinetics in non-aqueous vanadium acetylacetonate redox flow batteries,” *Journal of Applied Electrochemistry*, vol. 41, pp. 1191–1199, 10 2011.
- [87] M. A. Miller, J. S. Wainright, and R. F. Savinell, “Communication—Iron Ionic Liquid Electrolytes for Redox Flow Battery Applications,” *Journal of The Electrochemical Society*, vol. 163, pp. A578–A579, 1 2016.
- [88] J. A. Kowalski, A. M. Fenton, B. J. Neyhouse, and F. R. Brushett, “A Method for Evaluating Soluble Redox Couple Stability Using Microelectrode Voltammetry,” *Journal of The Electrochemical Society*, vol. 167, p. 160513, 11 2020.
- [89] C. G. Zoski, *Handbook of electrochemistry*. Elsevier, 2007.

- [90] B. Yang, A. Murali, A. Nirmalchandar, B. Jayathilake, G. K. S. Prakash, and S. R. Narayanan, "A Durable, Inexpensive and Scalable Redox Flow Battery Based on Iron Sulfate and Anthraquinone Disulfonic Acid," *Journal of The Electrochemical Society*, vol. 167, p. 060520, 4 2020.
- [91] C. A. McDermott, K. R. Kneten, and R. L. McCreery, "Electron Transfer Kinetics of Aquated $\text{Fe}^{3+}/\text{Fe}^{2+}$, $\text{Eu}^{3+}/\text{Eu}^{2+}$, and $\text{V}^{3+}/\text{V}^{2+}$ at Carbon Electrodes: Inner Sphere Catalysis by Surface Oxides," *Journal of The Electrochemical Society*, vol. 140, p. 2593, 9 1993.
- [92] M. Štulíková and F. Vydra, "Voltammetry with disk electrodes and its analytical application: IV. The voltammetry of iron(III) at the glassy carbon rotating disk electrode in acid media," *Journal of Electroanalytical Chemistry and Interfacial Electrochemistry*, vol. 38, pp. 349–357, 8 1972.
- [93] B. G. Ateya and L. G. Austin, "The Kinetics of $\text{Fe}^{2+}/\text{FeCl}_2/\text{HCl}(\text{aq})$ on Pyrolytic Graphite Electrodes," *Journal of The Electrochemical Society*, vol. 120, p. 1216, 9 1973.
- [94] E. Hollax and D. S. Cheng, "The influence of oxidative pretreatment of graphite electrodes on the catalysis of the $\text{Cr}^{3+}/\text{Cr}^{2+}$ and $\text{Fe}^{3+}/\text{Fe}^{2+}$ redox reactions," *Carbon*, vol. 23, pp. 655–664, 1 1985.
- [95] G. Oriji, Y. Katayama, and T. Miura, "Investigations on $\text{V}(\text{IV})/\text{V}(\text{V})$ and $\text{V}(\text{II})/\text{V}(\text{III})$ redox reactions by various electrochemical methods," *Journal of Power Sources*, vol. 139, pp. 321–324, 1 2005.
- [96] A. Bourke, M. A. Miller, R. P. Lynch, X. Gao, J. Landon, J. S. Wainright, R. F. Savinell, and D. N. Buckley, "Electrode Kinetics of Vanadium Flow Batteries: Contrasting Responses of $\text{V}^{2+}/\text{V}^{3+}$ and $\text{V}^{4+}/\text{V}^{5+}$ to Electrochemical Pretreatment of Carbon," *Journal of The Electrochemical Society*, vol. 163, pp. A5097–A5105, 10 2016.
- [97] H. Liu, L. Yang, Q. Xu, and C. Yan, "An electrochemically activated graphite electrode with excellent kinetics for electrode processes of $\text{V}(\text{II})/\text{V}(\text{III})$ and $\text{V}(\text{IV})/\text{V}(\text{V})$ couples in a vanadium redox flow battery," *RSC Advances*, vol. 4, pp. 55666–55670, 10 2014.
- [98] Y. Li, J. Parrondo, S. Sankarasubramanian, and V. Ramani, "Impact of Surface Carbonyl- and Hydroxyl-Group Concentrations on Electrode Kinetics in an All-

- Vanadium Redox Flow Battery,” *Journal of Physical Chemistry C*, vol. 123, pp. 6370–6378, 3 2019.
- [99] E. Agar, C. R. Dennison, K. W. Knehr, and E. C. Kumbur, “Identification of performance limiting electrode using asymmetric cell configuration in vanadium redox flow batteries,” *Journal of Power Sources*, vol. 225, pp. 89–94, 3 2013.
- [100] X. W. Wu, T. Yamamura, S. Ohta, Q. X. Zhang, F. C. Lv, C. M. Liu, K. Shirasaki, I. Satoh, T. Shikama, D. Lu, and S. Q. Liu, “Acceleration of the redox kinetics of $\text{VO}^{2+}/\text{VO}^{3+}$ and $\text{V}^{3+}/\text{V}^{2+}$ couples on carbon paper,” *Journal of Applied Electrochemistry*, vol. 41, pp. 1183–1190, 10 2011.
- [101] J. Friedl and U. Stimming, “Determining Electron Transfer Kinetics at Porous Electrodes,” *Electrochimica Acta*, vol. 227, pp. 235–245, 2 2017.
- [102] T. Yamamura, N. Watanabe, T. Yano, and Y. Shiokawa, “Electron-Transfer Kinetics of $\text{Np}^{3+}/\text{Np}^{4+}$, $\text{NpO}_2^{2+}/\text{NpO}_2^{3+}$, $\text{V}^{2+}/\text{V}^{3+}$, and $\text{VO}^{2+}/\text{VO}^{3+}$ at Carbon Electrodes,” *Journal of The Electrochemical Society*, vol. 152, p. A830, 3 2005.
- [103] B. Huskinson, M. P. Marshak, C. Suh, S. Er, M. R. Gerhardt, C. J. Galvin, X. Chen, A. Aspuru-Guzik, R. G. Gordon, and M. J. Aziz, “A metal-free organic–inorganic aqueous flow battery,” *Nature* 2014 505:7482, vol. 505, pp. 195–198, 1 2014.
- [104] A. W. Lantz, S. A. Shavaliyev, W. Schroeder, and P. G. Rasmussen, “Evaluation of an Aqueous Biphenol- And Anthraquinone-Based Electrolyte Redox Flow Battery,” *ACS Applied Energy Materials*, vol. 2, pp. 7893–7902, 10 2019.
- [105] T. V. Sawant and J. R. McKone, “Flow Battery Electroanalysis: Hydrodynamic Voltammetry of Aqueous Fe(III/II) Redox Couples at Polycrystalline Pt and Au,” *ACS Applied Energy Materials*, vol. 1, pp. 4743–4753, 9 2018.
- [106] T. V. Sawant and J. R. McKone, “Flow Battery Electroanalysis. 2. Influence of Surface Pretreatment on Fe(III/II) Redox Chemistry at Carbon Electrodes,” *Journal of Physical Chemistry C*, vol. 123, pp. 144–152, 10 2019.
- [107] M.-A. Goulet and M. J. Aziz, “Flow Battery Molecular Reactant Stability Determined by Symmetric Cell Cycling Methods,” *Journal of the Electrochemical Society*.

- [108] Z. Li, L. Liu, Y. Zhao, J. Xi, Z. Wu, and X. Qiu, “The indefinite cycle life via a method of mixing and online electrolysis for vanadium redox flow batteries,” *Journal of Power Sources*, vol. 438, p. 226990, 10 2019.
- [109] S. Rudolph, U. Schröder, and I. M. Bayanov, “On-line controlled state of charge rebalancing in vanadium redox flow battery,” *Journal of Electroanalytical Chemistry*, vol. 703, pp. 29–37, 8 2013.
- [110] A. J. Bard and L. R. Faulkner, *Electrochemical Methods: Fundamentals and Applications, 2nd Edition - Allen J. Bard, Larry R. Faulkner - Google Books*. New York: John Wiley & Sons, Inc., 2 ed., 2001.
- [111] K. W. Knehr, S. Biswas, and D. A. Steingart, “Quantification of the Voltage Losses in the Minimal Architecture Zinc-Bromine Battery Using GITT and EIS,” *Journal of The Electrochemical Society*, vol. 164, pp. A3101–A3108, 10 2017.
- [112] Q. Huang, J. Yang, C. B. Ng, C. Jia, and Q. Wang, “A redox flow lithium battery based on the redox targeting reactions between LiFePO₄ and iodide,” *Energy & Environmental Science*, vol. 9, pp. 917–921, 3 2016.
- [113] T. V. Sawant and J. R. McKone, “Flow Battery Electroanalysis: Hydrodynamic Voltammetry of Aqueous Fe(III/II) Redox Couples at Polycrystalline Pt and Au,” vol. 16, p. 46, 2018.
- [114] J. D. Hofmann and D. Schröder, “Which Parameter is Governing for Aqueous Redox Flow Batteries with Organic Active Material?,” *Chemie Ingenieur Technik*, vol. 91, pp. 786–794, 6 2019.
- [115] J. R. Scully, “Polarization Resistance Method for Determination of Instantaneous Corrosion Rates,” *CORROSION*, vol. 56, no. 2, 1998.
- [116] T. V. Sawant, C. S. Yim, T. J. Henry, D. M. Miller, and J. R. McKone, “Harnessing Interfacial Electron Transfer in Redox Flow Batteries,” *Joule*, vol. 5, pp. 360–378, 2 2021.
- [117] B. Dunn, H. Kamath, and J. M. Tarascon, “Electrical energy storage for the grid: A battery of choices,” *Science*, vol. 334, pp. 928–935, 11 2011.

- [118] G. Kear, A. A. Shah, F. C. Walsh, and A. A. Shah, “Development of the all-vanadium redox flow battery for energy storage: a review of technological, financial and policy aspects,” 2011.
- [119] J. Noack, L. Wietschel, N. Roznyatovskaya, K. Pinkwart, and J. Tübke, “Techno-Economic Modeling and Analysis of Redox Flow Battery Systems,” *Energies* 2016, Vol. 9, Page 627, vol. 9, p. 627, 8 2016.
- [120] C. Minke and T. Turek, “Materials, system designs and modelling approaches in techno-economic assessment of all-vanadium redox flow batteries – A review,” *Journal of Power Sources*, vol. 376, pp. 66–81, 2 2018.
- [121] M. Kim, D. Yun, and J. Jeon, “Effect of a bromine complex agent on electrochemical performances of zinc electrodeposition and electrodisolution in Zinc–Bromide flow battery,” *Journal of Power Sources*, vol. 438, p. 227020, 10 2019.
- [122] Kyu Taek Cho, Paul Ridgway, Adam Z. Weber, Sophia Haussener, Vincent Battaglia, and Venkat Srinivasan, “High Performance Hydrogen/Bromine Redox Flow Battery for Grid-Scale Energy Storage,” 2012.
- [123] W. A. Braff, M. Z. Bazant, and C. R. Buie, “Membrane-less hydrogen bromine flow battery,” *Nature Communications* 2013 4:1, vol. 4, pp. 1–6, 8 2013.
- [124] W. Lee, A. Permatasari, and Y. Kwon, “Neutral pH aqueous redox flow batteries using an anthraquinone-ferrocyanide redox couple,” *J. Mater. Chem. C*, vol. 8, p. 5727, 2020.
- [125] B. Hu, J. Luo, M. Hu, B. Yuan, and T. L. Liu, “A pH-Neutral, Metal-Free Aqueous Organic Redox Flow Battery Employing an Ammonium Anthraquinone Anolyte,” *Angewandte Chemie*, vol. 131, pp. 16782–16789, 11 2019.
- [126] N. H. Hagedorn, “NASA Redox Storage System Development Project Final Report Work performed for NASA Redox Storage System Development Project Final Report,” 1984.
- [127] M. Park, J. Ryu, W. Wang, and J. Cho, “Material design and engineering of next-generation flow-battery technologies,” p. 16080, 2016.
- [128] J. Wang, Z. He, X. Tan, T. Wang, L. Liu, X. He, X. D. Liu, L. Zhang, and K. Du, “High-performance 2.6 V aqueous symmetric supercapacitor based on porous boron-

- doped diamond via regrowth of diamond nanoparticles,” *Carbon*, vol. 160, pp. 71–79, 4 2020.
- [129] R. Trouillon, D. O’hare, and Y. Einaga, “Effect of the doping level on the biological stability of hydrogenated boron doped diamond electrodesw,” *Phys. Chem. Chem. Phys*, vol. 13, pp. 5422–5429, 2011.
 - [130] L. Coustan, G. Shul, and D. Bélanger, “Electrochemical behavior of platinum, gold and glassy carbon electrodes in water-in-salt electrolyte,” *Electrochemistry Communications*, vol. 77, pp. 89–92, 4 2017.
 - [131] T. Lv and L. Suo, “Water-in-salt widens the electrochemical stability window: Thermodynamic and kinetic factors,” *Current Opinion in Electrochemistry*, vol. 29, 10 2021.
 - [132] M. Yu, Y. Lu, H. Zheng, and X. Lu, “New Insights into the Operating Voltage of Aqueous Supercapacitors,” vol. 24, pp. 3639–3649, 2018.
 - [133] F. Reymond, G. Steyaert, P.-A. Carrupt, B. Testa, and H. Girault, “Ionic Partition Diagrams: A Potential-pH Representation,” 1996.
 - [134] T. Verdonck, P. Verpoort, J. De Strycker, A. De Cleene, D. Banerjee, P. Nockemann, R. Van Deun, and K. Van Hecke, “Combining MCR-ALS and EXAFS as tools for speciation of highly chlorinated chromium(III) in mixtures of deep eutectic solvents and water,” *Dalton Transactions*, vol. 48, 2019.
 - [135] S. M. Schmuecker, D. Clouser, T. J. Kraus, and B. M. Leonard, “Synthesis of metastable chromium carbide nanomaterials and their electrocatalytic activity for the hydrogen evolution reaction,” *Dalton Transactions*, vol. 46, p. 13524, 2017.
 - [136] B. Zhang, J. Zhou, Z. Guo, Q. Peng, and Z. Sun, “Two-dimensional chromium boride MBenes with high HER catalytic activity,” *Applied Surface Science*, vol. 500, p. 144248, 1 2020.
 - [137] P. He and L. R. Faulkner, “Intelligent, Automatic Compensation of Solution Resistance,” 1986.
 - [138] F. Wan, J. Zhu, S. Huang, and Z. Niu, “High-Voltage Electrolytes for Aqueous Energy Storage Devices,” *Batteries & Supercaps*, vol. 3, pp. 323–330, 4 2020.

- [139] R. F. Schulte and C. Pisut, “Mineral Industry Surveys PLATINUM-GROUP METALS IN DECEMBER 2020,” 2020.
- [140] K. N. Sheaffer and M. Saedi, “Gold Mineral Industry Surveys,” 2020.
- [141] D. W. Olson, “Graphite 2017,” 2017.
- [142] A. Seidell and W. F. Linke., *Solubilities of Inorganic and Metal Organic Compounds: a Compilation of Quantitative Solubility Data from the Periodical Literature*. 3rd ed., 1940.
- [143] M. N. Berberan-Santos, “Beer’s Law Revisited,” *Journal of Chemical Education*, 1990.
- [144] T. Lopez, E. Sanchez, P. Bosch, Y. Meas, and R. Gomez, “FTIR and UV-Vis (diffuse reflectance) spectroscopic characterization of TiO₂ sol-gel,” *Materials Chemistry and Physics*, vol. 32, pp. 141–152, 8 1992.
- [145] C. Chen, X. Wang, Y. Wang, D. Yang, F. Yao, W. Zhang, B. Wang, G. A. Sewvandi, D. Yang, and D. Hu, “Additive Manufacturing of Piezoelectric Materials,” *Advanced Functional Materials*, vol. 30, 12 2020.
- [146] K. V. Wong and A. Hernandez, “A Review of Additive Manufacturing,” *International Scholarly Research Network ISRN Mechanical Engineering*, vol. 2012, 2012.
- [147] W. E. Frazier, “Metal Additive Manufacturing: A Review,”
- [148] “3D Printing vs CNC Machining: Which is best for prototyping? - 3Dnatives.”
- [149] W. E. Frazier, “Metal Additive Manufacturing: A Review,” 2014.
- [150] P. Parandoush and D. Lin, “A review on additive manufacturing of polymer-fiber composites,” *Composite Structures*, vol. 182, pp. 36–53, 12 2017.
- [151] Q. Yan, H. Dong, J. Su, J. Han, B. Song, Q. Wei, and Y. Shi, “A Review of 3D Printing Technology for Medical Applications,” *Engineering*, vol. 4, pp. 729–742, 10 2018.

- [152] Z. Chen, Z. Li, J. Li, C. Liu, C. Lao, Y. Fu, C. Liu, Y. Li, P. Wang, and Y. He, “3D printing of ceramics: A review,” *Journal of the European Ceramic Society*, vol. 39, pp. 661–687, 4 2019.
- [153] T. D. Ngo, A. Kashani, G. Imbalzano, K. T. Nguyen, and D. Hui, “Additive manufacturing (3D printing): A review of materials, methods, applications and challenges,” *Composites Part B: Engineering*, vol. 143, pp. 172–196, 6 2018.
- [154] S. Ranganathan, T. C. Kuo, and R. L. McCreery, “Facile Preparation of Active Glassy Carbon Electrodes with Activated Carbon and Organic Solvents,” *Analytical Chemistry*, vol. 71, pp. 3574–3580, 8 1999.